

Harmonizing Energy: Unveiling Enhancement Strategies for High-Efficiency Perovskite Solar Cells

A thesis submitted for the degree of

Doctor of Philosophy

By

ROMPIVALASA SANTHOSH

Reg. No: 18CHPH17



School of Chemistry
University of Hyderabad
Hyderabad-500046
Telangana, India

July-2024

Dedicated to My Family & Friends

DECLARATION

I hereby declare that the matter embodied in the thesis entitled "Harmonizing Energy: Unveiling Enhancement Strategies for High-Efficiency Perovskite Solar Cells" is the result of investigation carried out by me in the School of Chemistry, University of Hyderabad, Hyderabad, India, under the supervision of Dr. Murali Banavoth.

In keeping with the general practice of reporting scientific observations, due acknowledgements have been made on the basis of the findings of other investigators. Any omission, which might have occurred by oversight or error, is regretted. This research work is free from Plagiarism. I hereby agree that my thesis can be deposited in Shodhganga/INFLIBNET. A report on plagiarism statistics from the University Librarian is enclosed.

Dr. Murali Banavoth (Supervisor)

School of Chemistry

University of Hyderabad

July, 2024

MURALI BANAVOTH Associate Professor School of Chemistry University of Hyderabad Hyderabad - 500 046 Rompivalasa Santhosh
(18CHPH17)





CERTIFICATE

This is to certify that the thesis entitled "Harmonizing Energy: Unveiling Enhancement Strategies for High-Efficiency Perovskite Solar Cells" submitted by Rompivalasa santhosh holding registration number 18CHPH17 in partial fulfilment of the requirements for award of Doctor of Philosophy in the School of Chemistry is a bonafide work carried out by him under my supervision and guidance.

This thesis is free from plagiarism and has not been submitted previously in part or in full to this or any other University or Institution for award of any degree or diploma.

A. Presented in the following conferences:

- Poster presentation, International Conference 33rd AGM of MRSI and IUMRS-ICA 2022, IIT Jodhpur, India – Dec 19-23, 2022. (Best poster award)
- 2. Poster presentation, CHEMFEST-2022 at SoC, UoH, Hyderabad, India.
- 3. Poster presentation, CHEMFEST-2023 at SoC, UoH, Hyderabad, India.
- 4. Oral presentation, CHEMFEST-2023 at SoC, UoH, Hyderabad, India.

B. Further the student has passed the following courses towards fulfilment of course work requirement for Ph.D.

Course. No	Title	Cradita	C .	
CV 901		Credits	Grade	Result
C1-001	Research Proposal	4	B ⁺	Passed
CY-805	Instrumental Methods A	1		1 asseu
CV enc		4	В	Passed
C1-000	Instrumental Methods B	4	R	Passed
	CY-801	CY-801 Research Proposal CY-805 Instrumental Methods A	CY-801 Research Proposal 4 CY-805 Instrumental Methods A 4	CY-801 Research Proposal 4 B ⁺ CY-805 Instrumental Methods A 4 B

Dr. Murali Banavoth

(Thesis Supervisor)
MURALI BANAVOTH
Associate Professor
School of Chemistry
University of Hyderabad
Hyderabad - 500 046

Dean

School of Chemistry University of Hyderabad

Dean

School of Chemistry University of Hyderabad Hyderabad-500 046.



List of Publications

- 1. Santhosh, R.; Ketavath, R.; Murali, B. Unadorned Molecular Engineering of Phenoxazine-Core-Based Hole-Transport Materials for Sustainable Perovskite Solar Cells. *ACS Applied Energy Materials* 2023, 6 (17), 9001-9011.
- Muniramaiah, R.; Reddy, N. P.; Santhosh, R.; Maharana, G.; Fernandes, J. M.; Padmanaban, D. B.; Kovendhan, M.; Veerappan, G.; Laxminarayana, G.; Banavoth, M.; et al. Anionic Fluorine and Cationic Niobium Codoped Tin Oxide Thin Films as Transparent Conducting Electrodes for Optoelectronic Applications. *physica status solidi* (a) 2023, 220 (14), 2200703.
- 3. Muniramaiah, R.; Reddy, N. P.; Santhosh, R.; Fernandes, J. M.; Padmanaban, D. B.; Maharana, G.; Kovendhan, M.; Veerappan, G.; Laxminarayana, G.; Banavoth, M.; et al. Solvent effect on the optoelectronic properties of fluorine doped SnO2 thin films prepared by spray-pyrolysis. *Surfaces and Interfaces* 2022, 33, 102174.
- Purushotham Reddy, N.; Santhosh, R.; Fernandes, J. M.; Muniramaiah, R.; Murali, B.; Paul Joseph,
 D. Nanocrystalline Sb-doped-BaSnO3 perovskite electron transport layer for dye-sensitized solar cells. *Materials Letters* 2022, 311, 131629.
- Reddy, N. P.; Muniramaiah, R.; Santhosh, R.; Fernandes, J. M.; Padmanaban, D. B.; Maharana, G.; Kovendhan, M.; Paul Joseph, D.; Murali, B. Cost-effective Sb-doped SnO2 films as stable and efficient alternative transparent conducting electrodes for dye-sensitized solar cells. *Journal of Materials Chemistry C* 2022, 10 (20), 7997-8008.
- 6. Reddy, N. P.; Santhosh, R.; Thogiti, S.; Muniramaiah, R.; Joseph, D. P.; Murali, B. Nanostructured ternary perovskite oxides as photoconversion efficiency enhancers for DSSC. *Journal of Materials Chemistry C* 2022, 10 (4), 1403-1413.
- 7. Chander, A.; Chiuyen, P.; Murali, B.; Santosh, R.; Guping, T. Polymer Properties: Functionalization and Surface Modified Nanoparticles. In Role of Novel Drug Delivery Vehicles in Nanobiomedicine, Rajeev, K. T., Neeraj, G., Rahul, S., Prakash Singh, B. Eds.; IntechOpen, 2019; p Ch. 7.
- 8. Purushothamreddy, N.; Santhosh, R.; Ketavath, R.; Murali, B.; Joseph, D. P. Optimization of nanocrystalline Sb doped BaSnO3 for dye-sensitized solar cell applications. *AIP Conference Proceedings* 2020, 2265 (1), 030650.
- 9. Amgoth, C.; Santhosh, R.; Malavath, T.; Singh, A.; Murali, B.; Tang, G. Solvent-Assisted [(Glycine)-(MP-SiO₂NPs)] Aggregate for Drug Loading and Cancer Therapy. *Chemistry Select* 2020, 5 (27), 8221-8232.
- Amgoth, C.; Singh, A.; Santhosh, R.; Yumnam, S.; Mangla, P.; Karthik, R.; Guping, T.; Banavoth, M. Solvent assisted size effect on AuNPs and significant inhibition on K562 cells. *RSC Advances* 2019, 9 (58), 33931-33940.
- 11. Rompivalasa Santhosh, Savu Ramu Naidu, Banavoth Murali, Unlocking Solar Cell Potential: EDTA as a Self-Assembling Chelating Molecule for Enhanced Electron Transport in Perovskite Solar Cells, (Manuscript under Communication).
- 12. Rompivalasa Santhosh, Savu Ramu Naidu, Ranadeep raj S, Banavoth Murali, Leveraging Guanidinium Thiocyanate Self-Assembly to Enhance Perovskite Solar Cell Efficiency (Manuscript under Communication).
- 13. Rompivalasa Santhosh, Savu Ramu Naidu, Ranadeep raj S, Banavoth Murali, Exploring the Effects of Temperature Annealing on Electron Transport Layers to Ease the Perovskite Solar Cell Fabrication (Manuscript under Communication).



Acknowledgements

Since I started my Ph.D. journey with some scepticism, I honestly never imagined I would find myself in this situation. However, my relationships with some extraordinary people and bright minds stretch my capacities and make this journey easy. This has kept me energised over the past six years. It is impossible for me to communicate digitally how much I owe these peoples for what I am today.

First, I would like to thank my supervisor *Dr. Murali Banavoth* for his exceptional guidance, motivation, and support in carrying out this research work. I consider myself blessed to get a chance to pursue my doctoral studies with him. I am grateful to his guidance, encouragement, cooperation, inputs and giving me the freedom to work in the laboratory. I have really enjoyed working with him over the past six years. It is my pleasure to thank the former and present Dean, School of Chemistry (SoC), UoH, for the academic support.

I sincerely thank my doctoral committee members, *Prof. Abani K. Bhuyan* and *Prof. R. Nagarajan*, for their invaluable suggestions and encouragement throughout my research work.

I would like to thank Dr. Pankaj Yadav (Associate professor, PDEU), Dr. Rohith and Dr. Ashish Kulakarni for helping in fabrication of perovskite solar cells. Dr. Suresh Thogiti and Dr. Sandeep Kumar for helping synthesis and fabrication techniques for my PhD progress.

It is a pleasure to acknowledge the financial support from the *Council of Scientific and Industrial Research* (CSIR), New Delhi, that made the work for this dissertation possible. I owe a great debt of gratitude to all my teachers from my school to the university, for their wonderful teaching and education throughout my academics.

In this context, continuous help from the non-teaching stuffs of SoC, specially from Mr. Venkat, Mr. Abraham, Ms. Geetha Ms. Radhika, and Ms. Rani (school office) for various official works, Dr. M. Durga Prasad, Mr. Rajesh for TEM imaging, Mr. Durgesh Kumar Singh and Mr. Mahendar for NMR measurements, Mahesh for XRD, Mr. Sunil and Mr. Vinay for the FESEM and PXRD, helpful to facilitate my research work. Mr. Prasanth helps in nanotechnology for measuring the thickness parameters, and the Centre for Nanotechnology is thankfully acknowledged for extending their Cleanroom facility.

It is simply hard to describe how much I am thankful to the "MB group" members. First, I want to express my gratitude to my seniors Dr. Sachin Gughal, Dr. Praveen Kumar, Dr. Swetha, Dr. Suresh, Dr. Sandeep, Dr. Mohan and Dr. Chander for their continuous help during the tenure



of my Ph.D. journey. I special thanks to the Dr. Ravi, Ranadeep Raj.S, Ramunaidu Savu and Jowhar for their continuous help and support during my Ph.D.

I am really thanks to the Dr. Allu Suryanarayana, Dr. Raveendra, Dr. Hema, Dr. Vinay, Dr. Vinod, Dr. Narshimha, Dr. Ravi, Hemanth, Calvin, Seema, Nirupama, Somratan, Debujana, Somdatta, and so many others in HCU with whom I have some wonderful memories in campus throughout my Ph.D. life.

I would also like to express my sincere thanks to all my close friends R. Kaasi, Sairam, Venkataramana anna, Anand anna, Surendra anna, Gowrinaidu anna, Maheshwer reddy, Devi prasad, Dalinaidu, Durga prasad, Tirupati naidu, Ganapathi, Adithya, Vamsi, Srikar, Ithu Sanyasirao, Azmeera Chandulal, Raju, Ravi, Ajay Sampath and other school friends for their help and encouragement in various stages of my life.

Finally, I would like express my deepest gratitude to my parents my beloved mother Rompivalasa Adilakshmi, and Father Rompivalasa Atchiyya and babai Rompivalasa Simhachalam without their sacrifice and financial support, I would not have reached this stage of my life. I am greatly indebted from the bottom of my heart to my teachers Mahalakshmu Naidu Sir, Srinivasa sir(English), Ramakrishna sir, Ramarao sir, Kishore sir, Murali sir, Sunny sir, Narayanarao sir, Koti sir, Ramanarao sir for their guidance and stay as a philosophers of my life. My Mother deserves special mention for her inseparable support and prayers. Any word would be less to justify their sacrifice and I don't want to let them down with 'thank you' either. I would like to thanks to all my sisters and cousins (Bhavani, kavya, Anu, Santhoshi, Devi, Lavanya, Harikrishna, Venkataramana, Eshwararao, Govinda, Bhavani) for their support and prayers. Here I specially mention my uncle (Rompivalasa simhachalam) because of him, I reached this goal. I thank to my brother-in-law (D. Mangtha Nayak) for his continuous support during my Ph.D.

This thesis embodies the results of the last few years' work whereby I have been accompanied and supported by many people. It is an honor and a very pleasant opportunity to express my gratitude to all of them.



Table of Contents:

Declaration	i
Certificate	ii
Acknowledgements	iv-v
Table of contents	vi
Outline of the contents	vii-xi
List of Figures	xii-xv
List of Tables	xvi
Symbols and Abbreviations	xvii-xx
Synopsis	xxi-xxv
Chapter-1	1-29
Chapter-2	30-60
Chapter-3	61-74
Chapter-4	75-86
Chapter-5	87-99
Chapter-6	101-108
Appendix	110-118
Bibliography	119-131
Presentations & publications	133-136

Outline of the Contents

Introduction and Analysis	1-29
1.1 Comprehensive Statistical Analysis of Global and Indian Energy Trends	2-3
1.2 Brief Statistical Analysis of Global and Indian Photovoltaic Energy Trends	4-6
1.3 Perovskite Solar Energy Statistics	6-7
1.3.1 Global Perovskite Solar Energy Statistics	6
1.3.2 Perovskite Solar Energy in India	6
1.3.3 Comparative Insights and Future Prospects	7
1.4 Evaluation of solar cells	7-10
1.4.1 First Generation Solar Cells: Silicon Wafer-Based Technology	8
1.4.2 Second Generation Solar Cells: Thin-Film Technologies	8
1.4.3 Third Generation Solar Cells: Emerging Technologies	9
1.4.4 Fourth Generation Solar Cells: Hybrid and Advanced Technologies	10
1.5 Evaluating Silicon and Perovskite Solar Cells: Efficiency, Cost, and Application Potential	10-12
1.5.1 Silicon Solar Cells	10
1.5.2 Perovskite Solar Cells	11
1.5.3 Comparative Analysis	11
1.6 Why Perovskite Solar Cells?	12-14
1.7 History and Evolution of Perovskite Solar Cells: Early Discoveries and Initial Developments	14-26
1.7.1 Rapid Efficiency Improvements	14
1.7.2 Addressing Stability and Scalability Challenges	15
1.7.3 Recent Advances and Commercialization Efforts	15
1.7.4 Future Prospects	15
1.8 Solar Radiation and Its Components	16-18

	VIII				
1.8.1 Air Mass (AM) and Standard Spectrum AM1.5G	17				
1.8.2 AM1.5G and Its Importance	17				
1.8.3 Application in Photovoltaic Systems	18				
1.9 Perovskite Solar Cells: Background Theory and Principles	18-29				
1.9.1 Background Theory	18				
1.9.2 Working Principle	19				
1.9.3 Key Properties and Advantages	20				
1.8.1 Air Mass (AM) and Standard Spectrum AM1.5G 1.8.2 AM1.5G and Its Importance 1.8.3 Application in Photovoltaic Systems 1.9 Perovskite Solar Cells: Background Theory and Principles 1.9.1 Background Theory 1.9.2 Working Principle 1.9.3 Key Properties and Advantages 1.9.4 Current Issues to Commercialize Perovskite Solar Cells 1.9.5 Perovskite Solar Cells: Causes of Degradation 1.9.6 Perovskite Solar Cells: Methods of Increasing Stability & Durability Chapter-2: Optimizing Perovskite Solar Cells: Materials, Methods, and Characterization Insights 2.1 Semiconductor Energetic Quantities 2.1.1 Bands and Band Edges 2.1.2 Bandgap 2.1.3 Fermi Level 2.1.4 Vacuum Level 2.1.5 Work Function 2.1.6 Ionization Energy and Electron Affinity 2.1.7 p-n junction 2.1.8 p-i-n Junction 2.1.9 Solar Spectrum and Photovoltaic Effect 2.2 Solar Cell Parameters 2.3 Halide Perovskite Solar Cells					
1.9.5 Perovskite Solar Cells: Causes of Degradation	22				
1.9.6 Perovskite Solar Cells: Methods of Increasing Stability & Durability	24				
1.8.2 AM1.5G and Its Importance 1.8.3 Application in Photovoltaic Systems 1.9 Perovskite Solar Cells: Background Theory and Principles 1.9.1 Background Theory 1.9.2 Working Principle 1.9.3 Key Properties and Advantages 1.9.4 Current Issues to Commercialize Perovskite Solar Cells 1.9.5 Perovskite Solar Cells: Causes of Degradation 1.9.6 Perovskite Solar Cells: Methods of Increasing Stability & Durability Chapter-2: Optimizing Perovskite Solar Cells: Materials, Methods, and Characterization Insights 2.1 Semiconductor Energetic Quantities 2.1.1 Bands and Band Edges 2.1.2 Bandgap 2.1.3 Fermi Level 2.1.4 Vacuum Level 2.1.5 Work Function 2.1.6 Ionization Energy and Electron Affinity 2.1.7 p-n junction 2.1.8 p-i-n Junction 2.1.9 Solar Spectrum and Photovoltaic Effect 2.2 Solar Cell Parameters 2.3 Halide Perovskite Solar Cells					
2.1.1 Bands and Band Edges	31				
2.1.2 Bandgap	31				
2.1.3 Fermi Level	32				
2.1.4 Vacuum Level	32				
2.1.5 Work Function	33				
2.1.6 Ionization Energy and Electron Affinity	33				
2.1.7 p-n junction	33				
2.1.8 p-i-n Junction	35				
2.1.9 Solar Spectrum and Photovoltaic Effect	36				
2.2 Solar Cell Parameters	37-38				
2.3 Halide Perovskite Solar Cells	38-39				
2.3.1Properties of Halide Perovskites	38				

	IX
2.4 Role of Interfaces in perovskite solar cells	40-52
2.4.1 Features of Perovskite and Its Surface	41
2.4.1.1 Defects and Recombination	
2.4.1.2 Ion Migration	
2.4.1.3 Hysteresis	
2.4.2 Interaction of Perovskite with Adjacent Layers	45
2.4.3 Energy Level Alignment and Charge Transport	46
2.4.4 Functionalization as a Strategy	47
2.4.5 Coordinate Bonding: Lewis Acids and Lewis Bases	48
2.4.6 Halogen Bonding	49
2.4.6.1 Directionality	
2.4.6.2 Strength Tunability	
2.4.6.2 Strength Tunability	
2.4.6.3 Hydrophobicity	
2.4.6.4 Donor Atom Dimension	
2.4.7 Self-Assembled Monolayers	51
2.5 Optical Characterisation	53-55
2.5.1 UV-Vis absorbance spectroscopy	53
2.5.2 Fluorescence Spectroscopy	54
2.5.3 Time-Resolved Photoluminescence (TRPL)	55
2.6 Electrochemical Impedance Spectroscopy	56
2.7 Electrical Characterisations: Carrier mobility and conductivity	57
2.8 Field Emission Scanning Electron Microscope (FESEM)	58



2.9 Samples and Device Preparation	59
2.10 Materials, Reagents and Solvents	60
Chapter-3: Unlocking Solar Cell Potential: EDTA as a Self-Assembling Chelating Molecule for Enhanced Electron Transport in Perovskite Sol Cells 61-7	ar
Abstract	62
3.1. Introduction	63-64
3.2. Experimental Section	64-67
3.2.1 Fabrication of Perovskite solar cells	64
3.2.2 Electron mobility of Perovskite layer with and without EDTA films	66
3.3. Results and Discussions	67-72
3.3.1. Characterization of EDTA films and perovskite films	67
3.3.2. Photovoltaic Properties	69
3.3.3 Stability and Carrier parameters	72
3.4. Conclusions	73
Chapter-4: Leveraging Guanidinium Thiocyanate Self-Assembly to Er Perovskite Solar Cell Efficiency 75-8	
Abstract	76
4.1. Introduction	77-78
3.2. Experimental Section	79-81
4.2.1 Perovskite solar cells fabrication	79
4.2.2 Electron mobility of Perovskite layer with and without GuSCN films	80
4.3. Results and Discussions	81-86
4.3.1. Spectral Characterizations	81
4.3.2. Photovoltaic Studies	83
4.3.3 Stability and Carrier parameters	85
4.4. Conclusions	86



Chapter-5:	Exploring	the	Effects	of T	Temperature	Annealing	on	Electron
Transport I	Lavers to Ea	ise th	ne Perov	skite	e Solar Cell F	abrication	8	7-99

Abstract	88
5.1. Introduction	89-90
5.2. Experimental Section	91-93
5.2.1 Perovskite solar cells fabrication	91
5.2.2 Electron mobility of Perovskite layer with ETL layers	93
5.3. Results and Discussions	94-98
5.3.1. Photo physical properties	94
5.3.2. Photoelectric properties	95
4.3.3 Stability and Carrier parameters	98
4.4. Conclusions	99
Chapter-6	101-108
7.1. Summary	102
7.2. Conclusion	105
7.3. Future Scope	106
Appendix	109-118
Chapter-3	110-112
Chapter-4	113-115
Chapter-5	116-118
Bibliography	119-131
Publications & Presentation	133-136



List of Figures

Figure 1.1 . Global primary energy consumption. Adopted from Energy Institute statistic	cal
review of world energy 2024.	2

Figure 1.2. India primary energy consumption. Adopted from Energy statistics India 2024.

3

- **Figure 1.3.** Evolution of the solar energy technology by generations.
- **Figure. 1.4.** Best Research solar cell efficiencies graph for all generations, highlighted emerging PV technology including perovskite single junction solar cells. Adopted from NREL photovoltaics research published in 2024.
- **Figure. 1.5.** Solar energy radiation spectrum for AM0 and AM1.5, including diffusive dust layers. Adopted from PVEducation.
- **Figure. 1.6. (a)** Basic perovskite crystal structure in the form of ABX_{3.} (b) Working principle for Conventional perovskite solar cells. (c) Basic architecture of mesoporous n-i-p based perovskite solar device.
- **Figure 2.1.** (a) Energy diagram for a semiconductor with flat bands at the surface illustrates various key energy levels and parameters, including the CBM/LUMO and VBM/HOMO, also depicts the vacuum level (E_{VAC}), the work function (WF), the energy gap (EG), ionization energy (IE), and electron affinity (EA). Adapted from Kahn A., Mater. Horiz. 3 (2016). (b) 1) The vacuum level near the surface, denoted as $E_{vac}(s)$, the work function (WF), and the vacuum level at an infinite distance, $E_{vac}(\infty)$, are depicted. The transition between these two levels indicates where the dipole field diminishes. 2) The electron distribution density, $\rho(x)$, both within and outside the solid, generates a dipole layer and influences the work function. 3) The electron potential energy step, ΔE , induced by the surface dipole, is also shown. Adapted from Cahen et al., Adv. Mat. 15 (2003)
- **Figure. 2.2.** (a) The diagram illustrates a p-n heterojunction in the dark. From top to bottom, it shows the p-doped and n-doped semiconductors before they come into contact, followed by the materials after contact where electrons and holes diffuse. This diffusion leads to the formation of a depletion region with an associated electric field (E_{field}). Additionally, both diffusion current and drift current are depicted. (b) The accompanying band diagrams correspond to the scenarios on the left. Before contact, the materials are aligned based on the vacuum level



(E_{VAC}). After contact, the Fermi levels (EF) align. The diagram also includes the conduction band minimum (CBM), valence band maximum (VBM), work function (WF), bandgap (EG), electron affinity (EA), and ionization energy (IE).

Figure 2.3. (a) A sketch of the band diagram for a p-i-n junction at equilibrium, illustrating the energy bands across the junction. (b) A similar sketch depicting the band diagram at open circuit voltage. This includes the electron and hole quasi-Fermi levels (E_F^n and E_F^p , respectively), as well as the quasi-Fermi level splitting (QFLS).

Figure 2.4. An example of typical JV curves is shown for both illuminated (light blue) and dark (dark blue) conditions. Key photovoltaic parameters are highlighted, including the maximum power point (MPP) along with its corresponding current (J_{MPP}) and voltage (V_{MPP}), the open circuit voltage (V_{OC}), and the short circuit current (J_{SC}).

Figure. 2.5. (a) Illustration depicting the primary defects in perovskite materials and the associated interfacial non-radiative recombination losses. Adapted from Niu et al., J. Phys. Chem. Lett. 12 (2021). (b) Diagram representing these defects from an energetic perspective, including: (1) the new energy levels introduced by localized defects, (2) the kinetics of charge trapping, and (3) the defect-induced recombination processes illustrated in a band diagram. Adapted from Jin et al., Mater. Horiz. 7 (2020).

Figure. 2.6. A schematic energy level diagram of typical hybrid halide perovskites and their charge-extraction interlayers is presented. The dotted lines indicate the work function (WF) of the materials. Adapted from Chu-Chen Chueh., Energy Environ. Sci. (8) 2015.

Figure 2.7. (a) semi log-log current and voltage curves for SCLC measurements. (b) Typical electrical Voltage Vs Current characterisation graph

57

Figure. 3.1. Schematic route of fabrication of perovskite solar cell with the addition of EDTA.

66

Figure. 3.2. (a) XRD spectra of perovskite (PVK), perovskite on TiO2 and TiO2 +EDTA films. (b,c) absorbance spectra and tau plot of perovskite (PVK), perovskite on TiO2 and TiO2 +EDTA films, and TiO2 and TiO2 +EDTA films. (d,e) Emission spectra and TRPL of perovskite (PVK), perovskite on TiO2 and TiO2 +EDTA films.



- **Figure. 3.3.** (a, b) Top-view of TiO2 and TiO2+EDTA film. (c, d) Top-view of perovskite film on TiO2+EDTA and TiO2 film respectively. (e, f) Cross-section FESEM of PSC with TiO2 and TiO2+EDTA layers 70
- **Figure. 3.4.** (a) J-V characteristics parameters of EDTA and Ref devices, inset(table for all the photovoltaic parameters of EDTA and Ref devices), (b) Continuous irradiation of EDTA and Ref devices under 1 sun, (c,d) Stability data of EDTA and Ref devices with PCE and current densities respectively, (e, f) Reproducibility statistics of EDTA and Ref devices.
- **Figure. 3.5.** (a,b) Semi log I-V curves of the EDTA and Ref devices with electron only device, (c-h) semi log J-V curves of the Ref devices with electron only device, at rt to 75°C, (i-n) semi log J-V curves of the EDTA devices with electron only device, at rt to 75°C.
- Figure. 4.1. Schematic route of fabrication of perovskite solar cell with the addition of GuSCN.

80

- **Figure. 4.2.** (a) XRD spectra of perovskite (PVK), GuSCN on perovskite films. (c) absorbance spectra and tau plot of perovskite (PVK), GuSCN on perovskite films, (b, d) Emission spectra and TRPL of perovskite (PVK), GuSCN on perovskite films. (e, f) Top-view of of perovskite (PVK), GuSCN on perovskite films, (g, h) Cross-section FESEM of PSC with conventional and addition of GuSCN layers.
- **Figure. 4.3.** (a) J-V characteristics parameters of Gu 0.5% to 3% and Ref devices, inset(table for all the photovoltaic parameters of Gu 0.5% to 3% and Ref devices), (b) Continuous irradiation of Gu and Ref devices under 1 sun, (c,d) Stability data of Gu and Ref devices with PCE and current densities respectively, (e, f) Reproducibility statistics of Gu and Ref devices 83
- **Figure. 4.4.** (a,b) Semi log I-V curves of the Gu and Ref devices with hole only device, (c-h) semi log J-V curves of the Gu device with hole only device, at rt to 75°C, (i-n) semi log J-V curves of the Ref device with hole only device, at rt to 75°C.
- **Figure. 5.1.** Schematic route of fabrication of perovskite solar cell with ETL layer different annealing stages prescribed in Type-A, B and C.
- **Figure 5.2.** (a) Conventional Device architectire for perovskite solar cells (b) XRD spectra of perovskite (PVK), perovskite on Type-A, B and C ETL annealing stages films. (b) absorbance spectra and tau plot (inset) of perovskite (PVK), perovskite on Type-A, B and C ETL films. (b)



Transmittance spectra Type-A, B and C ETL films. (e, f) Emission spectra and TRPL of perovskite (PVK), perovskite on Type-A, B and C ETL films.

95

Figure. 5.3. (a, b,c) Top-view of perovskite film on Type-A, B and C ETL annealing stages films, (g, h, i) Top-view of Type-A, B and C ETL annealing stages films, (d, e, f) Cross-section FESEM of PSC with Type-A, B and C devices.

Figure. 5.4. (a) J-V characteristics parameters of Type- A, B and C devices, inset (table for all the photovoltaic parameters of Type- A, B and C devices), (b) Stability data of Type- A, B and C devices with PCE, (c, d) Continuous irradiation of Type- A, B and C devices under 1 sun (e, f) R eproducibility statistics of Type- A, B and C devices.

Figure. 5.5. (a, b, c) Semi log I-V curves of the Type- A, B and C devices with electron only device, (d-h) semi log J-V curves of the Type-A devices with electron only device, at rt to 65°C, (i-m) semi log J-V curves of the Type-B devices with electron only device, at rt to 65°C. (n-r) semi log J-V curves of the Type-C devices with electron only device, at rt to 65°C.



List of Tables

Table 1.1. comparison table of renewable energy productions by sources including bioma	ıss,
geothermal energies for India and world. Adopted from Energy Institute statistical review	of
world energy 2024.	5
Table 3.1. Photovoltaic J-V data for the EDTA and Ref devices.	70
Table 4.1. Photovoltaic J-V data for the Gu 0.5% to 3% and Ref devices.	84
Table 5.1. Photovoltaic J-V data for the Type-A, B and C devices.	98



Symbols and Abbreviations

Å Angstrom

 Δ Heat

 ΔT Change in Temperature

 Ω Ohm

η Solar energy-to-electricity conversion efficiency

 λ Wavelength

hv Photon

σ Electrical Conductivity

ρ Resistivity

μ_h Hole-drift mobility

τ Lifetime

2D Two-Dimensional

3D Three-Dimensional

a.u. Arbitrary unit

AM Air Mass

Au Gold

B.E Binding Energy

CA Contact Angle

CB Conduction Band

cm Centimetre

CT Charge Transfer

c-TiO₂ Compact Titanium Oxide

CV Cyclic Voltammetry

DMF N, N-Dimethylformamide

DMSO Dimethyl sulfoxide

DSSC Dye-sensitized solar cell



eq. Equivalent

Ea Activation Energy

Eg/E₀₋₀ Electronic/Optical bandgap

E_{HOMO} Ground-state oxidation potential

ELUMO Excited-state redox potential

E_{onset} Onset oxidation potential

E.S Excited State

ETL Electron Transporting Layer

ETM Electron Transporting Material

eV Electron Volt

FA Formamidinium

FB Forward bias

FF Fill Factor

FE-SEM Field effect Scanning Electron Microscope

FK209 Tris(2-(1H-pyrazol-1-yl)- tertbutylpyridine)

cobalt (III) tri[bis (trifluoromethane) sulfonimide]

FTO Fluorine-doped Tin Oxide

FTIR Fourier Transform Infrared Spectroscopy

hv Photon of Energy

HOMO Highest Occupied Molecular Orbital

HTL Hole Transporting Layer

Hz Hertz

ICT Intramolecular Charge Transfer

Ip Ionization potential

ITO Tin-doped Iindium Oxide

J-V Photocurrent-voltage

J_{max} Maximum photocurrent



JSC Short-circuit photocurrent density

KHz KiloHertz

LiTFSI Lithium bis(trifluoromethane sulfonyl)imide

m-TiO₂ Mesoporous titanium dioxide

mA Milliampere

MO Molecular Orbital

mW Milliwatt

nm Nanometre

NREL National Renewable Energy Laboratory

O.D Optical Densities

OFET Organic Field-Effect Transistor

Os Oscillator strength

PCBM [6,6]-Phenyl-C61-butyric acid methyl ester

PC71BM [6,6]-Phenyl-C71-butyric acid methyl ester

PCE Power Conversion Efficiency

PEDOT:PSS Poly(3,4-ethylenedioxythiophene) polystyrene

sulfonate

P_{in} Power of the incident light

P_{max} Maximum power

PL Photoluminescence

ppm Parts per million

PSCs Perovskite Solar Cells

PTAA Poly[bis(4-phenyl)(2,4,6-

trimethylphenyl)amine]

PV Photovoltaic

R_{ct} Charge transfer resistance

R_s Series resistance



R_{sh} Shunt resistance

SC Short-circuit

SCL Space-Charge Limited Current

Spiro-OMeTAD Spiro-OMeTAD 2,2',7,7'-Tetrakis-(N,N'-di-p-

methoxyphenylamine)-9,9'-spirobifluoren

ssDSSC Solid-state dye-sensitized solar cell

TCO Transparent Conducting Oxide

TBP Tertiary butyl pyridine

DFT Density functional theory

V_{max} Maximum voltage

VOC Open-circuit voltage

VB Valence band

Z' Real part impedance

Z^{//} Imaginary part impedance



SYNOPSIS

Name of the Candidate : Mr. Rompivalasa Santhosh

Degree Registered : Ph.D. in Chemistry (18CHPH17)

Thesis Title : Harmonizing Energy: Unveiling Enhancement Strategies for

High-Efficiency Perovskite Solar Cells

Thesis Advisor : Dr. Murali Banavoth

School of Chemistry, University of Hyderabad

Gachibowli, Prof. C R Rao Road, Hyderabad-500046.

The thesis entitled "Harmonizing Energy: Unveiling Enhancement Strategies for High-Efficiency Perovskite Solar Cells" comprises of six chapters.

Chapter-1:

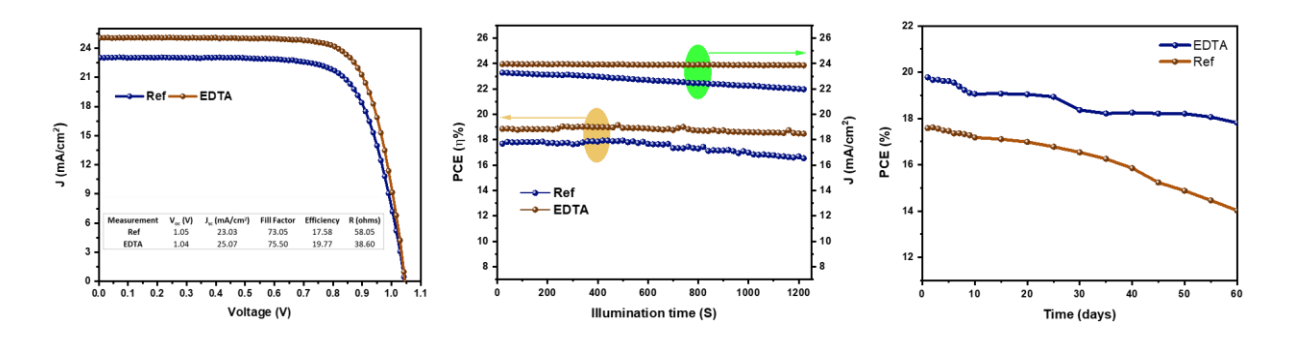
This section provides a comprehensive statistical review of energy consumption and production globally and in India. It covers the evolution of solar cells, highlighting the significance of perovskite solar cells over silicon solar cells. Additionally, it delves into the background, working principles, key properties, and advantages of perovskite solar cells. Current commercialization issues, causes of degradation, and methods to enhance the stability and durability of perovskite solar cells are discussed comprehensively.

Chapter-2:

This section presents the fundamental scientific concepts essential to this dissertation, which is primarily based on semiconductor physics with a focus on the energetics of the materials used. Key quantities are introduced and are briefly discussed, followed by an explanation of semiconductor junctions and their importance in solar cells. The principles of photovoltaics and the operation of solar cells are examined. Halide perovskite solar cells (PSCs) and their most significant characteristics are introduced, besides a discussion on crucial parameters such as power conversion efficiency, fill factor, short circuit current density, voltage at open circuit, conductivity, mobility, trap field density, and carrier density of electrons and holes, using relevant equations. The fabrication procedures, materials procured, experimental methods, and various instruments used for characterizing the samples in all the working chapters are also described.



Chapter-3:

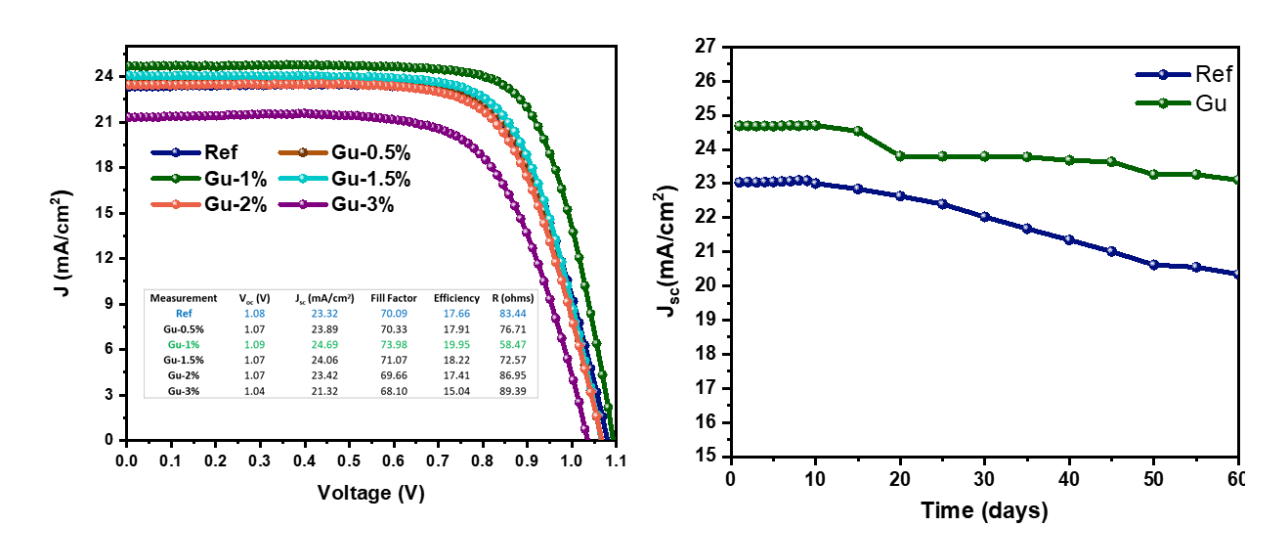


It is known that EDTA can form complexes with transition metal oxides by donating its lone-pair electrons to the vacant d-orbital of the transition metal atom. We hypothesized that EDTA-modified TiO₂ would serve as a more effective electron transport layer (ETL) in PSCs than TiO2 alone. To test this, we designed and fabricated an EDTA-TiO2 based device with the structure $FTO/c-TiO_2/m-TiO_2/EDTA/Cs_{0.05}(FA_{0.85}MA_{0.15})_{0.95}Pb(I_{0.85}Br_{0.15})_3/HTM/Au.$ $Cs_{0.05}(FA_{0.85}MA_{0.15})_{0.95}Pb(I_{0.85}Br_{0.15})_3$ was used as the active absorber due to its appropriate band gap and enhanced phase stability through Cs doping. The J-V curves of planar-type PSCs using EDTA-TiO₂ and TiO₂-based ETLs were analysed, with key parameters such as short-circuit current density (Jsc), open-circuit voltage (Voc), fill factor (FF), and PCE summarized in Table 1 (Figure (a), inset). The device with EDTA-TiO2 achieved a PCE of 19.77%, with Jsc = 25.07 mA/cm^2 , Voc = 1.04 V, and FF = 75.50. In comparison, the device with TiO_2 (reference) showed a PCE of 17.58%, with Jsc = 23.03 mA/cm², Voc = 1.05 V, and FF = 73.05. The superior performance of the EDTA-TiO₂ ETL is attributed to higher electron mobility, which enhances electron extraction, and a larger Voc due to the closer energy level alignment between EDTA-TiO₂ and the perovskite. Continuous illumination studies over 20 minutes demonstrated consistent PCE and current densities. Stability tests showed that the EDTA-TiO₂ based device retained 99% of its efficiency over 60 days, whereas the reference device with TiO₂ experienced a drop of more than 3% of its PCE. Further studies on electron-only device carrier parameters using conductivity and space-charge-limited conduction (SCLC) measurements at different temperatures confirmed the robustness of the EDTA-TiO₂ ETL even at higher temperatures. In this work, we have successfully developed EDTA-complexed TiO₂ ETLs for planar-type PSCs, achieving a PCE as high as 19.77%. Additionally, the TiO₂-based PSCs exhibited negligible hysteresis due to the elimination of charge accumulation at the perovskite/ETL interface and improved electron extraction. Furthermore, EDTA treatment rendered the TiO₂ surface more hydrophilic, reducing the Gibbs free energy for heterogeneous nucleation and resulting in higher quality perovskite films.



Chapter-4:

Employing self-assembled monolayers (SAMs) is a notable technique for interface engineering across various fields. SAMs are molecular assemblies that spontaneously form on a substrate through adsorption and typically consist of an anchoring group, a linker, and a functional group. The anchoring group enables the molecules to interact with the surface and arrange themselves in an orderly fashion, which is crucial for functionalization. The linker, often an aliphatic chain, influences the supramolecular structure via Van der Waals interactions, while the functional group plays a key role in modifying the surface properties.



Following the approach described in Chapter 3, we have fabricated a device with configuration FTO/c-TiO₂/m-TiO₂ /Cs_{0.05}(FA_{0.85}MA_{0.15})_{0.95}Pb(I_{0.85}Br_{0.15})₃/GuSCN/HTM/Au. Employing SAMs on the perovskite film is proven to be an effective method to ameliorate the PCE and long-term stability of perovskite solar cells (PSCs). In this work, the perovskite films, Cs_{0.05}(FA_{0.85}MA_{0.15})_{0.95}Pb(I_{0.85}Br_{0.15})₃, were modified with guanidinium thiocyanate (GuSCN) as a SAM. Upon introduction of the GuSCN precursor solution to the perovskite film, the crystal quality of the resulting films improved, with enhanced orientations of the (100) and (200) crystal planes. This optimization of energy level alignment benefits electron extraction. Additionally, defect density is reduced, and the charge recombination process is effectively suppressed, leading to improved PCE and stability. With the addition of 1% GuSCN to the perovskite film, the device achieved a champion PCE of 19.95%, an *Voc* of 1.09 V, a *Jsc* of 24.69 mA/cm², and a FF of 74%. This represents a 3% improvement over the counterpart without GuSCN. The enhanced Cs_{0.05}(FA_{0.85}MA_{0.15})_{0.95}Pb(I_{0.85}Br_{0.15})₃ PSC also demonstrated better stability, retaining approximately 95% of its initial PCE after being stored for over 60 days without encapsulation in a desiccator, compared to only 64% for pristine PSCs. This work provides a simple strategy



for reducing defects and improving the performance of PSCs. Further studies on hole-only device carrier parameters using conductivity and SCLC measurements at different temperatures confirmed the sustainability of the GuSCN PSCs even at higher temperatures.

Chapter-5

Organic-inorganic halide perovskites (OIHPs) have garnered significant attention in photovoltaic technology owing to their remarkable properties, such as high absorption coefficients, unprecedented long carrier diffusion lengths, ease of fabrication using solutionprocessed techniques, low optical band gaps, low recombination rates, ambipolar nature, and high charge carrier mobilities. Over the past decade, PSCs have made a linear progression, with numerous publications emerging worldwide. Currently, the PCE of perovskite solar cells exceeds 26%. Following the approach described in Chapter 3, we fabricated a device with the structure $FTO/c-TiO_2/m-TiO_2/Cs_{0.05}(FA_{0.85}MA_{0.15})_{0.95}Pb(I_{0.85}Br_{0.15})_3/GuSCN/HTM/Au.$ However, the fabrication of PSCs typically being a laborious process of almost three days, involving the hightemperature annealing required for the electron-transporting layers. We hypothesized that by reducing the annealing temperatures, the overall performance of the device could be maintained while shortening the fabrication time. To validate this, we experimented with different annealing stages for each coating of compact TiO2, mesoporous TiO2, and TiCl4 treatment. Ultimately, we achieved promising results by lowering the annealing temperatures for compact TiO2, resulting in a champion PCE of 18.03%, an Voc of 1.02 V, a Jsc of 24.08 mA/cm², and an FF of 73.46%. In this work, we have optimized the fabrication of PSCs by reducing procedural steps while maintaining performance metrics. By implementing a streamlined approach with reduced annealing temperatures for electron-transporting layers, we have accomplished decent efficiency gains compared to conventional methods. We also investigated carrier mobilities, concentrations, and trap densities at various temperatures, demonstrating the stability and performance of the PSCs under higher temperatures. This research contributes to sustainable energy solutions by paving the way for more efficient production processes in perovskite solar cell technology.

Chapter-6

Deals with the summary and conclusion of the complete thesis work, in addition, the future scopes of this work also outlined.



Chapter-1

Advancements in Perovskite Solar Cells: A Comprehensive Introduction and Analysis





Advancements in Perovskite Solar Cells: A Comprehensive Introduction and Analysis

1.1 Comprehensive Statistical Analysis of Global and Indian Energy Trends

As of recent statistics, the global energy landscape is marked by significant consumption and production shifts. The world's total energy consumption continues to grow, driven by economic development and population increase, particularly in emerging economies. In 2023, global energy consumption reached approximately 620 exajoules (EJs), with fossil fuels – oil, natural gas, and coal – accounting for about 85% of this consumption. Renewable energy sources, including solar, wind, and hydropower, have been steadily increasing their share, now contributing around 14% to the global energy mix. This transition towards renewables is crucial as nations strive to meet climate goals and reduce carbon emissions. Despite this progress, the intermittent nature of renewable sources and the existing infrastructure's limitations pose significant challenges. The data taken from the Energy Institute statistical review of world energy 2024, shown in figure 1.1.

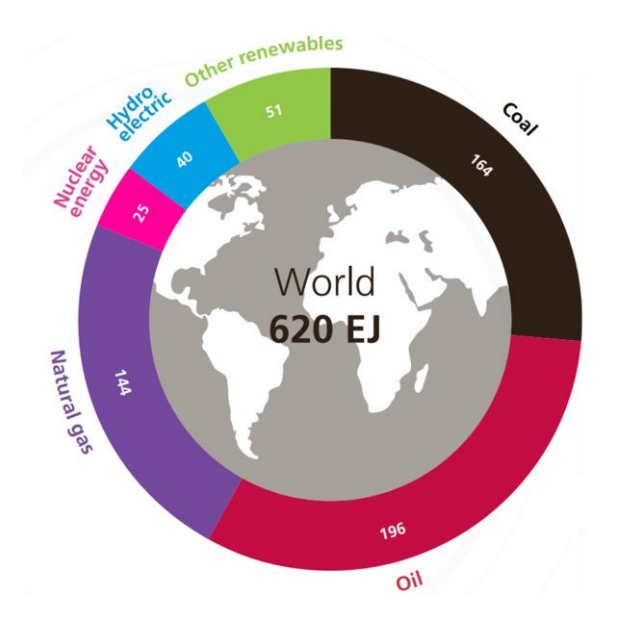


Figure 1.1. Global primary energy consumption. Adopted from Energy Institute statistical review of world energy 2024.

India, one of the world's largest and fastest-growing energy markets, has its unique set of statistics reflecting both its rapid development and the challenges it faces. The country's energy consumption has been increasing at an average rate of 4.5% per year over the past decade, reaching about 35159 petajoules (PJ) 2023. India is the world's second-largest user of





coal due to its heavy reliance on the resource, which supplies over 58% of its energy needs. This dependency is evident in the power sector, where coal-fired plants generate about 70% of the electricity. However, India is also making significant strides in renewable energy, with a target to reach 2109 gigawatts (GW) of renewable capacity by 2023 and 4500 GW by 2030. As of now, the installed renewable energy capacity stands at around 750 GW, with solar power leading the way at approximately 50 GW. The data taken from Energy statistics India 2024, Govt. of India. Shown in figure 1.2.

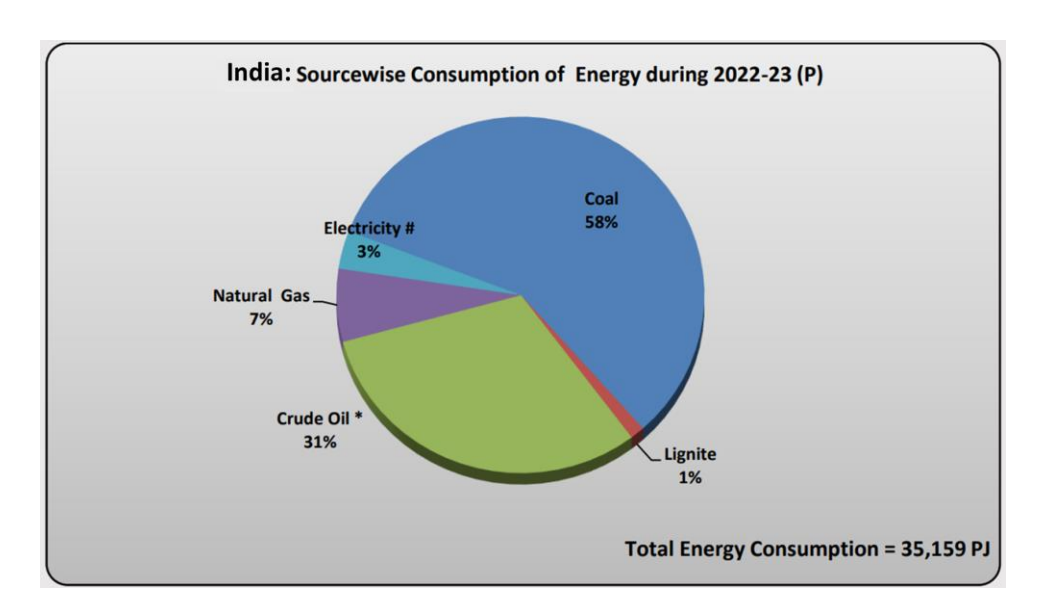


Figure 1.2. India primary energy consumption. Adopted from Energy statistics India 2024.

Globally, oil remains the dominant source of energy, comprising about 31% of the total consumption. The United States, China, and India are the top three oil consumers, accounting for nearly 50% of the global demand. Natural gas consumption is also on the rise, driven by its lower carbon footprint compared to coal and oil. The U.S. is the largest producer and consumer of natural gas, followed by Russia and China. Renewable energy, though still a smaller fraction compared to fossil fuels, is the fastest-growing energy source. Solar photovoltaic capacity increased by 32.2% in 2023, while wind power grew by 12.9%. These increases are driven by policy support, technological advancements, and declining costs. The data taken from IRENA (2024), Renewable Energy Statistics 2024, The International Renewable Energy Agency, Abu Dhabi.

In India, the government has been proactive in promoting energy efficiency and renewable energy initiatives. The Perform, Achieve, and Trade (PAT) scheme is one such initiative aimed at enhancing energy efficiency in large industries, contributing significantly to

energy savings. Additionally, the National Solar Mission, part of the broader National Action Plan on Climate Change, aims to make India a global leader in solar energy. Despite these efforts, India faces challenges such as inadequate grid infrastructure, financial constraints in the power sector, and the need to balance rapid economic growth with environmental sustainability. In conclusion, while the global and Indian energy landscapes are marked by significant consumption of fossil fuels, there is a clear and accelerating shift towards renewable energy sources. The transition is driven by the urgent need to address climate change and reduce carbon emissions. Both the world and India are investing heavily in renewable energy infrastructure and policies, although challenges remain. Balancing immediate energy demands with long-term sustainability goals is crucial for ensuring a secure and resilient energy future.

1.2 Brief Statistical Analysis of Global and Indian Photovoltaic Energy Trends

Photovoltaic (PV) energy, harnessing the power of the sun to generate electricity, has seen remarkable growth worldwide. As of 2023, the global installed PV capacity has surpassed 1,000 gigawatts (GW), marking a significant milestone in renewable energy development. This exponential increase is driven by technological advancements, decreasing costs of PV modules, and strong policy support from various governments. China leads the world in PV installations, accounting for nearly 40% of the total global capacity. The European Union and the United States follow, with substantial contributions from countries like Germany, Spain, and India. This widespread adoption is a testament to the growing recognition of PV energy as a key solution to reducing carbon emissions and combating climate change.

Photovoltaic (PV) energy, utilizing solar energy to produce electricity, has seen remarkable growth worldwide. As of 2023, the global installed PV capacity has surpassed 1,000 gigawatts (GW), marking a significant milestone in renewable energy development. This exponential increase is driven by technological advancements, decreasing costs of PV modules, and strong policy support from various governments. China leads the world in PV installations, accounting for nearly 40% of the total global capacity. The European Union and the United States follow, with substantial contributions from countries like Germany, Spain, and India. The fact that PV energy is being widely used is evidence of the increasing understanding of its importance in lowering carbon emissions and halting climate change.





In India, photovoltaic energy has also experienced rapid growth, positioning the country as one of the leading solar markets globally. As of 2023, India's installed solar capacity has reached approximately 60 GW, up from just 2.6 GW in 2014. This growth is part of India's ambitious goal to achieve 113.4 TWh of solar capacity by 2023, under the National Solar Mission. The government has implemented various policies and incentives to support this expansion, including tax breaks, subsidies, and the establishment of solar parks. These efforts have not only increased capacity but also helped reduce the cost of solar power, making it competitive with traditional energy sources.

Globally, the cost of PV electricity has decreased significantly, with the "levelized cost of electricity (LCOE)" for utility-scale solar projects dropping by over 80% in the last decade. This reduction is due to improvements in technology, economies of scale in manufacturing, and increased efficiency of solar panels. In many regions, solar power has become the cheapest source of new electricity generation. For instance, in sunny regions like the Middle East and Australia, the LCOE for solar projects can be as low as \$20 per megawatt-hour (MWh), making it more economical than fossil fuels. This cost advantage is driving the rapid adoption of PV systems in both developed and developing countries.

	2022					2022 2023					2023 Growth rate				
Terawatt-hours	Wind	Solar	Hydro	Other renewables #	Total	Wind	Solar	Hydro	Other renewables #	Total	Wind	Solar	Hydro	Other renewables #	Total
India	70.0	95.2	174.9	38.6	378.7	82.1	113.4	149.2	37.3	382.0	17.22%	19.18%	-14.73%	-3.33%	0.86%
Total World	2108.0	1321.9	4323.4	776.8	8530.1	2325.3	1641.6	4240.0	781.5	8988.4	10.31%	24.18%	-1.93%	0.61%	5.37%

Table 1.1. comparison table of renewable energy productions by sources including biomass, geothermal energies for India and world. Adopted from Energy Institute statistical review of world energy 2024.

India's solar sector is characterized by significant investments in both utility-scale and rooftop solar projects. Utility-scale projects dominate the market, contributing to the majority of the installed capacity. However, the market for rooftop solar is expanding as well, driven by initiatives such as the Solar Rooftop Scheme, It anticipates adding 40 GW of rooftop solar power by 2022. These projects are particularly important for providing energy access in rural and remote areas, where grid connectivity is limited. The combination of large-scale solar parks and decentralized rooftop systems is helping India to diversify its energy mix and enhance energy security.



Despite the impressive growth, challenges remain in the global and Indian solar markets. Grid integration of intermittent solar power, land acquisition for large-scale projects, and the need for advanced energy storage solutions are critical issues that need to be addressed. In India, financial health and policy consistency are additional concerns. However, ongoing technological innovations, supportive policies, and international cooperation are expected to mitigate these challenges and support the continued expansion of PV energy. In conclusion, photovoltaic energy is transforming the global energy landscape, offering a sustainable and increasingly economical alternative to fossil fuels. The significant progress in global and Indian solar capacity highlights the potential of PV technology to contribute to a cleaner and more resilient energy system. As the world continues to prioritize renewable energy, the role of photovoltaic power will undoubtedly become even more prominent in the quest for a sustainable future.

1.3 Perovskite Solar Energy Statistics

1.3.1 Global Perovskite Solar Energy Statistics

The excellent efficiency and low production costs of perovskite solar cells have made them a potential technology in the global solar energy landscape. As of 2023, the total installed capacity of perovskite solar cells is still relatively modest compared to traditional silicon-based solar PV, but the growth trajectory is remarkable. Laboratory-scale efficiencies of perovskite solar cells have surpassed 25%, rivalling those of silicon solar cells. Despite the early stage of commercialization, several pilot projects and small-scale installations have been deployed worldwide. Countries like China, the United States, and members of the European Union are leading in research and development (R&D) of perovskite solar technology. China, in particular, is investing heavily in scaling up production capabilities and improving the Perovskite cells' endurance and stability. The global market for perovskite solar cells is expected to grow significantly in the coming years, driven by ongoing advancements in technology and increasing demand for renewable energy solutions.

1.3.2 Perovskite Solar Energy in India

Perovskite solar cells are still in their infancy in India, but they have a great deal of promise for the future. "Indian research institutions, such as the Indian Institute of Science (IISc) and the Indian Institute of Technology (IIT)", are actively engaged in R&D to improve the efficiency and stability of perovskite solar cells. India's solar energy market is currently





dominated by silicon-based technologies, but the cost advantages and rapid efficiency improvements of perovskite cells present a compelling case for their adoption. The Indian government's focus on renewable energy and initiatives like the National Solar Mission provide a conducive environment for the advancement of perovskite technology. Pilot projects and collaborations with international research bodies are underway to explore the feasibility of large-scale deployment of perovskite solar cells. Perovskite technology has the potential to be a major player in India's energy future, given the country's abundant solar potential and the demand for reasonably priced renewable energy alternatives.

1.3.3 Comparative Insights and Future Prospects

Comparing the status of perovskite solar cells globally and in India highlights both the opportunities and challenges in scaling up this technology. The goal of significant R&D expenditures is to surmount the technological obstacles pertaining to the stability and lifetime of perovskite solar cells on a global scale. In India, the emphasis is on integrating perovskite technology into the existing solar infrastructure and ensuring cost-effectiveness for widespread adoption. The rapid advancements in perovskite research globally provide valuable insights that can be leveraged by Indian researchers and policymakers. Collaborative efforts and knowledge sharing between international and Indian research communities are crucial for accelerating the development and deployment of perovskite solar cells. As the technology matures, the unique properties of perovskites, such as their high absorption coefficient and flexibility, could revolutionize the solar energy sector, increasing its effectiveness and accessibility. The future of perovskite solar cells looks promising, with the potential to significantly contribute to the global and Indian renewable energy goals.

1.4 Evaluation of solar cells

The progress of solar cell technology has progressed through several generations, each bringing innovations that enhance efficiency, reduce costs, and expand the applicability of solar energy. From the reliable silicon-based cells of the first generation to the cutting-edge hybrid technologies of the fourth generation, these advancements reflect the dynamic and rapidly evolving field of photovoltaics, driving the global transition towards sustainable energy.¹





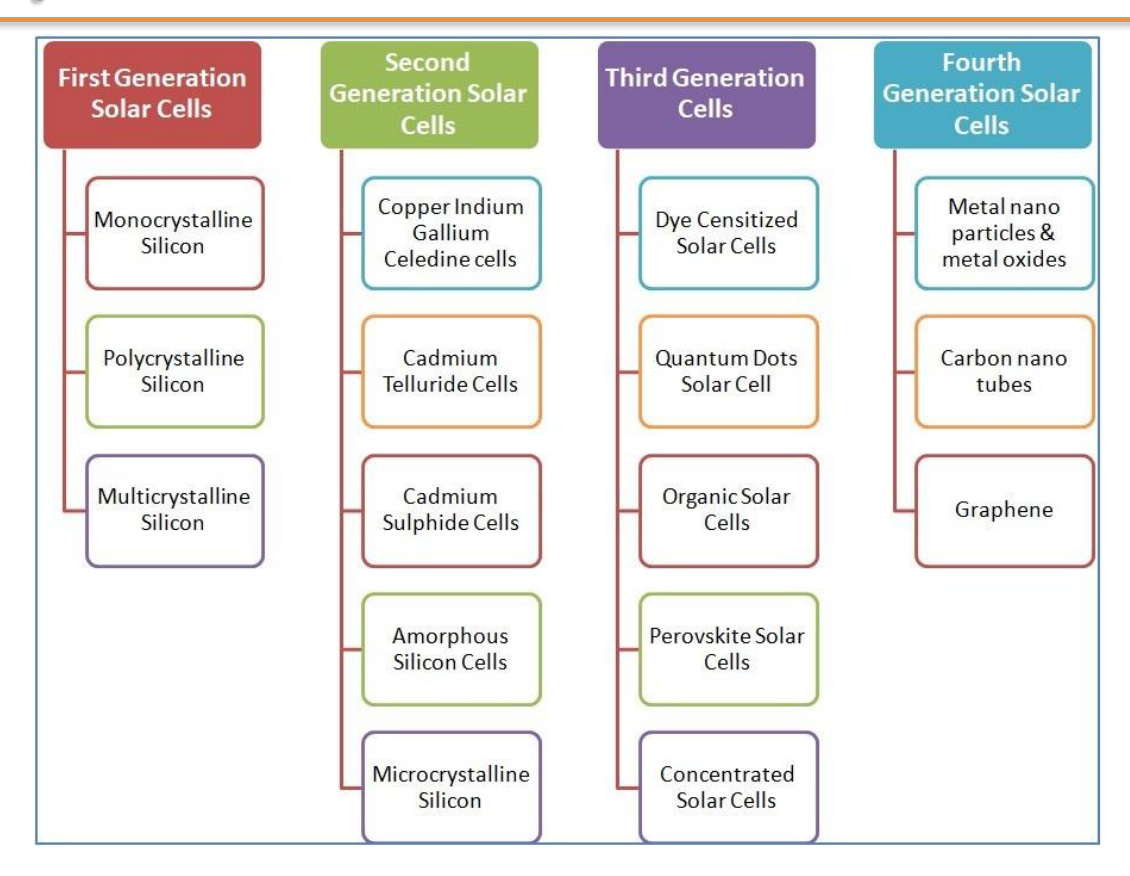


Figure 1.3. Evolution of the solar energy technology by generations.

1.4.1 First Generation Solar Cells: Silicon Wafer-Based Technology

Crystalline silicon (c-Si) technology, comprising monocrystalline and polycrystalline silicon cells, are the mainstay of first solar cell generation. Since the 1950s, these solar cells have served as the foundation for the photovoltaic industry. Although they are rather expensive to build, silicon monocrystalline cells, which are constructed from single-crystal silicon, are renowned for having a high efficiency of approximately 15-20%. Polycrystalline silicon cells, made from silicon crystals melted together, are less expensive but slightly less efficient, with efficiencies ranging from 13-16%.

First-generation solar cells are a trustworthy option for both residential and commercial applications because of their dependability and demonstrated performance. However, the quest for substitute materials and methods to lower costs and increase accessibility has been fueled by the high cost of silicon and the energy-intensive manufacturing process.

1.4.2 Second Generation Solar Cells: Thin-Film Technologies

Thin-film technologies, which seek to lower material consumption and manufacturing costs, are a part of the second generation of solar cells. "Cadmium telluride (CdTe), copper





indium gallium selenide (CIGS) cells, and amorphous silicon (a-Si) are a few examples. A substrate, such as glass, plastic, or metal, is coated with one or more layers of photovoltaic material to generate thin-film solar cells.

For a multitude of applications, including "building-integrated photovoltaics" (BIPV), amorphous silicon cells are a cost-effective and flexible alternative to crystalline silicon cells. However, their efficiency is typically lower, around 6-9%. CdTe and CIGS cells offer higher efficiencies, typically ranging from 10-12% for CdTe and 12-14% for CIGS, and have seen significant cost reductions over the years. These technologies benefit from lower material costs and the potential for large-scale, low-cost manufacturing processes.

1.4.3 Third Generation Solar Cells: Emerging Technologies

Emerging technologies that strive to exceed the cost and efficiency limitations of previous generations are incorporated into the third generation of solar cells. Organic photovoltaics (OPVs), dye-sensitized solar cells (DSSCs), quantum dots, and perovskite solar cells are some of the major advancements in this field. With above 25% efficiency in lab settings, perovskite solar cells have attracted a lot of attention because of their quick efficiency advancements. They are relatively easy to manufacture using solution-based processes, which could lead to lower production costs. However, challenges related to stability and scalability remain.

In order to turn sunlight into electricity, organic photovoltaics, or OPVs, use organic molecules or polymers. They offer the advantages of being lightweight, flexible, and potentially cheaper to manufacture. Efficiencies for OPVs have reached around 15%, and the goal of continuing research is to increase their stability and performance. Dye-sensitized solar cells (DSSCs) mimic natural photosynthesis using organic dye molecules to absorb sunlight. These cells are less efficient, with typical efficiencies around 7-12%, but they can be made with low-cost materials and processes. They are appropriate for some applications because they function effectively in low light. Quantum dot solar cells use nanometre-sized semiconductor particles to create multiple electron-hole pairs from a single photon of sunlight, potentially increasing efficiency. While still in the experimental stage, these cells show promise for high-efficiency, low-cost solar power.





1.4.4 Fourth Generation Solar Cells: Hybrid and Advanced Technologies

The fourth generation of solar cells represents a blend of previous technologies, aiming to combine the best attributes of different approaches. Stacking many layers of distinct photovoltaic materials to catch a wider range spectrum of sunlight and attain higher efficiency is known as multi-junction solar cells. Another technology in this generation is concentrated photovoltaics (CPV), which directs sunlight onto high-efficiency cells using lenses or mirrors. Perovskite cells combined with silicon or other materials is an example of a hybrid technology that aims to increase overall stability and efficiency. The goal of this research is to develop solar cells that are more resilient, cost-effective, and efficient by overcoming the constraints of individual materials.

1.5 Evaluating Silicon and Perovskite Solar Cells: Efficiency, Cost, and Application Potential

Silicon solar cells represent a well-established and reliable technology with high efficiency and durability, making them the current standard in the PV industry. Perovskite solar cells offer exciting prospects for low-cost and versatile solar energy solutions but still face significant challenges related to stability and scalability. Both technologies have unique strengths and weaknesses, and the future of solar energy will likely involve a combination of both to harness their respective advantages.²

1.5.1 Silicon Solar Cells

Silicon solar cells have dominated the photovoltaic (PV) market for decades, primarily based on crystalline silicon (c-Si), which can be either monocrystalline or polycrystalline. The superior efficiency of silicon monocrystalline solar cells, which range from 15 to 22 percent, stems from their use of single-crystal silicon. The intricate manufacturing process makes them more costly to produce, but the trade-off is better longevity and performance. When silicon crystals are fused together, however, polycrystalline silicon solar cells are produced. They are less expensive but slightly less efficient, with efficiencies ranging from 13-18%, and are easier and cheaper to produce than monocrystalline cells.

Silicon solar cells have several advantages. They represent a mature technology with a well-established production infrastructure and a long history of research and development. They are durable, with a proven track record of long-term performance, often lasting over 25





years. Over the years, silicon solar cells have achieved significant efficiency improvements, with laboratory efficiencies exceeding 26%. However, they also have disadvantages. The high-purity silicon required for manufacturing procedures and energy-intensive manufacturing techniques lead to high production costs. Higher environmental consequences are also caused by the production process, which uses a lot of energy and material.

1.5.2 Perovskite Solar Cells

Emerging technology known as perovskite solar cells has garnered a lot of interest because of its potential for low production costs and quick efficiency gains. These cells are based on perovskite-structured materials, typically hybrid lead or tin halide-based organic-inorganic compounds. PSCs have seen a dramatic increase in efficiency, rising from about 3.8% in 2009 to over 25% in recent laboratory tests, an unprecedented improvement in solar technology history.

One of the benefits of perovskite solar cells is their low manufacturing costs. This is because the cells can be produced at relatively low temperatures utilizing solution-based techniques, which drastically lowers production costs. They are versatile, as they can be printed onto flexible substrates, enabling a wide range of applications, from building-integrated photovoltaics (BIPV) to portable solar devices. Furthermore, the raw materials required for perovskite cells are more abundant and cheaper than those needed for silicon cells. However, perovskite cells also face several disadvantages. Their long-term stability and performance are affected by the fact that they are more prone to degradation when exposed to moisture, oxygen, and high temperatures. Although research is ongoing to develop lead-free perovskite materials, the use of lead in many perovskite compositions raises issues both the environment and human health. Additionally, while lab-scale efficiencies are impressive, increasing output while preserving high performance and stability remains a challenge.

1.5.3 Comparative Analysis

When comparing silicon and perovskite solar cells shown in figure 1.4, Several things jump out. Silicon solar cells have been shown to work well over the long term and have greater commercial efficiencies. Perovskite cells, while rapidly improving, still face challenges in achieving consistent and reliable efficiencies at scale. Regarding cost, perovskite solar cells have the potential for lower production costs due to simpler and less energy-intensive





manufacturing processes. Silicon cells, despite their higher cost, profit from scale economies and an established manufacturing network.

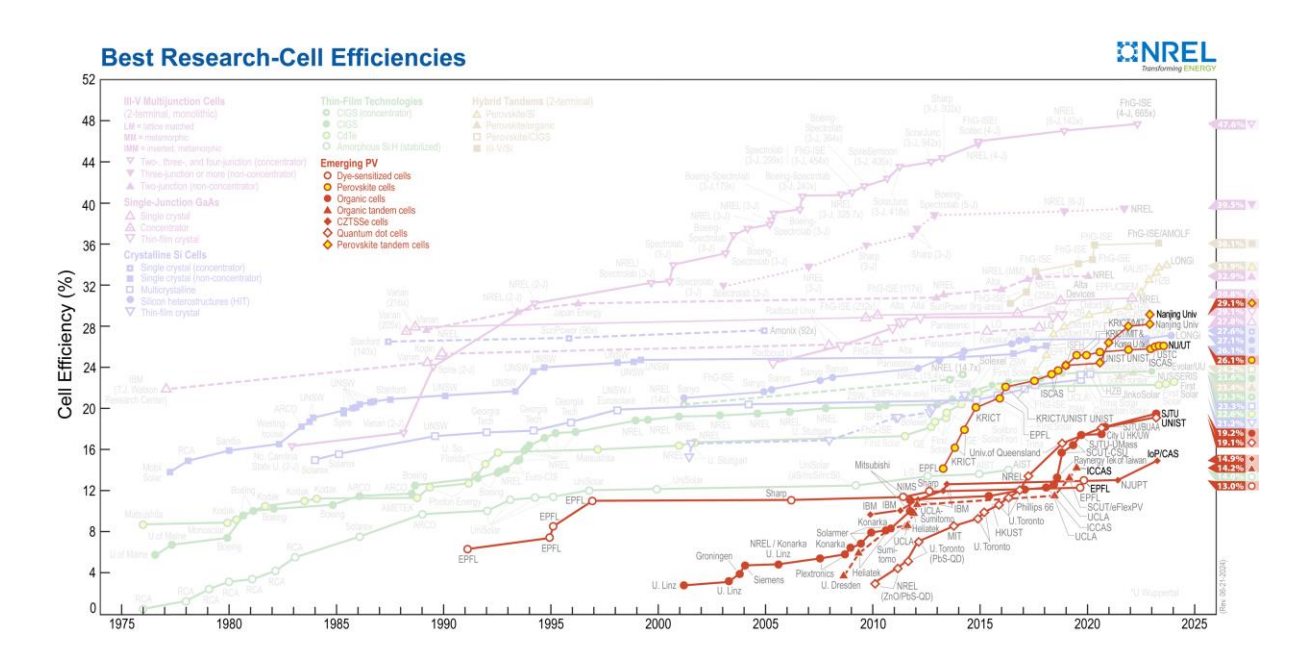


Figure. 1.4. Best Research solar cell efficiencies graph for all generations, highlighted emerging PV technology including perovskite single junction solar cells. Adopted from NREL photovoltaics research published in 2024.

In terms of durability and stability, silicon cells are known for their durability and ability to maintain performance over decades. Perovskite cells currently struggle with long-term stability but are the focus of intensive research to improve their lifespan. Regarding environmental impact, silicon cell production involves significant energy consumption and material use. Perovskite cells have a smaller environmental footprint during production but raise concerns about using toxic materials like lead. In terms of application possibilities, perovskite cells' flexibility and light weight enable new uses that are not possible for rigid silicon panels, such as incorporation into construction materials, portable electronics, and other creative applications.

1.6 Why Perovskite Solar Cells?

Due of their great efficiency, low production costs, and wide range of applications, perovskite solar cells have become a major player in the renewable energy space and have emerged as a game-changer in solar technology. To fully achieve the promise of this cutting-

edge technology and solve the remaining obstacles, research and development must continue. Perovskite solar cells have the potential to be extremely important in the global switch to sustainable energy sources as long as advancements in technology continue. Due to their distinct crystal structure, perovskites are a class of materials that are very good at converting sunlight into electrical power. Due to their significant efficiency advancements over the past ten years, perovskite solar cells have become increasingly popular. Initial versions of these cells had efficiencies of around 3.8% in 2009, but recent iterations have achieved efficiencies exceeding 26%, rivalling traditional silicon-based solar cells.³

The primary advantage of perovskite solar cells lies in their versatile and inexpensive manufacturing process. In contrast to silicon solar cells, which necessitate intricate production techniques and high-temperature processing, perovskite cells can be produced using solution-based techniques at relatively low temperatures. Because of their ability to be printed onto a multitude of substrates, including flexible materials, they may find use in everything from portable solar chargers to rooftop panels. Additionally, the raw materials used in perovskite solar cells are more abundant and cheaper than those required for silicon cells, which further reduces production costs.

Recent advancements in the stability and durability of perovskite solar cells have addressed some of the initial concerns regarding their commercial viability. In the presence of moisture, oxygen, and elevated temperatures, the early versions of these cells were prone to deterioration. However, through improved material compositions and protective coatings, researchers have significantly enhanced the longevity of perovskite cells. These improvements are crucial for ensuring that perovskite solar cells can withstand real-world environmental conditions and maintain their performance over time.

The integration of perovskite solar cells with other technologies is another exciting development. Tandem solar cells, which combine perovskite cells with traditional silicon cells, have shown potential for even higher efficiencies. Tandem cells can achieve higher efficiency levels than single-material cells by absorbing distinct regions of the sun spectrum. Additionally, developments in material science and nanotechnology are constantly broadening the potential applications of perovskite solar cells, allowing for the creation of multi-junction cells and the investigation of novel perovskite compositions with enhanced characteristics.

Even with these encouraging developments, perovskite solar cells still need to overcome some barriers before they can be generally adopted used in the commercial sector.





Issues such as long-term stability, large-scale manufacturing, and environmental impact of certain materials used in perovskite cells need further research and development. Efforts are also being made to scale up production processes while maintaining the high efficiencies achieved in laboratory settings. To overcome these obstacles and hasten the commercialization of perovskite solar cells, cooperative efforts including academic institutions, business, and governmental agencies are essential.

1.7 History and Evolution of Perovskite Solar Cells: Early Discoveries and Initial Developments

The perovskite mineral was discovered in the 19th century by Russian mineralogist Lev Perovski, which marked the beginning of the development of perovskite solar cells. Nonetheless, the utilization of perovskite materials in solar cells is a very new advancement. A major advance was made in 2009 when Tsutomu Miyasaka of Toin University of Yokohama, Japan, and his colleagues employed methylammonium lead halide, a perovskite material, as a light absorber in a dye-sensitized solar cell for the first time. With an efficiency of about 3.8%, this first cell demonstrated perovskite's potential in photovoltaics.^{4,5}

1.7.1 Rapid Efficiency Improvements

Efficiency improvements for perovskite solar cells occurred quickly between 2009 and 2012. Scientists were able to achieve approximately 6.5% efficiency by 2011 after making improvements to the cell structure. The independent reporting of efficiencies of above 10% utilizing solid-state perovskite solar cells by two distinct groups in 2012, headed by Nam-Gyu Park at Sungkyunkwan University and Henry Snaith at the University of Oxford, marked a significant breakthrough. The potential of perovskite materials to compete with conventional silicon-based solar cells was shown by these investigations. From 2012 onwards, several key innovations propelled the development of perovskite solar cells. Researchers began to experiment with different perovskite compositions, particularly by tuning the halide components (chloride, bromide, and iodide) to optimize light absorption and improve stability. The use of mixed-halide perovskites and mixed-cation perovskites allowed for better control over the material properties, resulting in higher efficiencies and enhanced stability.

In 2013, the introduction of mesoporous TiO₂ scaffolds and planar heterojunction structures significantly improved electron transport and collection, leading to efficiencies





exceeding 15%. By 2015, perovskite solar cells had achieved efficiencies of over 20%, drawing considerable attention from the scientific community and the solar industry.

1.7.2 Addressing Stability and Scalability Challenges

Early perovskite solar cells encountered major stability issues despite promising efficiency advances. The sensitivity of perovskite materials to moisture, oxygen, and thermal stress hindered their commercial viability. Researchers focused on enhancing stability through various approaches, such as using encapsulation techniques, optimizing device architecture, and developing more stable perovskite compositions. In an effort to address the health and environmental risks connected with lead-based perovskites, research into lead-free perovskites has also become increasingly important. Although lead-free perovskites have not yet matched the efficiencies of their lead-based counterparts, ongoing research continues to explore viable alternatives.

1.7.3 Recent Advances and Commercialization Efforts

Perovskite solar cell technology has advanced significantly throughout the past few years. By 2024, perovskite solar cells in lab conditions had reached maximum recorded efficiency of over 26%, which was on par with conventional silicon solar cells. The focus has also shifted towards improving long-term stability, with some perovskite cells demonstrating stable performance under accelerated aging tests.⁷

Hybrid tandem solar cells, which combine perovskite and silicon technologies, have shown exceptional promise. These tandem cells leverage the complementary absorption spectra of perovskites and silicon to achieve higher overall efficiencies, with some configurations surpassing 30% efficiency. Efforts to scale up perovskite solar cell production have intensified, with several startups and research institutions working on pilot manufacturing lines. In order to produce perovskite solar modules on a big scale and at a reasonable cost, methods including roll-to-roll printing and inkjet printing are being investigated.⁸

1.7.4 Future Prospects

Research is still being conducted to further increase the efficiency, stability, and scalability of perovskite solar cells, which bodes well for their future. "Collaborations between academia, industry, and government bodies are accelerating the commercialization of perovskite technology". By providing a flexible and affordable substitute for conventional





silicon-based solar cells, perovskite solar cells have the potential to be a major player in the global shift towards renewable energy sources, should present trends continue.⁹

To sum up, the development and history of perovskite solar cells have been characterized by quick advances and ground-breaking inventions. Perovskite solar cells were formerly a scientific curiosity, but since their discovery, they have emerged as a major player in the hunt for effective and reasonably priced renewable energy sources. The continued progress in this field holds the promise of revolutionizing the solar energy industry and contributing significantly to global sustainability efforts.

1.8 Solar Radiation and Its Components

Solar radiation is the electromagnetic energy emitted by the sun, which spans a variety of wavelengths, from infrared (IR) to visible light and ultraviolet (UV). For Earth's climate and biological systems, radiation serves as the main energy source. Understanding solar radiation and its components is crucial for designing and optimizing photovoltaic (PV) systems, as it directly impacts their performance and efficiency.

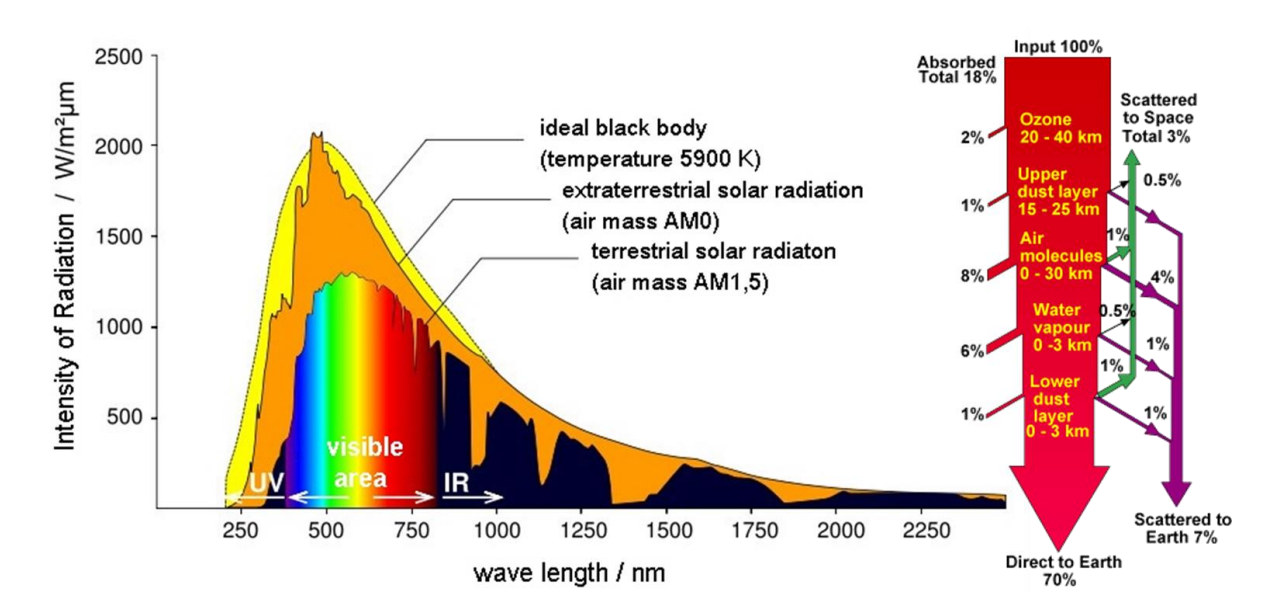


Figure. 1.5. Solar energy radiation spectrum for AM0 and AM1.5, including diffusive dust layers. Adopted from PVEducation.

Solar radiation can be broadly categorized into three main components based on the wavelength of the light:





- ➤ Ultraviolet (UV) Radiation: Wavelengths shorter than 400 nm. UVA, UVB, and UVC rays are farther separated from one another; UVC light is primarily absorbed by the Earth's atmosphere and does not reach the surface.
- ➤ Visible Light: Wavelengths between 400 nm and 700 nm. This range is where the sun's radiation is most intense and is visible to the human eye. It is also the most effective range for solar energy conversion in PV cells.
- ➤ Infrared (IR) Radiation: Wavelengths longer than 700 nm. IR radiation accounts for nearly half of the total solar energy received by the Earth and is primarily responsible for the warming effect of sunlight.

1.8.1 Air Mass (AM) and Standard Spectrum AM1.5G

Air Mass (AM) is a word used to describe the distance that solar radiation takes to pass through Earth's atmosphere. It is an indicator of the quantity of atmosphere that sunlight must travel through in order to reach the surface. The air mass is determined by the angle created by the sun's rays and the vertical direction. We call this angle the solar zenith angle.

- **AM0:** Is a common symbol for space conditions, it represents the sun spectrum outside of Earth's atmosphere.
- **AM1**: Represents the solar spectrum when the sun is directly overhead, meaning sunlight passes through one atmosphere thickness.
- **AM1.5:** However, most PV systems are not used under direct overhead sunlight. To standardize testing and comparison of solar cells, the **AM1.5** spectrum is used, depicting sunlight traveling through an atmosphere that is 1.5 times that of Earth. This condition is often regarded as representative of the average sunlight conditions in temperate latitudes, and it corresponds to a solar zenith angle of approximately 48 degrees.

1.8.2 AM1.5G and Its Importance

AM1.5G stands for "Air Mass 1.5 Global". The "G" denotes that this spectrum includes both direct sunlight and diffuse skylight scattered by the atmosphere. The AM1.5G spectrum is a standardized reference for testing and Analyzing solar cells' performance. It is defined in the international standard IEC 60904-3.





- **Spectrum Characteristics**: The AM1.5G spectrum covers wavelengths from about 280 nm to 4000 nm, with peaks corresponding to the visible light range where solar cells are most efficient.
- Irradiance: The total irradiance (power per unit area) under AM1.5G conditions is standardized at 1000 watts per square meter (W/m²). When comparing how well various PV systems operate under reliable and consistent conditions, this value is essential.

1.8.3 Application in Photovoltaic Systems

Understanding and utilizing the AM1.5G spectrum allows manufacturers and researchers to design and optimize solar cells and modules that are efficient under real-world conditions. By simulating AM1.5G conditions, they can predict how solar cells will perform in various geographic locations and climates. The standardized spectrum helps ensure that performance ratings are comparable across different products and technologies.

1.9 Perovskite Solar Cells: Background Theory and Principles

1.9.1 Background Theory

The class of materials that form the basis of perovskite solar cells shares the same crystal structure as the mineral perovskite, which is identified by the formula ABX₃. shown in figure 1.6 (a). In this structure: "A" is a cation, usually an organic molecule like methylammonium (CH₃NH₃⁺) or formamidinium (CH(NH₂)₂⁺). "B" is a metal cation, typically lead (Pb²⁺) or tin (Sn²⁺). "X" is a halide anion, such as chloride (Cl⁻), bromide (Br⁻), or iodide (l⁻). The unique properties of perovskite materials, such as high absorption coefficients, tuneable bandgaps, and excellent charge-carrier mobilities, make them highly effective for use in solar cells. To attain high efficiency and low production costs, perovskite solar cells take advantage of the special qualities of perovskite materials. Their operation is up on efficient light absorption, exciton dissociation, and effective charge transport and collection. Although challenges related to stability, toxicity, and scalability remain, ongoing research continues to advance the potential of perovskite solar cells as a revolutionary technology in the renewable energy sector.⁹





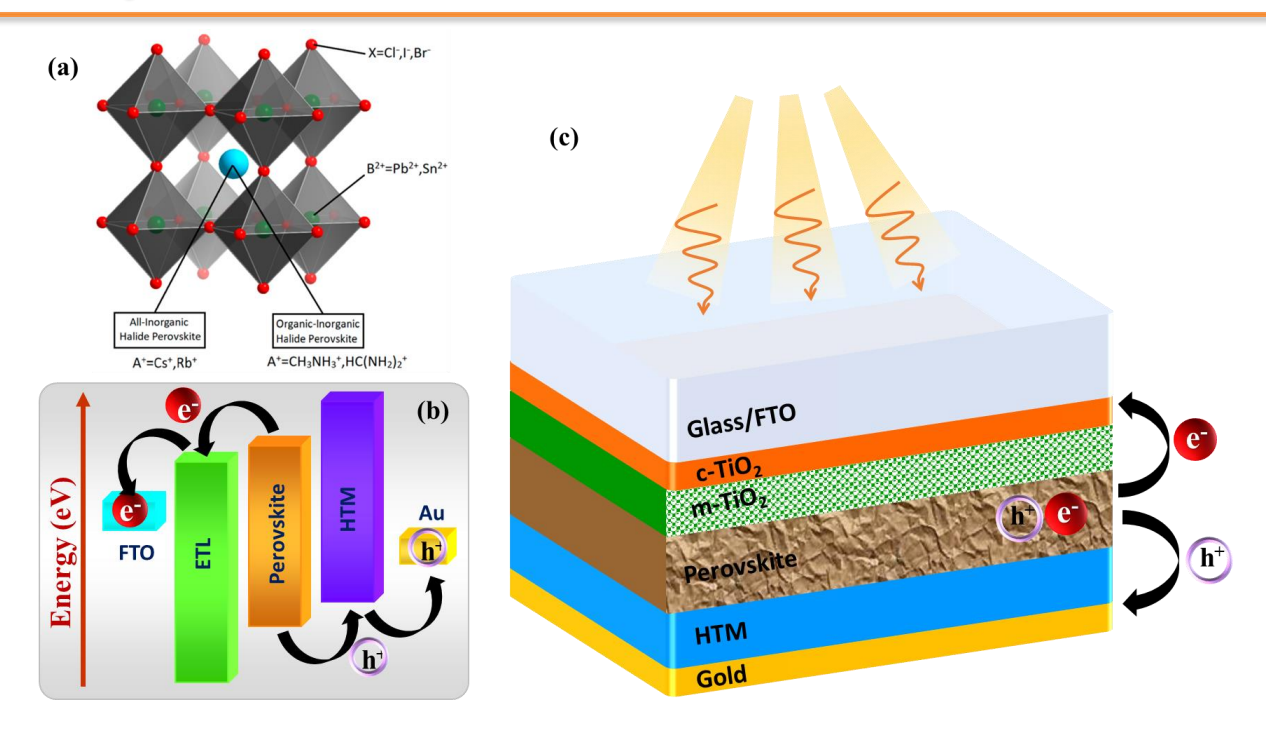


Figure. 1.6. (a) Basic perovskite crystal structure in the form of ABX_{3.} (b) Working principle for Conventional perovskite solar cells. (c) Basic architecture of mesoporous n-i-p based perovskite solar device.

1.9.2 Working Principle

The operation of a perovskite solar cell involves several key steps shown in figure 1.6 (b,c): light absorption, exciton formation and dissociation, charge transport, and charge collection.¹⁰

- Light Absorption: When sunlight hits the perovskite material, it is absorbed efficiently since perovskites have a high absorption coefficient. This absorption generates electron-hole pairs (excitons) within the material.
- ➤ Exciton Dissociation: The excitons, which are bound electron-hole pairs, must be dissociated into free charge carriers (electrons and holes). In perovskite materials, the binding energy of excitons is relatively low, which means they can easily separate into free carriers at room temperature.
- ➤ Charge Transport: Once the excitons are dissociated, the free electrons and holes are transported to their respective electrodes. Typically, a hole transport layer (HTL) and an electron transport layer (ETL) are positioned between the perovskite layer. The ETL facilitates the movement of electrons towards the cathode, while the HTL directs the



holes towards the anode. Materials like titanium dioxide (TiO₂) and phenyl-C61-butyric acid methyl ester (PCBM) are commonly used for ETLs, and spiro-OMeTAD is often used for HTLs.

➤ Charge Collection: By accumulating at the electrodes, electrons and holes produce an electric current that can be used to generate electricity. The typical architecture of a perovskite solar cell includes a "transparent conducting oxide" (TCO) like Indium/Fluorine tin oxide (ITO/FTO) on the front contact and a metal contact like gold or silver on the back.

1.9.3 Key Properties and Advantages

- ➤ **High Absorption Coefficient**: In contrast to silicon, which needs hundreds of micrometers, perovskite materials may absorb a wide spectrum of sunlight with a very thin layer, frequently less than 1 micrometer rich. This makes perovskite solar cells lightweight and flexible.
- ➤ Tunable Bandgap: The bandgap can be modified to improve the absorption of various solar spectrum regions by varying the perovskite material's composition (namely, the A, B, or X components). This tunability is particularly advantageous for creating tandem solar cells.
- ➤ Long Diffusion Lengths: Perovskite materials exhibit long electron and hole diffusion lengths, meaning the charge carriers can travel long distances without recombining. This enhances the efficiency of the cell by ensuring more charge carriers reach the electrodes.
- > Solution Processability: Techniques using low temperatures, including spin coating, spray coating, or inkjet printing, can be used to create perovskite solar cells. This makes the production process simpler and cheaper compared to traditional silicon-based solar cells.

1.9.4 Current Issues to Commercialize Perovskite Solar Cells

➤ Stability and Longevity: The stability and endurance of perovskite solar cells present one of the biggest obstacles to their commercialization. Perovskite materials are extremely susceptible to changes in temperature, oxygen content, and moisture in the environment. These components have the potential to cause the material to deteriorate





quickly, drastically shortening the solar cells' usable lives. To be commercially feasible, perovskite solar cells must ensure long-term stability equivalent to silicon-based solar cells, which usually have lifespans exceeding 25 years. Scholars are investigating many methodologies to augment stability, including but not limited to encapsulating strategies, optimizing the chemical makeup of the perovskite substance, and formulating more resilient cell structures.¹¹

- ➤ Lead Toxicity: Lead, which is hazardous to both the environment and human health, is present in a large number of high-efficiency perovskite solar cells. The toxicity of lead raises concerns about the wide-spread adoption and disposal of perovskite solar cells. Regulatory hurdles related to lead content could also impede commercialization efforts. Finding lead-free perovskite materials is a key area of study to solve this issue. Alternatives such as tin-based perovskites are being studied, but these materials currently do not match the performance and stability of their lead-based counterparts. Finding a suitable non-toxic replacement that maintains high efficiency is a critical area of ongoing research.¹²
- Scalability of Production: The expansion of perovskite solar cell production from laboratory to large-scale manufacturing is hampered by a number of issues. The fabrication processes need to be adapted for mass production while maintaining high quality and performance. Techniques such as roll-to-roll printing, spray coating, and inkjet printing are being investigated to enable cost-effective large-scale manufacturing. However, ensuring uniformity and consistency in large-scale production remains a hurdle. Additionally, integrating perovskite solar cells with existing photovoltaic manufacturing infrastructure requires significant adjustments and investments.¹³
- ➤ Cost-Effectiveness: Even while using less expensive raw materials and less complicated fabrication techniques can result in lower production costs for perovskite solar cells, scaling up cost-effectiveness remains a hurdle. The cost advantages need to be balanced against the expenses associated with improving stability, developing lead-free alternatives, and scaling up production. Ensuring that perovskite solar cells can be produced at a competitive price point compared to traditional silicon-based solar cells is essential for their commercial success. ¹³
- ➤ Performance Under Real-World Conditions: Laboratory efficiencies of perovskite solar cells have reached impressive levels, exceeding 25%. However, translating these efficiencies to real-world conditions remains a challenge. Factors such as temperature



variations, humidity, and exposure to sunlight can affect the performance of perovskite solar cells differently than controlled laboratory environments. Field testing and long-term performance studies are crucial to understand and mitigate these effects, ensuring reliable and consistent performance in various climatic conditions. ^{14, 15}

- ➤ Intellectual Property and Standardization: As the field of perovskite solar cells rapidly evolves, issues related to intellectual property (IP) and standardization become increasingly important. Ensuring that innovations are protected and that there is a clear pathway for licensing and commercializing new technologies can facilitate investment and development. Additionally, establishing industry standards for perovskite solar cells, including testing methods and performance benchmarks, is essential for gaining market acceptance and consumer trust.¹⁶
- Environmental Impact and Recycling: Crucial factors for perovskite solar cell commercialization are also their effect on the environment and their capacity to be recycled. Addressing the lifecycle environmental impact, including the extraction of raw materials, manufacturing processes, and end-of-life disposal or recycling, is important for sustainable commercialization. Developing effective recycling processes to recover valuable materials and mitigate environmental hazards associated with lead-based perovskites will enhance the sustainability profile of this technology.¹⁷

Perovskite solar cells are very promising due to their high efficiency and possibilities for low production costs; nonetheless, several significant problems must be fixed before they can be made economically viable. Enhancing stability and longevity, finding non-toxic material alternatives, scaling up production processes, ensuring cost-effectiveness, and demonstrating reliable performance under real-world conditions are key areas of focus. Addressing intellectual property issues, standardization, and environmental impact will also play a crucial role in the successful commercialization of perovskite solar cells. With continued research and development, collaboration across the industry, and supportive policy frameworks, perovskite solar cells have the potential to revolutionize the solar energy sector and contribute significantly to the global transition to renewable energy.

1.9.5 Perovskite Solar Cells: Causes of Degradation

➤ Moisture Sensitivity: The sensitivity of perovskite solar cells to moisture is one of the main factors contributing to their breakdown. Perovskite materials, particularly those containing organic components such as methylammonium lead iodide (MAPbI₃), are





highly hygroscopic and can rapidly absorb water from the atmosphere. The efficiency and lifespan of the solar cells are greatly lowered as a result of the moisture absorption, which breaks down the perovskite material into lead iodide (PbI₂), methylamine, and hydroiodic acid. This degradation mechanism necessitates stringent moisture control and effective encapsulation strategies to protect the perovskite layer.¹⁸

- Thermal Instability: Perovskite solar cells also suffer from thermal instability. High temperatures can cause the organic components within the perovskite material to volatilize, leading to the breakdown of the crystal structure. Thermal stress can also induce phase transitions within the perovskite material, resulting in a less stable and less efficient phase. These effects are particularly problematic for outdoor applications where temperatures can vary widely, underscoring the need for thermal management strategies and the development of thermally stable perovskite compositions. ¹⁹
- ➤ UV Light Exposure: Exposure to ultraviolet (UV) light can accelerate the degradation of perovskite solar cells. UV photons have enough energy to break chemical bonds within the perovskite material, leading to the formation of defects and non-radiative recombination centres. This photoinduced degradation reduces the charge-carrier lifetime and the overall efficiency of the solar cells. Additionally, UV light can degrade the organic components of the cell, such as the hole transport material (e.g., Spiro-OMeTAD). Effective UV-blocking coatings and UV-resistant materials are essential to mitigate these effects.²⁰
- ➤ Oxygen Exposure: Oxygen is another environmental factor that contributes to the degradation of perovskite solar cells. In the presence of light, oxygen can react with the perovskite material to form superoxide species, which can oxidize the organic components and lead to material decomposition. This photo-oxidation process is detrimental to the stability and performance of perovskite solar cells. Encapsulation techniques that limit oxygen ingress and the development of oxygen-resistant perovskite formulations are crucial to enhance durability.^{21, 22}
- ▶ Ion Migration: Ion migration within the perovskite layer can cause significant degradation over time. Mobile ions, such as iodide and methylammonium, can migrate under the influence of electric fields, light, or thermal gradients. This migration can lead to the formation of ion vacancies, phase segregation, and the accumulation of ions at interfaces, all of which degrade the performance of the solar cell. Controlling ion migration through material engineering, such as doping and compositional tuning, is a key focus of current research. ²³





- ➤ Mechanical Stress: Mechanical stress and strain can also contribute to the degradation of perovskite solar cells. The brittle nature of perovskite materials makes them susceptible to cracking and delamination, especially under bending or flexing conditions. This mechanical degradation is a concern for flexible and wearable solar applications. Developing flexible and resilient perovskite materials, along with robust encapsulation layers, can help mitigate mechanical degradation.²⁴
- ➤ Chemical Instability of Interfaces: The perovskite layer contacts with charge transport layers (electron transport layer and hole transport layer) are critical points of vulnerability. Chemical reactions at these interfaces can lead to the formation of interfacial defects and degradation products that reduce the efficiency and stability of the solar cell. For example, the commonly used hole transport material Spiro-OMeTAD can undergo chemical reactions with the perovskite layer, especially in the presence of dopants. Engineering stable interfaces through the use of inert interfacial layers and compatible materials is essential for improving the long-term stability of perovskite solar cells.²⁵

The degradation of perovskite solar cells is influenced by a variety of factors, including moisture, thermal instability, UV light exposure, oxygen, ion migration, mechanical stress, and chemical instability of interfaces. Addressing these challenges requires a multifaceted approach that includes advanced material engineering, protective encapsulation, stable interfaces, and environmental protection strategies. In order to improve perovskite solar cells' stability and durability and enable their wider commercial adoption as well as long-term performance under real-world settings, researchers are working to comprehend and mitigate these degradation mechanisms.

1.9.6 Perovskite Solar Cells: Methods of Increasing Stability & Durability

Encapsulation Techniques: Encapsulation is a critical method for protecting perovskite solar cells from environmental factors that cause degradation, such as moisture and oxygen. To improve the stability and longevity of perovskite solar cells, a variety of encapsulating materials and methods are being investigated:²⁶

• Glass Encapsulation: Using layers of glass to encase the solar cells provides excellent protection against moisture and oxygen. This method is widely used in commercial silicon solar panels and is being adapted for perovskites.





- Polymeric Encapsulation: Flexible and lightweight polymeric materials can be used for encapsulation. Polymers such as ethylene-vinyl acetate (EVA) and polyolefin are being tested for their effectiveness in protecting perovskite cells while maintaining flexibility.
- **Barrier Films**: Advanced barrier films that combine multiple layers of polymers and inorganic materials offer high resistance to moisture and oxygen ingress. These films can be laminated onto the perovskite cells to enhance durability.
- ➤ Material Engineering: Improving the intrinsic stability of perovskite materials through chemical and structural modifications is a key area of research:

Compositional Engineering: Modifying the composition of the perovskite material can enhance its stability. For example, replacing the organic cation methylammonium (MA) with formamidinium (FA) or cesium (Cs) can result in more stable perovskite structures.

- Additives and Dopants: Incorporating additives or dopants into the perovskite layer can improve its resistance to moisture and thermal stress. Additives such as potassium iodide (KI) and rubidium (Rb) have been shown to enhance stability.
- **2D/3D Hybrid Perovskites**: Combining two-dimensional (2D) perovskite layers with three-dimensional (3D) perovskite structures can enhance moisture resistance and overall stability. The 2D layers act as a barrier, protecting the 3D perovskite from degradation.
- > Surface and Interface Engineering: The interfaces between different layers in perovskite solar cells play a crucial role in their overall stability:
- Surface Passivation: Applying passivation layers to the perovskite surface can reduce defect densities and prevent degradation. Materials such as "phenyl-C61-butyric acid methyl ester (PCBM)" and fullerene derivatives are used for surface passivation.
- Interface Engineering: Optimizing the interfaces between the perovskite layer and the charge transport layers (electron and hole transport layers) can enhance stability. For instance, using stable materials like titanium dioxide (TiO₂) for the "electron transport layer and Spiro-OMeTAD for the hole transport layer" can improve overall device stability.





• **Buffer Layers**: Buffer layers can reduce stress and improve durability by sandwiching them between the perovskite and transport layers. Materials like zinc oxide (ZnO) and tin oxide (SnO₂) are used as buffer layers to improve stability.

Environmental Stability: Increasing the resistance of perovskite solar cells to several external influences is necessary to improve their stability in the environment:

- Thermal Stability: For perovskite materials to function well over time, their thermal stability must be improved. This can be achieved by developing perovskite compositions and device architectures that withstand higher temperatures without degradation.
- Humidity Resistance: Developing hydrophobic coatings and encapsulants that repel
 moisture can significantly enhance the humidity resistance of perovskite solar cells.
 Research is focused on creating moisture-resistant perovskite formulations and
 protective coatings.
- UV Stability: Exposure to ultraviolet (UV) light can degrade perovskite materials. Incorporating UV-blocking layers or additives that stabilize the perovskite structure under UV exposure is essential for improving long-term stability.

Advanced Manufacturing Techniques: The stability and robustness of perovskite solar cells can also be enhanced via creative manufacturing methods.:

- Low-Temperature Processing: Utilizing low-temperature processing methods can reduce thermal stress on perovskite materials, enhancing their stability. Techniques like blade coating and slot-die coating are being explored for low-temperature fabrication.
- Solvent Engineering: Developing solvent systems that enhance the crystallinity and
 uniformity of perovskite films can improve their stability. Solvent engineering involves
 optimizing the solvent composition and processing conditions to achieve high-quality
 perovskite layers.
- Sequential Deposition: Sequential deposition techniques, where the perovskite
 precursor materials are deposited in separate steps, can provide more stable and
 homogeneous perovskite films. This method allows better control over film formation
 and quality.





Passivation Techniques: Through the reduction of surface imperfections, enhancement of charge carrier lifetimes, and mitigation of non-radiative recombination, passivation techniques are essential in promoting the performance, stability, and longevity of perovskite solar cells. To overcome these difficulties, a number of passivation techniques have been developed:

Surface Passivation

Through surface passivation, the perovskite layer's surface is treated to lessen surface imperfections and trap states, which enhances charge carrier extraction and lowers non-radiative recombination. Common surface passivation techniques include:

- Self-Assembled Monolayers (SAMs): Organic molecules with functional groups that bind to the perovskite surface can be used to form SAMs. These molecules create a protective layer that reduces surface defects and improves the interface with charge transport layers.
- Inorganic Passivation Layers: Thin inorganic layers, such as metal oxides (e.g., aluminum oxide, zinc oxide) or nitrides, can be deposited onto the perovskite surface using atomic layer deposition (ALD) or chemical vapor deposition (CVD). These layers provide excellent passivation by filling surface traps and reducing recombination.
- **Polymer Coatings**: Polymers with high dielectric constants, such as poly(methyl methacrylate) (PMMA) or poly(vinyl alcohol) (PVA), can be spin-coated onto the perovskite surface to increase stability and passivate flaws.

Interface Passivation

Enhancing the interfaces between the neighboring charge transport layers and the perovskite layer is the main goal of interface passivation techniques. Effective interface passivation enhances charge extraction and reduces recombination at these critical interfaces. Common interface passivation methods include:

• Interfacial Layers: thin layers of interfacial deposit between charge transfer and perovskite layers can improve interface quality and passivate defects. Materials such as "phenyl-C61-butyric acid methyl ester (PCBM)" or fullerene derivatives are commonly used for electron transport layer passivation.





- **Dipole Layers**: The electronic structure can be changed and charge recombination can be decreased by adding dipole layers at the interfaces. Materials with high dipole moments, such as cesium carbonate (Cs₂CO₃) or lead iodide (PbI₂), are used to passivate interfaces effectively.
- **Surface Modification**: Chemical treatments or functionalization of the charge transport layers can improve their compatibility with the perovskite layer and reduce interface defects. For example, treating the hole transport layer (e.g., Spiro-OMeTAD) with lithium bis(trifluoromethanesulfonyl)imide (Li-TFSI) enhances passivation.

Defect Engineering

Defect engineering involves intentionally introducing certain dopants or additives into the perovskite layer to passivate defects and improve performance. Common defect engineering strategies include:

- **Dopants**: Adding small amounts of dopants, such as cesium (Cs), rubidium (Rb), or potassium (K), into the perovskite lattice can reduce defect densities and improve stability. These dopants can enhance the crystallinity and electronic properties of the perovskite material.
- Additives: Incorporating additives into enhancing film morphology and passivating surface imperfections can be achieved with the perovskite precursor solution..
 Additives such as ionic liquids, guanidinium thiocyanate (GuSCN), or organic salts are used to enhance perovskite film quality.
- Halide Mixing: Modifying the halide composition of the perovskite material by mixing
 different halide ions (e.g., iodide, bromide, chloride) can tailor the bandgap and
 improve stability. Halide mixing techniques optimize the crystal structure and reduce
 defect densities.

Heterojunction Passivation

Heterojunction passivation involves creating heterojunctions at the interfaces between different materials to improve charge separation and reduce recombination. Common heterojunction passivation techniques include:





- Perovskite/Perovskite Heterojunctions: Fabricating heterojunctions between different perovskite compositions with complementary bandgaps can enhance charge extraction and reduce recombination. Sequential deposition techniques are used to create multi-layered heterojunction structures.
- **Perovskite/Inorganic Semiconductor Heterojunctions**: Integrating perovskite layers with inorganic semiconductors, such as zinc oxide (ZnO) or titanium dioxide (TiO₂), can improve charge transfer and reduce recombination. These heterojunctions optimize energy level alignment and interface properties.
- **Perovskite/Organic Semiconductor Heterojunctions**: Combining perovskite layers with organic semiconductors, such as pentacene or poly(3-hexylthiophene) (P3HT), can enhance charge extraction and reduce interface recombination. These heterojunctions offer flexibility and compatibility with flexible substrates.

Conclusion

Enhancing the stability and durability of perovskite solar cells is crucial for their commercial viability. Through encapsulation techniques, material engineering, surface and interface optimization, improving environmental stability, and advanced manufacturing processes, researchers are addressing the key challenges associated with perovskite solar cell degradation. Perovskite solar cells require passivation procedures in order to function, stabilize, and last longer. The efficiency and dependability of perovskite devices are increased by passivation techniques, which also improve charge carrier lifetimes, decrease surface and interface flaws, and lessen non-radiative recombination. Continued research and development in passivation techniques will further advance the commercialization and widespread adoption of perovskite solar technology, making it a competitive and sustainable solution for renewable energy generation. Perovskite solar technology has great potential for the future of renewable energy, and these efforts are laying the groundwork for its eventual commercialization.



Chapter 2

Optimizing Perovskite Solar Cells: Materials, Methods, and Characterization Insights



This section provides an overview of the fundamental scientific ideas related to this thesis. This work's fundamentals are based in semiconductor physics, with a focus on the materials' energetics. The introduction and brief discussion of important terms is followed by a description of semiconductor-junctions and their use in solar cells. The workings of solar cells and photovoltaic principles are examined. We also present halide perovskite-solar cells and highlight some of its key features.

2.1 Semiconductor Energetic Quantities

An essential factor in optoelectronic and electronic devices where these characteristics impact overall electronic transport is a solid's energetic qualities. The important quantities that underpin the behaviours analysed in this dissertation must be presented before going into detail. Figure 2.1a presents a simplified picture of a semiconductor's basic energetics.²⁷

- **2.1.1 Bands and Band Edges:** Electron energy levels grow into electronic bands in solid materials. The lowest energy band that only becomes occupied when electrons are excited is called the conduction band (CB), whereas the highest energy band filled with electrons is called the valence band (VB). The CB's electrons are free to travel about. The energy states that are lowest in the CB constitute the conduction band minimum (CBM), and the states that are greatest in the VB form the valence band maximum (VBM). Often referred to as transport levels or band edges, VBM and CBM are essential for charge transmission. Their equivalents in organic semiconductors are the lowest unoccupied molecular orbital (LUMO) and the highest occupied molecular orbital (HOMO), according to molecular orbital theory.²⁸
- **2.1.2 Bandgap:** The energy differential between the CBM and VBM is known as the bandgap (EG). All it is really the energy needed to move an electron from the VBM to the CBM. The normal bandgap in semiconductors is between 0.5 and 4 eV. According to the momentum of the VBM and CBM, the bandgap might be either direct or indirect. There is less chance of photon absorption when an electron's momenta are different and it need both a photon and a phonon (lattice vibration) to get to the CBM. As such, compared to direct bandgap semiconductors like gallium arsenide (GaAs) and halide perovskites, indirect bandgap semiconductors like silicon require a thicker absorber layer in solar cells.²⁹



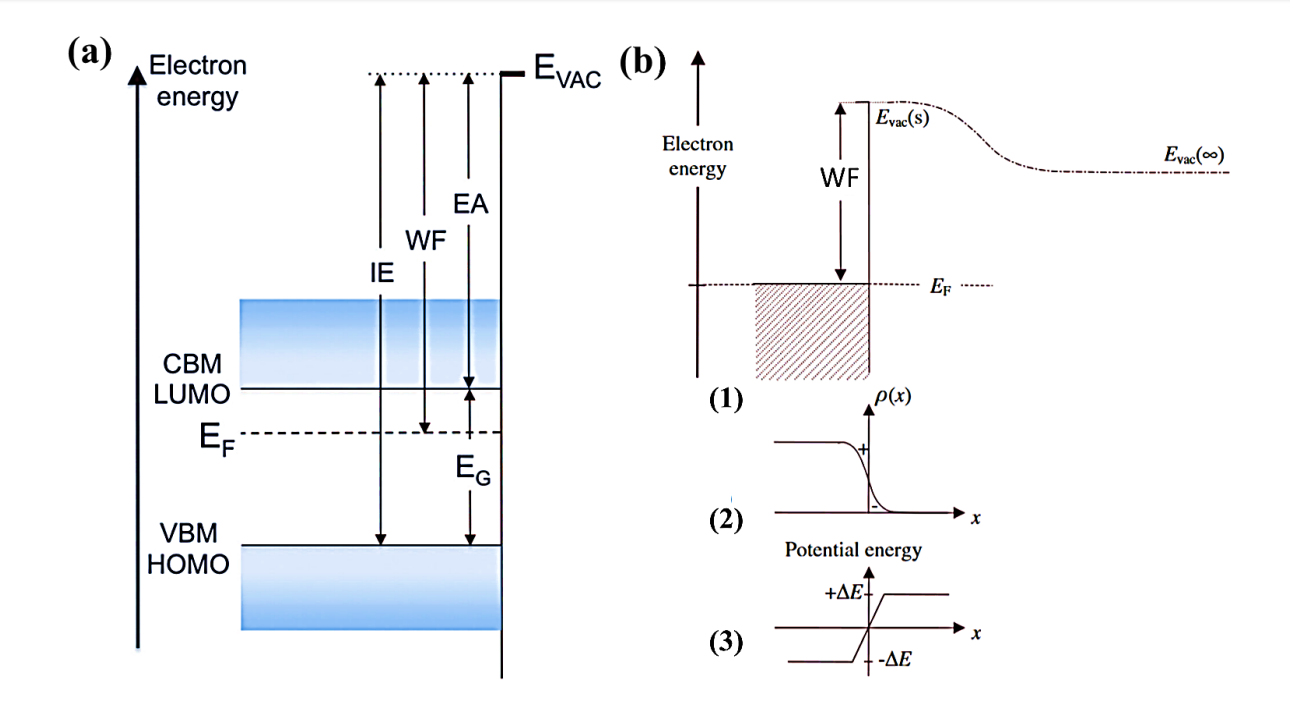


Figure 2.1. (a) Energy diagram for a semiconductor with flat bands at the surface illustrates various key energy levels and parameters, including the CBM/LUMO and VBM/HOMO, also depicts the vacuum level (E_{VAC}), the work function (WF), the energy gap (EG), ionization energy (IE), and electron affinity (EA). Adapted from Kahn A., Mater. Horiz. 3 (2016). (b) 1) The vacuum level near the surface, denoted as $E_{vac}(s)$, the work function (WF), and the vacuum level at an infinite distance, $E_{vac}(\infty)$, are depicted. The transition between these two levels indicates where the dipole field diminishes. 2) The electron distribution density, $\rho(x)$, both within and outside the solid, generates a dipole layer and influences the work function. 3) The electron potential energy step, ΔE , induced by the surface dipole, is also shown. Adapted from Cahen et al., Adv. Mat. 15 (2003)

- **2.1.3 Fermi Level:** The theoretical energy level that has a 50% chance of having an electron occupy it is called the Fermi level (EF). In semiconductors, EF is located within the bandgap and has a big impact on the material's electrical characteristics. Enhancement of electron transport occurs when EF is close to the CB, while favouring of hole transport occurs when EF is close to the VB. The material's doping concentration has the ability to change the EF.
- **2.1.4 Vacuum Level:** An electron's resting energy outside of a solid is known as the vacuum level (E_{VAC}). The surface (or local) vacuum level ($E_{VAC}(s)$) and the vacuum level at infinity ($E_{VAC}(\infty)$) must be distinguished from one another. Since it is universal to all materials in a system, $E_{VAC}(\infty)$ is a theoretical notion that cannot be evaluated empirically. It represents the



energy of an electron at rest at an infinite distance from the solid. On the other hand, $E_{VAC}(s)$, which is the energy of a resting electron just outside the solid surface, is used as a standard when measuring the energetic levels of a material through experimentation. In crystals, the local vacuum level fluctuates according to the exposed face and is affected by surface dipoles.³⁰

Figure 2.1b depicts how the E_{VAC} changes from the surface to infinity. Abrupt termination of the solid at the surface leads to electron spill out and formation of an interfacial dipole (Figure 2.1b(2)). This, in turn, raises the electron potential energy (Figure 2.1b(3)), producing E_{VAC} that progressively decays to $E_{VAC}(\infty)$. The differences between $E_{VAC}(s)$ and $E_{VAC}(\infty)$ are thoroughly discussed by Cahen et al. The term " E_{VAC} " in this dissertation refers to $E_{VAC}(s)$, unless otherwise noted.

2.1.5 Work Function: E_{VAC} and E_{F} have a close relationship with a material's work function (WF). The energy difference between E_{F} and E_{VAC} is its definition, and it is the energy needed to extract one electron from a solid. Although there are theoretically two different WFs with regard to $E_{VAC}(s)$ and $E_{VAC}(\infty)$, the relevant number is usually the local work function (WF relative to $E_{VAC}(s)$). The bulk and surface components of the WF are hard to distinguish experimentally. An extra positive or negative potential step is produced by the dispersion of dipoles and interfacial charges., which is accounted for by the surface WF. The bulk WF is predominant. When analysing the behaviour at interfaces, the surface WF is essential.

2.1.6 Ionization Energy and Electron Affinity: The energy difference between EVAC and VBM is known as the ionization energy (IE), and it denotes the energy needed to extract an electron from the VBM. On the other hand, electron affinity (EA), which is the energy obtained when an electron moves from EVAC to the CBM, is the difference in energy between EVAC and CBM. Finding the locations of the VBM and CBM, respectively, is necessary to experimentally determine IE and EA.

2.1.7 p-n junction:

Semiconductors produce junctions when two or more of them come into contact. A band diagram is produced when the previously mentioned energy quantities modify their relative positions in accordance with certain constraints. Fermi level (EF) must align upon contact, while simultaneously retaining the energy characteristics and the continuity of the vacuum level (E_{VAC}).





A key component of semiconductor electrical devices are junctions, or p-n junctions, between semiconductors with various doping types. P-doped and n-doped materials make up these junctions. Both semiconductors create a heterojunction if their materials are different, and a homojunction if they are the same. The main distinction between them, albeit having similar behaviours, is the discontinuities caused by various bandgaps between the transport bands. Frequently referred to as "cliffs" or "spikes" (Figure 2.2b), these discontinuities might form potential steps that serve as obstacles.

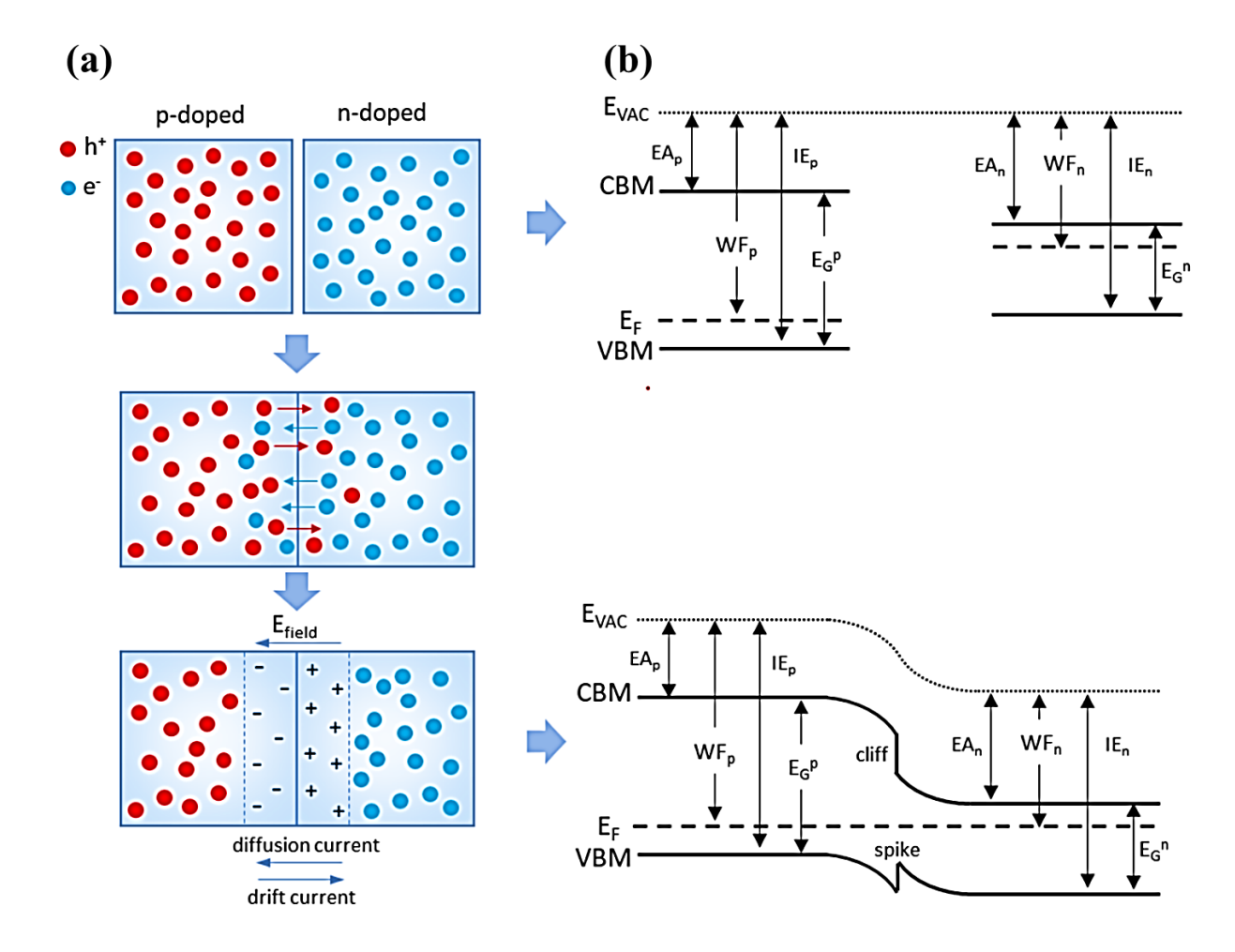


Figure. 2.2. (a) The diagram illustrates a p-n heterojunction in the dark. From top to bottom, it shows the p-doped and n-doped semiconductors before they come into contact, followed by the materials after contact where electrons and holes diffuse. This diffusion leads to the formation of a depletion region with an associated electric field (E_{field}). Additionally, both diffusion current and drift current are depicted. (b) The accompanying band diagrams correspond to the scenarios on the left. Before contact, the materials are aligned based on the vacuum level (E_{VAC}). After contact, the Fermi levels (EF) align. The diagram also includes the conduction band minimum



(CBM), valence band maximum (VBM), work function (WF), bandgap (EG), electron affinity (EA), and ionization energy (IE).

Figure 2.2 presents the band diagrams prior to and following contact as a schematic representation of the behaviour of a p-n heterojunction. The concentration of holes in a p-type material is higher than the concentration of electrons in an n-type material. As a p-n junction develops, electrons and holes move in the direction of the area that has the opposite charge until equilibrium is attained (Figure 2.2a, middle). Since the diffused carriers left behind charged dopants—that is, contaminants that are negative in the p-type semiconductor and positive in the n-type semiconductor—this leads to the formation of a depletion area, which has run out of free charges at the interface. A drift current in the other direction is produced by the depletion region's creation of an electric field that prevents additional diffusion. Equation (Figure 2.2a - bottom): When the diffusion current matches the drift current without an external bias, equilibrium is reached and a built-in potential (V_{bi}) is created across the junction. By measuring the difference in work function (WF) between the two semiconductors, this potential can be ascertained from a solar cell with that junction. Moreover, carrier concentration can be used to express V_{bi}:

$$V_{bi} = \frac{k_B T}{e} \ln \left(\frac{n \cdot P}{n_i^2} \right)$$

where n is the electron concentration in the n-type material, p is the hole concentration in the p-type material, n_i is the intrinsic carrier concentration, e is the elementary charge, k_B is the Boltzmann constant, and T is the temperature.

Photogenerated electron-hole pairs are produced when light is applied to a p-n junction. Electrons move in the direction of the n-type contact and holes move in the direction of the p-type contact due to the electric field. It is possible to extract current by connecting the contacts to an external load.

2.1.8 p-i-n Junction

When two doped layers are sandwiched between an intrinsic semiconductor layer, a p-i-n junction is created. Figure 2.3 displays the energy diagram of a p-i-n junction, showing both the condition under illumination at open circuit voltage (Figure 2.3b) and the equilibrium state (Figure 2.3a). The doped layers in a p-i-n junction control the voltage, which fluctuates linearly between them.





One Fermi level cannot adequately characterize the carrier population when the system is out of balance, as when it is illuminated. The independent electrochemical potentials of electrons and holes are instead represented by quasi-Fermi levels (E_F^n and E_F^p in Figure 2.3b). Quasi-Fermi level splitting (QFLS), which is connected to a solar cell's open circuit voltage directly, is the division of these quasi-Fermi levels under light. In this configuration, photo-induced charges are generated by the intrinsic semiconductor acting as the absorber, and these charges are then transferred through the doped layers.^{28, 30}

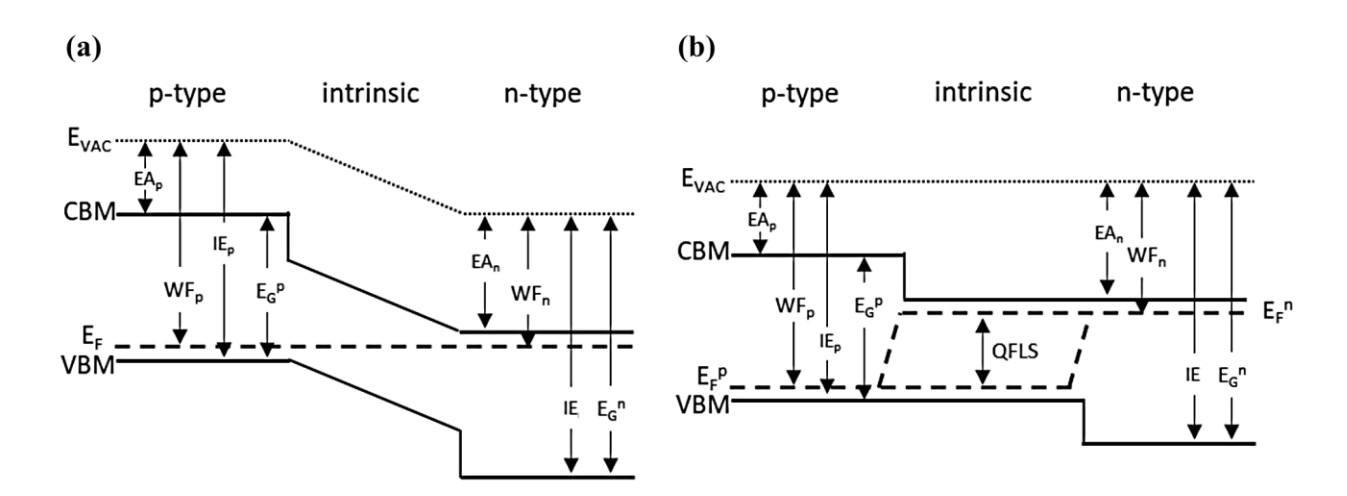


Figure 2.3. (a) A sketch of the band diagram for a p-i-n junction at equilibrium, illustrating the energy bands across the junction. (b) A similar sketch depicting the band diagram at open circuit voltage. This includes the electron and hole quasi-Fermi levels (E_F^n and E_F^p , respectively), as well as the quasi-Fermi level splitting (QFLS).

2.1.9 Solar Spectrum and Photovoltaic Effect

In open space, the sun produces radiation that travels to Earth at an intensity of 1353 W/m[^]. This process is known as nuclear fusion. Unfortunately, because to dust particle scattering and air molecule absorption, the atmosphere reduces solar irradiation. The real energy flux that reaches the Earth's surface thus fluctuates according to how far photons have to travel through the atmosphere. The optical air mass (AM), which measures this spectrum attenuation, is used to evaluate solar cells. AM1.5 is the standard value. When the sun is 48° tilted with respect to the equator, AM1.5 corresponds to the spectrum at the surface, offering an energy flux of roughly 1000 W/m².

Through the photovoltaic effect, light can be converted into electricity. A substance creates an electron-hole pair when it absorbs a photon. Although these charges would normally





recombine, In the presence of an electric field, as in a p-n or p-i-n junction, they can be gathered and extracted to generate current. The material's bandgap (E_G) must be exceeded for photon energy (hv) to be absorbed. Photons passing through the material if hv < E_G . Photons are absorbed if hv > E_G , but excited electrons relax to the conduction band and lose their surplus energy by thermalization.

2.2 Solar Cell Parameters

Characterizing the current density that emerges from applying a voltage sweep to a solar cell in either light or dark conditions is a typical way to assess the performance of solar cells. Through this method, a JV curve is produced, on which the voltage is represented on the x-axis and the current density is plotted on the y-axis. This curve offers important information regarding the photovoltaic behaviour of the solar cell. Figure 2.4 shows the essential parameters measured in light and dark, along with a standard JV curve. The four most crucial photovoltaic characteristics are fill factor (FF), maximum power point (MPP), short circuit current (Jsc), and open circuit voltage (Voc).

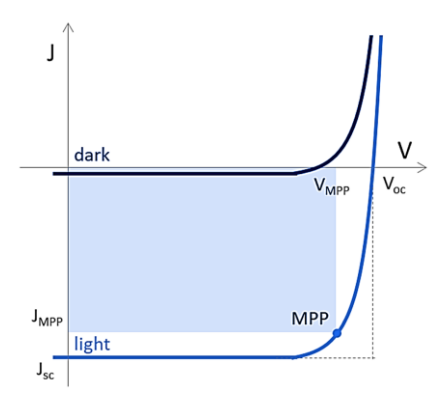


Figure 2.4. An example of typical JV curves is shown for both illuminated (light blue) and dark (dark blue) conditions. Key photovoltaic parameters are highlighted, including the maximum power point (MPP) along with its corresponding current (J_{MPP}) and voltage (V_{MPP}), the open circuit voltage (V_{OC}), and the short circuit current (J_{SC}).

- *Voc* (Open Circuit Voltage): The voltage at which the device operates with no current flowing, representing the maximum voltage achievable by the solar cell.
- *Jsc* (Short Circuit Current): The current density when the device is short-circuited, i.e., when the voltage is 0 V.



- MPP (Maximum Power Point): The point on the JV curve where the product of current and voltage yields the maximum power output of the device.
- **FF (Fill Factor):** This parameter is calculated using the formula:

$$FF = \frac{V_{MPP}J_{MPP}}{V_{oc}J_{sc}}$$

where V_{MPP} and J_{MPP} are the voltage and current at the MPP. The device's quality is indicated by the FF, which compares actual performance to an ideal scenario in which the JV curve forms a rectangle with sides representing *Jsc* and *Voc* (shown by dashed lines in Figure 2.5). While an ideal solar cell would have an FF of 1, a decent solar cell usually has an FF of 0.80 to 0.85. FF is frequently given as a percentage.

The power conversion efficiency (PCE) of the device is the ratio of the power output (P_{out}) to the input power (P_{in}) :

$$PCE = \frac{P_{out}}{P_{in}} \cdot 100 = \frac{V_{oc}.J_{sc}.FF}{P_{in}} = \frac{V_{MPP}.J_{MPP}}{P_{in}} \cdot 100$$

where P_{in} is generally 1000 W/m², as measurements are conducted using sun simulators that reproduce the AM1.5 spectrum.

The bandgap and incident spectrum are the two factors that determine the greatest theoretical efficiency of a single-junction solar cell, which is known as the Shockley-Queisser limit.³¹ The important parameter, given the standardized AM1.5 spectrum, is the bandgap. With a bandgap of 1.4 eV, a single-junction solar cell can achieve its maximum efficiency of 33.7%.

2.3 Halide Perovskite Solar Cells

Perovskite materials have a broad range of applications, particularly in optoelectronics. This section introduces these materials and their properties, focusing on their use in photovoltaics, with special emphasis on their electronic structure.³²⁻³⁷

2.3.1 Properties of Halide Perovskites

Materials that bear structural resemblance to CaTiO₃, a mineral named after mineralogist Lew Alexejewitsch Perowski and discovered by Gustav Rose in 1839, are referred to as "perovskite". ABX₃, as this structure is known, is made up of three cations: A, B, and X, which





are monovalent, divalent, and anionic, respectively. Metal sulphides (X=S), metal oxides (X=O), and metal halides (X=F, Cl, Br, I) are common forms of perovskites; the latter is of particular interest here. A unit cell is on the left in Figure 1.6a, while a popular representation with cornersharing octahedra is on the right. This represents the ABX₃ structure for the cubic form. Based on temperature and/or pressure, Orthorhombic or tetragonal formations may emerge if the structure tilts.³⁹⁻⁴¹

In metal halide perovskites, the A cation can be organic or inorganic, offering a wide range of options, such as MA⁺ (methylammonium - CH₃NH₃⁺), FA⁺ (formamidinium - (NH₂)₂CH₂⁺), Cs⁺, or Rb⁺. The B cation is often Pb²⁺, though research is shifting towards the less toxic Sn²⁺. ⁴²⁻⁴⁴ The X anion is typically I⁻, Br⁻, or Cl⁻. The electronic structure of the perovskite is directly influenced by the selection of A, B, and X ions, which enables compositional changes to adjust the bandgap (E_G). For example, replacing I- with Br- or Cl- raises E_G, whereas replacing Pb²⁺ with Sn²⁺ lowers it. Additionally influencing E_G and the lattice size is A's size. E_G can vary between around 1.2 eV and 3.5 eV thanks to its tunability. ^{45, 46} An overview of the impact of composition differences on energetics is given in Figure 2.6. In general, the orbitals of the A cation reside deeper inside the bands, whereas the metal and halides contribute to the energy of the band edges. Pb(6s) and I(5p) orbitals specifically determine the valence band maximum (VBM) whereas Pb(6p) orbitals determine the conduction band minimum (CBM).

The stability of the ABX₃ structure is predicted by the Goldschmidt tolerance factor, defined as:

$$t = \frac{R_A + R_X}{\sqrt{2}(R_B + R_X)}$$

The ionic radii of A, B, and X are denoted as R_A, R_B, and R_X, respectively. Based on their ionic radii, the tolerance factor can be used to forecast which combinations of materials will create a stable ABX₃ structure. If the tolerance factor is between 0.8 and 1, a stable 3D perovskite structure may usually be obtained. This factor allows for the formation of perovskites with various ions, leading to systems that offer both optoelectronic tunability and complex stoichiometry.





2.4 Role of Interfaces in perovskite solar cells

An integral part of any solid-state device is its interface. At the junctions where various materials come together, scientists have noticed variations from Ohm's law ever since the invention of semiconductor devices in the late 19th century. These anomalies were soon attributed to the contact itself, though it took another 50 years to fully understand the underlying phenomena.

The fundamental problem is that surfaces are uneven and have hanging bonds when a material terminates abruptly. Surface states, potential chemical reactions, and changes to the material's energetics and structure can all arise from this. Thus, a material's characteristics and a device's functionality are largely determined by their interfaces.

PSCs, or hybrid organic-inorganic solar cells, hold considerable significance in this regard. At the interface with adjacent layers, which include both organic and inorganic components, the perovskite absorber, which is made up of many elements and molecules in a complex stoichiometry, results in numerous surface terminations. Furthermore, different methods might result in distinct characteristics and faults in perovskite films.

There are multiple interfaces between these materials or with the external environment, and a typical PSC is made up of a stack of five layers: a TCO substrate, an ETL, an HTL, and a conductive metal contact. And because of interlayers, more interfaces can appear. Grain boundaries with varying visible facets and surface terminations are examples of additional interfaces that are typically introduced by the polycrystalline nature of the perovskite layer.

Consequently, several and intricate interfaces are involved in PSCs, particularly at the interfaces where the perovskite and surrounding layers meet. These have a substantial effect on the stability and performance of the solar cells since the devices' electrical and transport characteristics are determined by the junctions between semiconductors and metals, as well as their exposed surfaces.

Further details on these interfaces and their implications for charge transport, particularly between the perovskite and later layers, will be covered in the sections that follow.

2.4.1 Features of Perovskite and Its Surface

2.4.1.1 Defects and Recombination





Typically, extrinsic and intrinsic types of perovskite faults are distinguished. The origin of extrinsic defects is usually undercoordinated atoms at the grain boundaries and surface that interact with the surrounding material or other layers. It is thought that non-radiative recombination losses in PSCs are mostly caused by these flaws. Mostly, these shortcomings will be addressed in the experimental part of this dissertation.

Crystallographic flaws within the lattice that are sometimes referred to as vacancies, antistites, and interstitials are known as intrinsic, or native, point defects. Atoms that live in between lattice sites produce interstitials, antistites when they occupy the wrong site, and vacancies when an atom is absent from its lattice site. In the specific case of MAPbI3, there are 12 native point defects, including MA, Pb, and I vacancies and interstitials, as well as andesite occupations like MAPb, MAI, PbMA, PbI, IMA, and IPb.

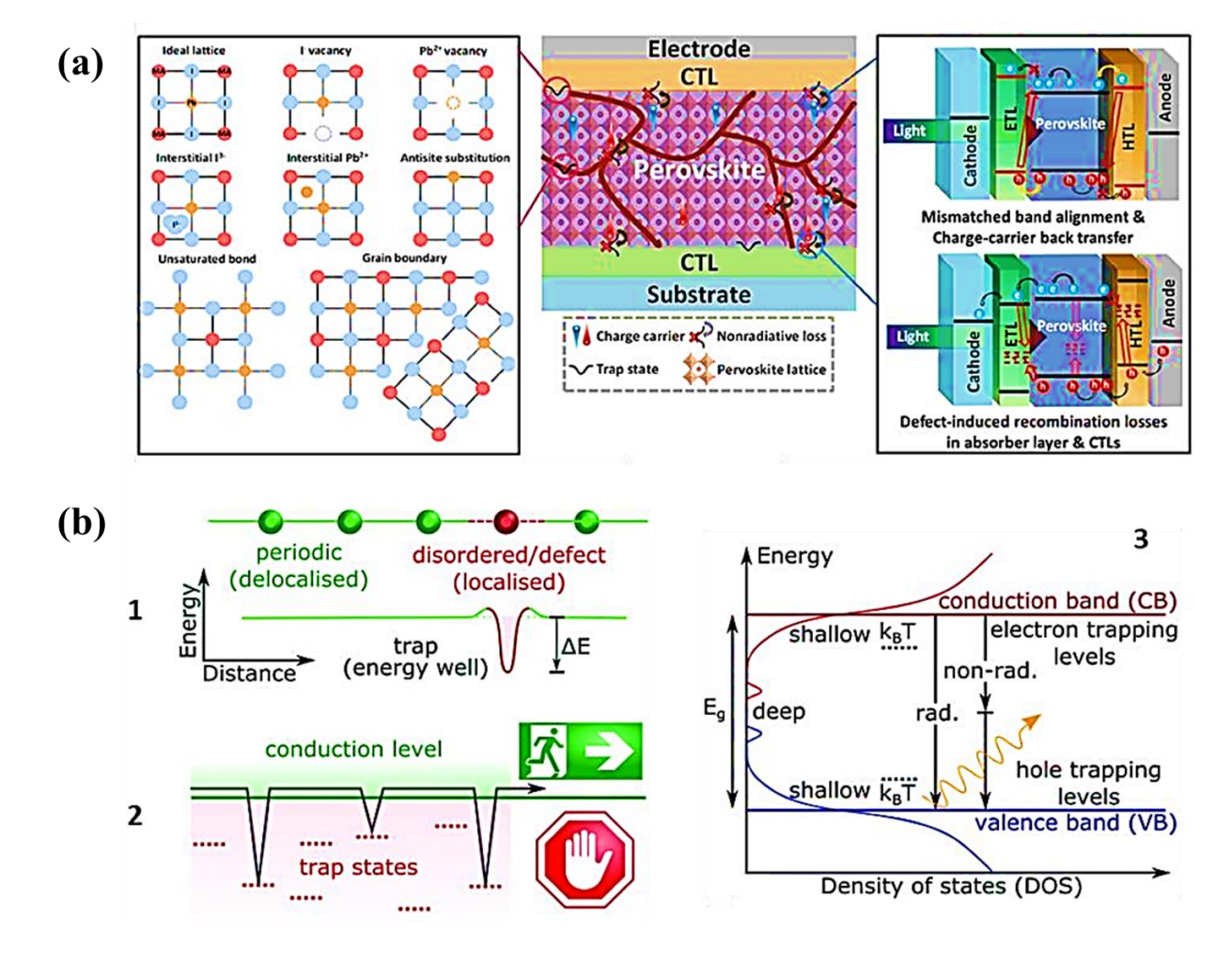


Figure. 2.5. (a) Illustration depicting the primary defects in perovskite materials and the associated interfacial non-radiative recombination losses. Adapted from Niu et al., J. Phys. Chem. Lett. 12 (2021). (b) Diagram representing these defects from an energetic perspective, including:



(1) the new energy levels introduced by localized defects, (2) the kinetics of charge trapping, and (3) the defect-induced recombination processes illustrated in a band diagram. Adapted from Jin et al., Mater. Horiz. 7 (2020).

Unlike at the conduction and valence band boundaries, defects have different energy levels. Charges are not expected to inhabit these states, thus if these energy levels are outside the bandgap, they usually do not cause an issue. Nonetheless, free carriers may fall into these traps and undergo recombination if the defect energy levels are inside the bandgap but above or below the valence band edge. Their depth within the bandgap determines how these faults behave. In shallow defects, trapped charges can escape with some additional energy, usually supplied thermally or optically. These defects have energy levels near the band boundaries. By means of trapping-detrapping processes, these flaws mainly hinder carrier movement, hence decreasing effective mobility.

In contrast, deep defects within the bandgap significantly increase the likelihood of recombination, as the probability of re-emission is low. It is possible for trapped electrons or holes to recombine with their counterparts and release a phonon rather than a photon. This process is referred to as trap-assisted recombination, or Shockley-Read-Hall (SRH). In all semiconductor applications—including solar cells—this is an essential loss mechanism. Additional recombination processes encompass Auger recombination and band-to-band recombination, which is typically radiative. These recombination processes are often described using a simplified rate equation:

$$\frac{dn}{dt} = -k_1 n - k_2 n^2 - k_3 n^3$$

Where dn/dt represents the rate at which carriers' decay, n is the charge carrier density, and k_1 , k_2 , and k_3 are the rate constants for the three recombination processes, respectively. Surface defects and dangling bonds draw electrons and holes, causing more recombination to occur at the site, which makes it a high-recombination site. Usually a kind of SRH recombination, surface recombination leads to first-order recombination that depends linearly on the charge carrier density n.

The velocity of free carriers moving towards the surface, denoted as S, is what defines surface recombination. "This recombination also depends on diffusivity (D) and thickness (d). The surface recombination coefficient (k_s) can be expressed as:



$$k_s = \left(\frac{4d^2}{\pi^2 D} + \frac{d}{s}\right)^{-1}$$

where the first term accounts for the time needed to diffuse to the surface and the second for the actual recombination." The recombination losses in thin-film solar cells are mostly caused by surface recombination, which frequently predominates over bulk recombination. Surface passivation is a common technique to mitigate these losses.

2.4.1.2 Ion Migration

One well-known property of perovskites is that they migrate ions as ionic crystals. If bias is applied or the material is exposed to light, the ions can migrate within it, causing defects and aggregating at transitions. Diffusion or a bias resulting from a differential in the concentration of available vacancies might propel ions towards migration. Diffusion and field-induced migration shall both be referred to as "ion migration" in this discussion.

To comprehend and describe ion migration, a great deal of research has been done. Although activation energy figures vary throughout research, it is generally agreed upon that iodides comprise the majority of mobile ions because of their low activation energy. Pb²⁺ ions, on the other hand, have very high activation energies and exhibit relative stability at their locations. Despite their slow migration, MA⁺ ions can also have significant activation energies. Since MA⁺ defects do not create deep traps, they are usually not dangerous; however, excision of these defects may change the crystal structure and cause deterioration.

Mobile ions move across the material in response to a bias or light exposure, leaving behind charged vacancies or defects that have the potential to become recombination centres. The built-in electric field is partially screened and carrier collection is adversely affected by the accumulation of these migrating ions at the interfaces with charge transport layers (CTLs). This makes recombination worse and is a big reason why JV curves hysteresis. Remarkably, Domanski et al. showed that if devices are exposed to darkness for a little amount of time—like one night—ion migration losses can be regained. This implies that PSC applications in the real world, which experience natural day-and-night cycles, can make up for these losses during night.

2.4.1.3 Hysteresis

In JV curves, hysteresis in perovskite solar cells is seen as a difference between backward and forward scans. The second scan frequently reveals decreased efficiency when hysteresis is





present, mostly as a result of a lower fill factor (FF) and occasionally a lower open-circuit voltage (*Voc*). In addition to highlighting this issue, Snaith et al. (2014) pointed out that hysteresis is dependent on other parameters, including device architecture and scan rate. Comparing devices from different laboratories is challenging due to this diversity. Maximum power point (MPP) tracking, which evaluates efficiency variations over longer periods (usually at least 100-200 seconds) to account for transient effects owing to ion migration, is advised to supplement JV curves with stable power outputs in order to achieve trustworthy results.

Presently, hysteresis is thought to be mostly caused by ion migration, specifically halide ion moving. Although they were eventually ruled out as potential explanations, a high defect density in the perovskite and its ferroelectric characteristics were also raised. Debye layers are thin, charged layers that occur at the CTL interfaces when ions migrate across the perovskite absorber due to bias or light exposure. Charge transport may become inefficient as a result of the extra electric field produced by these layers opposing the inherent electric field. As migrating ions respond slowly and are unable to redistribute rapidly enough, hysteresis happens. Ions do not have enough time to respond at high scan rates, resulting in minimal harm; at low scan rates, ions can redistribute without producing hysteresis. Nevertheless, considerable hysteresis is seen at moderate scan rates.

While several theoretical investigations have supported the connection between ion migration and hysteresis, it is difficult to obtain experimental proof. To study ion migration, methods such as galvanostatic tests, impedance spectroscopy, and Kelvin probe force microscopy have proven helpful. Charge accumulation at interfaces may contribute to hysteresis, according to certain research, implying a correlation between ion movement and this phenomenon. Hence, it needs more research to fully comprehend the intricate mechanisms underlying hysteresis.

Hysteresis and interfaces are generally tightly related, and ineffective charge transport is caused by bad junctions. Greater grain sizes and surface passivation are two treatments that can lessen this and improve charge carrier extraction. Enhancing the qualities of the nearby CTLs is an additional strategy. For PSCs to work, the interactions with neighbouring layers are essential.

2.4.2 Interaction of Perovskite with Adjacent Layers

It is important to take into account how perovskite materials interact with other layers in a device while analysing their surfaces in particular. Placement of perovskite films usually involves sandwiching them between two electrodes and two charge transport layers (CTLs). Due





to their influence on charge transport and the extraction of photogenerated carriers, these materials' characteristics and interactions are critical to the operation of devices. The following are essential traits of a successful CTL:

- a. High optical transmittance to minimize optical losses and maximize absorption in the perovskite layer.
- b. High electrical conductivity to enhance charge transport.
- c. Absence of pinholes to prevent current leakage and shunting.
- d. Well-matched energy level alignment (ELA) for efficient charge transport and minimal energy loss.

Energy level alignment is a crucial component for interfaces and will be the main topic of discussion in this conversation. Although achieving and assessing ELA can be difficult, it has a substantial impact on charge transfer and is intimately related to recombination.

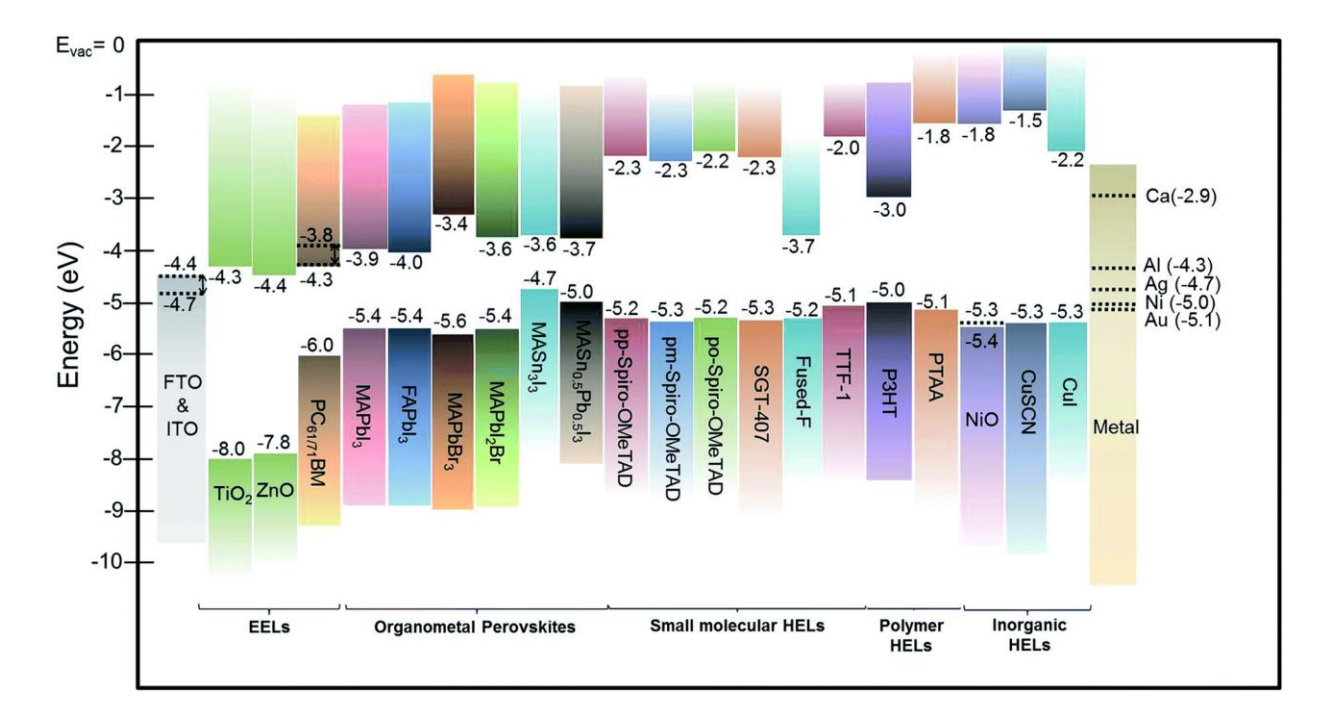


Figure. 2.6. A schematic energy level diagram of typical hybrid halide perovskites and their charge-extraction interlayers is presented. The dotted lines indicate the work function (WF) of the materials. Adapted from Chu-Chen Chueh., Energy Environ. Sci. (8) 2015.

The optimal configuration of layers is described in Section 2.9. Electrons go along CBM/LUMO levels toward lower energy, while holes travel along VBM/HOMO levels toward





higher energies, like a "staircase." Injectable and extraction barriers are the two primary kind of obstacles that might impede the transmission of charge. When the perovskite and CTL are not aligned properly, an extraction barrier forms, which stops the majority charges from flowing. The device would display lower FF and current loss near *Voc*, for instance, if the perovskite VBM is higher than the HTL HOMO level. When the perovskite and CTL have a large offset, like the HTL HOMO level being significantly higher than the perovskite VBM, an injection barrier is present. This results in *Voc* loss and restricts the quasi-Fermi level splitting. For effective charge transfer, therefore, it is essential to have energy levels that are effectively matched with suitable offsets.

Note that every material in a stack has two different kinds of interfaces: the top interface and the buried interface, or bottom and bottom, respectively. Variations in defect structures and electronic alignments result from the different formation processes of these contacts. The subsurface substrate is essential to the buried interface because it serves as a template for the material's growth. In contrast, the subsequent layer's formation occurs at the top interface. When this interface is accessible, it can communicate with more complicated layers or external agents. The CTL to be placed on top must also be carefully chosen because not all deposition techniques are appropriate for perovskite. Therefore, extra care and optimization are needed for the top interface.

2.4.3 Energy Level Alignment and Charge Transport

In perovskite solar cells (PSCs), the open-circuit voltage (*Voc*) is greatly influenced by the energy level alignment (ELA) at the interface between the perovskite and surrounding layers. In an ideal scenario, *Voc* would coincide with the quasi-Fermi level splitting (QFLS) in the absorbing layer, which happens when the quasi-Fermi levels (QFLs) may flow freely from the perovskite to the contacts. But considerable offsets at the interface for majority carrier transmission and interfacial recombination lead the QFL to bend, which results in a mismatch between QFLS and *Voc* and lowers the external *Voc*. Smaller offsets let the QFLs to remain flat, eliminating *Voc* loss; this effect is especially visible when the offset approaches 200 meV.

For instance, simulations and experiments across a variety of common perovskite compositions consistently show a QFLS-*Voc* mismatch due to energy level offsets in a p-i-n device with an offset between the perovskite valence band maximum (VBM) and the hole transport layer (HTL) (specifically, poly(triaryl)amine - PTAA) highest occupied molecular





orbital (HOMO) level. Non-radiative recombination, which is also brought on by misaligned energy levels, increases the charge carrier density in the CTLs exponentially and leads to interfacial recombination. Any offset is directly correlated with a *Voc* loss since *Voc* is logarithmically dependent on the recombination rate.

Consequently, CTLs impair device performance by causing *Voc* losses and extra non-radiative recombination. Research has revealed that the largest the perovskite interface at the top is where energy losses occur. This has been demonstrated by analysing the Comparing QFLS and *Voc* measurements for both n-i-p and p-i-n stacks, as well as the top and bottom perovskite interfaces. To show this, picture a bucket of water with holes in it to represent recombination losses and the water level representing the feasible *Voc*. In high-performing devices, the interface between the perovskite and the uppermost transport layer experiences the most loss. Bulk recombination within the material, however, may take precedence if the perovskite is severely deficient. Therefore, before attributing alterations to specific modifications, it is imperative to establish the primary loss route.

Although ELA's influence on *Voc* is highlighted in this article, other factors also have an impact on this metric. *Voc* losses are largely caused by defects, particularly those that result in bulk recombination or interface recombination. Thus, there are multiple approaches to interface optimization for *Voc* maximization: (i) matching energy levels, (ii) perovskite material optimization, and (iii) passivation to minimize interfacial recombination losses.

2.4.4 Functionalization as a Strategy

As discussed earlier, the perovskite layer is a polycrystalline film containing various surface and bulk defects. These imperfections generally impair device functionality, leading to issues like recombination or ion migration, and negatively impacting both efficiency and stability. Deeply within the bandgap faults are the most troublesome because they lead to non-radiative recombination. Although shallow flaws usually cause less damage, they have the ability to move across layers and cause unwanted charge accumulation or hysteresis. As a result, removing these flaws and reducing ion movement are essential. Using compounds that can interact with these imperfections, defect passivation is the most often used technique to remedy this.

Defects frequently contain positive or negative charges due to the ionic nature of perovskites. These flaws can be deactivated by a number of passivation techniques, including conversion, ionic bonding, and coordinate bonding. Conversion is the process of chemically





changing grain boundaries and surface to create a material with a larger bandgap, which removes flaws and produces an ELA that is more advantageous. Anions and cations can act as ions' passivators on the perovskite surface by the transfer of valence electrons between atoms during ionic bonding. The coordinate bonding technique, in order to create a Lewis, adduct, two electrons from the same atom must be shared, will be covered in this section.

2.4.5 Coordinate Bonding: Lewis Acids and Lewis Bases

An electron pair that can be donated by one molecule to another to create a dative bond and produce a Lewis adduct is known as a Lewis base. An electron pair from a Lewis base can be accepted by a molecule with an empty orbital, so creating a Lewis adduct, in contrast to a Lewis acid. Numerous unpaired electrons or holes form dangling bonds at the perovskite surface due to the abrupt interruption of the crystal structure. One can frequently find, for example, Pb2+ ions with a positive charge or halide ions with free negative charges. Use of Lewis acids or bases to passivate these flaws has worked well.

The broad spectrum of compounds that are suitable for passivating Pb²⁺ ions make Lewis base functionalization especially appealing. With lone pairs of electrons to share with Pb2+ ions, molecules containing nitrogen, sulphur, oxygen, or phosphorus in their functional groups are effective. Noel et al. first introduced this technology to the PSC sector by treating the perovskite surface with thiophene and pyridine. They later refined this process utilizing the derivatives of these compounds. Trioctylphosphine oxide (TOPO), which demonstrates the benefits of passivation with oxygen and phosphorus, is a very effective molecule in decreasing recombination. Its practical use in electronics, however, might be restricted by the lengthy insulating aliphatic chains of TOPO.

For passivating halide ions, employ lewis acids. The term "Lewis acid-like molecules" is more correct when referring to perovskite functionalization, though. Their ability to receive electrons is what allows these compounds to interact with halide ions rather than the existence of an empty orbital. Because of their spherical form and aromatic characteristics, fullerenes, for example, are useful "Lewis acids" that draw electron density from halide ions. A molecule that can form a halogen bond is an additional example. It interacts with halide ions on the perovskite surface by having a small positive electrostatic potential area. In the next section, this kind of link will be thoroughly explained. It is especially significant for this dissertation. Lewis acids are used for passivating halide ions. However, in perovskite functionalization, it is more accurate to





refer to molecules that behave like Lewis acids. These molecules interact with halide ions not due to the presence of an empty orbital, but because of their electron-accepting capabilities. For instance, fullerenes are effective "Lewis acids" that attract electron density from halide ions due to their aromatic properties and spherical shape. Halogen bonding molecules, which have a small positive electrostatic potential region and interact with halide ions on the perovskite surface, are another example. The next section will provide a detailed description of this particular bond, which holds significant importance for this dissertation.

2.4.6 Halogen Bonding:

Due to their strong electronegative nature, halogens have a high electron density and can interact attractively with other atoms by acting as electron donors, or nucleophiles. On the other hand, the electron density turns anisotropic when a halogen (X) forms a covalent link with another element (R). The three pairs of unshared electrons make up the majority of the electron density, which is formed into a belt around the center of X that is orthogonal to the bond. The σ -hole, located at the outermost area of X, is an electrophile because it can create attractive interactions with sites that are rich in electrons due to its lower electron density.

2.4.6.1 Directionality

The location and dimensions of the σ -hole, which is limited and narrow along the R—X covalent bond's length, determine the directionality of XB, this indicates a limited interaction region, causing the R—X···Y bond to be oriented at about 180° when the nucleophile Y comes into contact with the σ -hole. Stronger, shorter bonds are more directed than weaker, longer ones; the directionality also changes with bond strength. The bond angle, for instance, is roughly 170° in C—X···N systems if X is I and 155° in Cl. Ordered and homogeneous molecular layers are encouraged to form by this directionality.

2.4.6.2 Strength Tunability

The properties and qualities of the σ -hole determine the strength of XB interactions, which are contingent upon the XB donor. The order Cl < Br < I indicate that the strength generally grows in proportion to the X atom's polarizability and the electron-removal ability of the associated moiety. As can be seen, the molecule containing I exhibits the strongest positive electrostatic potential. Altering the hybridization of the C atom attached to the XB donor can likewise adjust the strength; the bond strength is arranged as follows: $[C(sp)-X] > [C(sp^2)-X]$





> [C(sp³)—X]. This versatility of XB comes from its ability to modify bond strength through changes to R's electron-withdrawing capacity. To enhance the capacity to pull electrons and produce, for example, aromatic rings, replacing H with F.

2.4.6.3 Hydrophobicity

Particularly in perfluorocarbon compounds, the presence of halogen atoms results in molecules that are both lipophilic and hydrophobic. The control of medication transport and absorption by lipophilicity makes this relevant for applications like drug design. The hydrophobic properties of XB-capable molecules enable the development of protective coatings on materials, keeping them safe from moisture and other deteriorating agents, according to this dissertation.

2.4.6.4 Donor Atom Dimension

Comparing halogen atoms to hydrogen, their Van der Waals radii are bigger (1.47 Å for F, 1.75 Å for Cl, 1.85 Å for Br, and 1.98 Å for I, against 1.20 Å for H). In order to encourage stable bonding, this characteristic can be used to make XB more susceptible to steric hindrance, which may have an impact on system stability.

These are extensively characterized and well-established features of XB. Halogens' behaviour and characteristics as electrophiles are explained by the σ-hole theory. It is debatable, nevertheless, exactly what XB is. Prior to investigations with strong XB donors demonstrating net electron density transfer, the interaction was thought to be caused by charge transfer events. Later, because of comparisons with HB, electrostatic attraction took center stage as the most likely explanation. Actually, there is probably more than one cause for XB. The XB complexes have a mixed electrostatic-dispersion energy, according to the decomposition of interaction energy utilizing techniques such as "symmetry-adapted perturbation theory (SAPT) and density functional theory (DFT)". The main component of XB interactions may vary based on the system, interacting partners, and environment, but overall, they probably involve multiple components.

2.4.7 Self-Assembled Monolayers

An important interface engineering method in several domains is the use of self-assembled monolayers, or SAMs. Using adsorption, self-assembled molecule assemblies (SAMs) arise on a substrate. Anchoring groups, linkers, and functional groups are usually their composition. A major benefit of SAMs for functionalization is that the anchoring group enables the molecules to engage with the surface and arrange themselves in an ordered form. Through





van der Waals interactions, the linker—typically an aliphatic chain—influences the supramolecular structure. One important factor in changing the surface properties is the functional group.

There are several techniques to deposit these layers, including:

- ➤ Liquid-phase deposition: Involves submerging substrates in a solution that contains the molecules that need to be deposited.
- > Spin coating: Using centrifugal force, a layer is deposited.
- **Vapor deposition:** The substrate is placed in a target molecule-saturated environment.

SAMs are primarily used on top of metal oxide layers in the field of perovskite solar cells (PSCs) because their flat surface makes it easier for an ordered layer to form. Even though there are certain difficulties due to the roughness of the perovskite surface, SAM synthesis on perovskite layers is still possible and advantageous for device performance. Perovskite surfaces with a variety of dangling bonds provide a platform that can accommodate SAMs with different functions. Sensitive methods like "transmission electron microscopy, scanning electron microscopy, and X-ray reflectometry are needed to characterize monolayers on perovskite, which is still a difficult task.

Remarkably, SAMs created by halogen bonding (XB) seem to functionalize the surface without "passivating" it in the traditional sense, meaning they don't change the perovskite's optoelectronic characteristics. The anchoring molecules are thought to be responsible for electrostatically screening the charge from the ions they interact with, which is why the passivation effect is observed when there is an interfacial dipole present, as with XB.

In general, the orderly distribution and stability of SAMs make them especially desirable. By attaching to surface imperfections, they can both positively impact crystal structure and morphology and decrease non-radiative recombination. Moreover, dipole moments that SAMs might create at the interface can impact the alignment of energy levels.

Dipolar molecules have a significant impact on the electronic properties of interfaces, offering a useful means to adjust Energy Level Alignment (ELA) and facilitate charge transfer within devices. A dramatic shift in the electrostatic potential across the interface caused by an interfacial dipole layer is depicted in Figure 3.6a, and this shift affects the vacuum level (E_{VAC}).





The material's energetics, including its work function (WF), ionization energy (IE), and electron affinity (EA), are altered by this change. More precisely, E_{VAC} shifts upward and increases WF when the dipole points towards the functionalized material's surface (from negative to positive charge). Conversely, if the dipole points outward, E_{VAC} shifts downwards, lowering the WF.⁴⁷

The magnitude of this shift is proportional to the dipole moment per unit area and can be described by:

$$\Delta E_{VAC} = -\frac{q_e \mu}{\varepsilon_0 \varepsilon_{eff} A}$$

Here, q_e represents the charge on an electron, μ is the dipole moment of the molecule, A denotes the area, ϵ_0 is the vacuum permittivity, and ϵ_{eff} is the effective dielectric constant accounting for depolarization effects.

Consequently, the interfacial Work Function (WF^I), in the presence of a dipolar layer and disregarding band bending, can be expressed as:

$$WF^{I} = WF_{sub} + \Delta E_{vac}$$

When considering interfacial dipoles resulting from surface functionalization with specific molecules, it's essential to account for different dipole components, including intrinsic molecular dipole and interaction-induced dipole. Together, these components make up the overall dipole; the interaction-induced dipole results from intricate charge exchange events, whereas the inherent dipole is usually known or calculable.

A crucial factor affecting the actual E_{VAC} shift brought about by dipolar layers is the arrangement and orientation of molecules. It is better to express the shift as follows: just the dipole component perpendicular to the surface influences it:

$$\mu = \mu_0 \cos\theta$$

Here, μ_0 is the intrinsic dipole moment and θ is the angle between the molecular axis and the surface normal. The significance of molecule orientation and packing density is thus highlighted by the fact that a strong intrinsic dipole does not always correspond to a large WF shift.⁴⁸





In practical applications, an ordered and dense molecular layer oriented perpendicularly to the surface maximizes the E_{VAC} shift. Such a configuration allows a larger portion of the dipole moment to contribute effectively. However, the effectiveness of a compact dipolar layer is constrained by depolarization effects arising from dipole-dipole interactions.^{49, 50}

Real-world scenarios deviate from ideal infinite layers due to defects and uneven layering, complicating the characterization of energy level shifts induced by dipoles. Techniques like Kelvin Probe Force Microscopy (KPFM) aid in directly probing these shifts, albeit challenges persist when assessing buried interfaces within devices.⁵¹

2.5 Optical Characterisation:

Optical characterization provides valuable insights into material properties such as quality, losses, and electronic behaviour, offering understanding of recombination mechanisms, dynamics, light absorption, and bandgap characteristics without causing damage to the samples. This dissertation employs two primary optical techniques: ultraviolet-visible (UV-Vis) spectroscopy and photoluminescence (PL) spectroscopy, which complement each other.

2.5.1: UV-Vis absorbance spectroscopy"

The recording of light absorption in the ultraviolet, visible, and occasionally near-infrared (UV-Vis-NIR) ranges is the process of UV-Vis spectroscopy. This technique measures how much incident light is absorbed, reflected, or transmitted using the Beer-Lambert law:

$$A = log_{10} \left(\frac{I}{I_0} \right)$$

where A is absorbance, I₀ is incident light intensity, and I is transmitted or reflected light intensity. Transmittance (T) and reflectance (R) are derived from I/I₀, with T usually expressed as a percentage. Given the polycrystalline nature of perovskite samples, which causes significant reflection and scattering, an integrating sphere is recommended to accurately account for all light interactions.

UV-Vis measurements also facilitate determination of the bandgap energy $E_{\rm g}$. Initially, an estimation can be made by identifying the wavelength corresponding to the absorption edge in transmission or the peak in reflection, using Planck's Law:



$$E = \frac{hc}{\lambda}$$

for photon energy E. However, a more precise determination of E_g involves Tauc plot method, which requires calculating the absorption coefficient α

$$\alpha = \frac{2.303 A}{d}$$

where d is the sample thickness. Alternatively, α can be determined from:

$$\alpha = \frac{A(h\nu - E_g)^n}{h\nu}$$

resulting in a Tauc plot where $(\alpha h v)^{1/n} = A^{1/n} h v - A^{1/n} E_g$

is plotted against $(\alpha hv)^{1/n}$ against hv. For direct bandgap semiconductors, n=1/2.

In this dissertation, UV-Vis spectroscopy, reflectance measurements utilized a Jasco 1050 UV-VIS spectrometer, while transmission measurements employed a Jasco 1050 UV-VIS spectrometer.

2.5.2 Fluorescence Spectroscopy:

Fluorescence spectroscopy involves the study of photoluminescence, where a material emits light after absorbing light. When this emission occurs rapidly, typically within nanoseconds, it is termed fluorescence. In contrast, if the emission persists and decays over longer periods, typically milliseconds, it is referred to as phosphorescence. Photoluminescence spectroscopy (PL) demonstrating the transition of electrons from the excited state (ES) to the ground state (GS), both radiative and non-radiative energy emissions occur within molecules. PL allows us to observe emission spectra across various wavelengths (nm). The emission spectrum is produced when molecules in the excited state return to the ground state by releasing photons that have less energy than those that they originally absorbed. In this dissertation, we have been used Jasco Fu-8500 Spectro fluorometer.

In fluorescence spectroscopy, photons interact with electrons within the molecules of a fluorophore. The molecule typically exists in a ground state with the lowest energy and an excited state with higher energy. Each electronic state includes various vibrational modes with slightly differing energies, represented by thinner energy levels.





Light, characterized as photons, carries energy described by hc/λ , where h is Planck's constant, c is the speed of light, and λ is the wavelength of light. Consequently, photon energy is inversely proportional to the wavelength of light.

The molecule can be stimulated to a higher energy level by absorption of photons that strike it with energy larger than the difference between the ground and excited states. The molecule swiftly reaches the lowest excited state level as a result of some energy being lost in molecular collisions. A photon with energy equal to the difference between the two states is released when the molecule relaxes back to its ground state from this state.

From this description, two critical aspects of fluorescence spectroscopy emerge:

- As a result of the emitted photons having less energy than the absorbed photons, light that is emitted has a wavelength that is always longer than light that is absorbed.
- Fluorescence occurs almost instantaneously because molecular relaxation due to collisions happens very rapidly.

2.5.3 Time-Resolved Photoluminescence (TRPL)

The lifespan of photoluminescence, or fluorescence, is an intrinsic characteristic of luminescent materials that provides important information about the dynamics of their excited states. For studying fast electronic deactivation processes that result in photon emission, or fluorescence, Time-Resolved Photoluminescence (TRPL) is the recommended technique. Molecules in their lowest excited singlet state typically have a lifespan of a few picoseconds to several nanoseconds. The chemical surroundings of the molecule can have an impact on this fluorescence lifespan. A Xe-flash lamp, LED, or pulsed laser are used to stimulate the sample in time-resolved investigations. Next, a sensitive detector with UV/Vis or NIR spectral area operating capability detects the emission that has been released. Sample spin coating was done while the measurements were made under ambient conditions. The lifespan of photoluminescence, or fluorescence, is an intrinsic characteristic of luminescent materials that provides important information about the dynamics of their excited states. For studying fast electronic deactivation processes that result in photon emission, or fluorescence, Time-Resolved Photoluminescence (TRPL) is the recommended technique. Molecules in their lowest excited singlet state typically have a lifespan of a few picoseconds to several nanoseconds. The chemical surroundings of the molecule can have an impact on this fluorescence lifespan. A Xe-flash lamp,





LED, or pulsed laser are used to stimulate the sample in time-resolved investigations. Next, a sensitive detector with UV/Vis or NIR spectral area operating capability detects the emission that has been released. Sample spin coating was done while the measurements were made under ambient conditions. "Samples were excited at 405 nm ps laser with a stable repetition rate of 20 MHz (FWHM: 176 ps).

2.6 Electrochemical Impedance Spectroscopy:

Impedance of electrochemistry in electroanalytical chemistry, spectroscopy (EIS) is a complicated subject. The opposition to current flow in an electrical circuit is commonly referred to as electrical resistance (R). According to Ohm's law, in direct current (DC) circumstances where the voltage or current across a resistor is constant, a higher resistance (R) indicates lower current flows at a given voltage.

Alternating current (AC) resistance that a circuit experiences overall is measured by impedance. A sinusoidal wave oscillates at a particular frequency in AC, in contrast to DC. Although Z is used in place of R in the impedance calculation, it still resembles Ohm's law. With ω representing the sine wave's angular frequency, Z is proportional to the frequency-dependent voltage $V(\omega)$ and current $I(\omega)$.

An electrochemical system receives a sinusoidal potential or current signal from a potentiostat in an EIS experiment. After that, the resulting signal—either current or potential—is recorded and examined. At each frequency, potential versus time and current vs time are among the data gathered. These time-domain data are transformed into potential and current magnitude vs. frequency charts using the Fast Fourier Transform (FFT).

A Nyquist plot is commonly used to display impedance data, with the real impedance (Zr) plotted on the x-axis and the negative imaginary impedance (-Zi) plotted on the y-axis. The labels "real" and "imaginary" originate from the way impedance is expressed mathematically. We may analyse series resistance, charge transfer resistance, and interlayer resistances by fitting the Nyquist plot data using Z-view software and converting to circuit diagrams. We conducted the trials for our solar devices at room temperature, with a voltage range of -0.5 V to 1 V and a frequency range of 2 MHz to 100 mHz utilizing the Biologic sp-300 equipment.

2.7 Electrical Characterisations: Carrier mobility and conductivity:





When an electron is exposed to an electric field, its velocity through a metal or semiconductor is measured by electron mobility in solid-state physics. The movement of holes under the same circumstances is referred to as hole mobility. Holes and electrons are both included in the concept of carrier mobility. The product of carrier concentration and mobility determines conductivity in a straight line. Either a large number of low-mobility electrons or a small number of highly mobile electrons can lead to a high conductivity, for example.

If there are many low-mobility electrons in a semiconductor or few high-mobility electrons in a semiconductor, it will have a major impact on the performance of transistors and other devices. For semiconductor materials, mobility is therefore an important factor. When other conditions stay the same, more mobility usually translates into improved gadget performance.

A number of variables, such as temperature, defect density, donor and acceptor concentrations, and electron and hole concentrations, can influence semiconductor mobility. In high fields when velocity saturation takes place, it is also affected by the electric field.

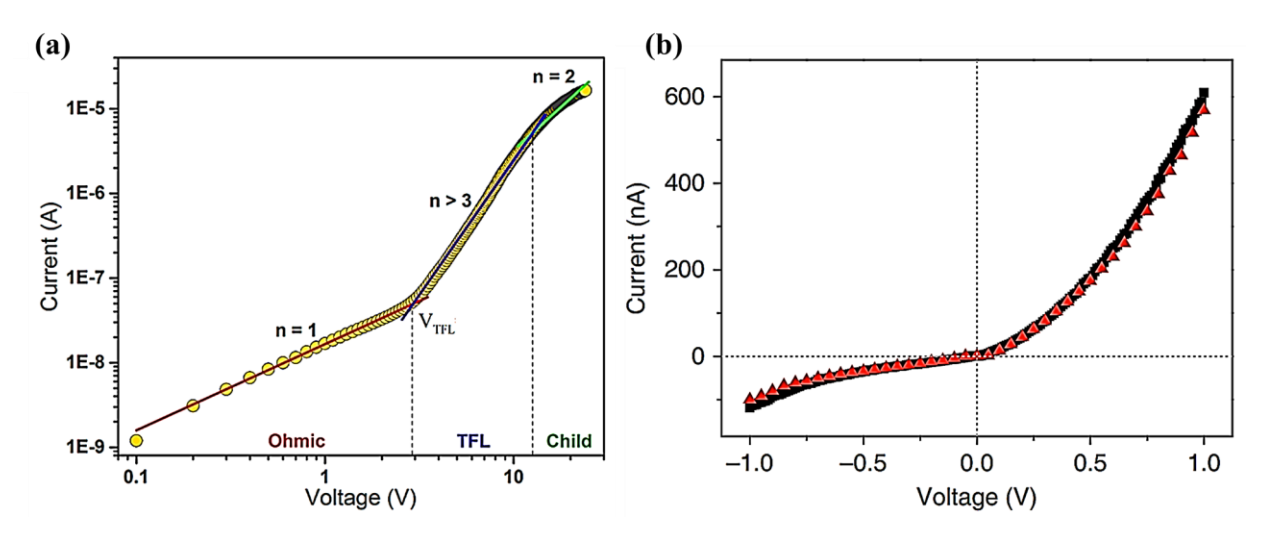


Figure 2.7. (a) semi log-log current and voltage curves for SCLC measurements. (b) Typical electrical Voltage Vs Current characterisation graph

We investigated the charge-transport properties of hole/electron only devices by using Keithly 2400 source meter to assess their suitability for optoelectronic applications. A capacitor-like device was created by sandwiching a perovskite layer between FTO/HTL or ETL and gold electrode, deposited by spin coating and thermal evaporation, to allow selective hole/electron injection. From low electric fields to high electric fields (0 V to 10 V), the evolution of space-charge-limited current (SCLC) under changing biases was examined (Figure 2.7 a).



At the trap-filled limit (TFL), where all trap states are occupied by charge carriers, the current demonstrated a large rise (I∞Vn with n>3), as indicated by the sharp increase in the SCLC, I–V characteristics of the perovskite material under different environmental conditions. The connection between VTFL and trap density (ntraps) is used.

$$n_{traps} = \frac{2\varepsilon\varepsilon_0 V_{TFL}}{eL^2}$$

where ε is the dielectric constant of perovskite (usually taken 32 for FAPbI₃), ε_0 is the vacuum permittivity, L is the thickness of the material, and e is the elementary charge, we can estimate the trap density.

At higher biases, the current followed a quadratic dependence ($I \propto V^2$). By fitting this with the Mott-Gurney law,

$$J_d = \frac{9\varepsilon\varepsilon_0\mu V^2}{8L^3}$$

where J_d is the current density and V is the applied voltage, we can calculate the carrier mobility (μ) . The uncertainties represent the standard deviation based on measurements from five similar devices.

We can estimate the conductivity, conductance by using simple ohms law, further, the free charge carrier density (n_c) can be estimated using the relation $n_c = \sigma/e\mu$.

2.8 Field Emission Scanning Electron Microscope (FESEM)

FE-SEM is a versatile technique used to evaluate the physical properties of materials, such as shape, texture, precipitation, phase transitions, and particle size distribution in three dimensions. It also allows for the examination of nanoparticle structures. FESEM captures images ranging from the micro to the nanoscale, with a resolution of less than 10 nm, which can be viewed from both top and cross-sectional perspectives.

To improve conductivity, samples are mounted on a metal stub for FESEM investigation using a sticky carbon disc. A conductive coating, usually gold (Au), is applied to the specimen to prevent charge build-up. In FESEM, electron guns (either thermionic or field emission guns) generate a fine, controlled electron beam. This beam passes through lenses and strikes the sample's surface at a low vacuum level. Above the objective lens are scan coils that regulate the





electron beam's position on the material. Signals arising from the interaction of the specimen with the electrons are monitored when the electron beam traverses the surface of the sample. These signals are detected by detectors, which then translate them into images that are shown on a computer screen. These images disclose the composition and surface morphology of the material.

Depending on the accelerating voltage and sample density, a few microns are how deep the high-energy electron beam enters the sample. Secondary electrons, backscattered electrons, and characteristic X-rays all produce signals.

In our study, we use a Carl Zeiss FESEM instrument, operating at 3 kV to record the FESEM images of thin films.

2.9 Samples and Device Preparation

Solution-based methods were used to create the films for sample characterization and device preparation. The devices' metal contacts (Au), which were applied after being thermally evaporated onto the substrates, were the lone exception.

The devices' general design is based on the n-i-p architecture that was covered in the part before this one. TiO2 specifically functioned as the "electron transport layer (ETL)". First, spin coating was used to create a compact layer of TiO2 on "fluorine-doped tin oxide (FTO)". This was followed by spin coating and annealing of a mesoporous layer. Doped 2,2',7,7'-Tetrakis[N,N-di(4-methoxyphenyl)amino]The hole transport layer (HTL) of -9,9'-spirobifluorene (spiro-OMeTAD) was spin-coated on top of the perovskite layer. The top contact was evaporating gold (Au).

Direct deposition of the layers of interest, including perovskite films, on glass substrates allowed for optical characterisation using UV-Vis and PL spectroscopy. Films were either deposited on fluorine tin oxide (FTO) or fabricated as entire devices up to the necessary layer because energetic characterization required conductive substrates.

Everything, except the ETL deposition, was done in gloveboxes filled with nitrogen. Depending on their composition, the perovskite films were annealed for either 30 minutes or 1 hour after being created using the conventional one-step spin-coating method with anti-solvent treatment. Cs_{0.05}(FA_{0.85}MA_{0.15})_{0.95}Pb(I_{0.85}Br_{0.15})₃ was the "triple cation" formula employed as the





main perovskite composition in this dissertation. To achieve the desired composition, various spin-coating algorithms and anti-solvent drop timings were needed.

Molecular assemblies were also used to functionalize the perovskite surface. Layers between the perovskite and the next layer were covered in monolayers of these molecules. The ensuing working chapters will provide further information on the specific deposition methods needed to create such monolayers.

2.10 Materials, Reagents and Solvents:

Lead bromide (PbBr₂), Lead iodide (PbI₂), Caesium iodide (CsI), Methyl ammonium iodide (MAI), Formamadinium iodide (FAI), Spiro-OMeTAD, TBP, LiTFSI, FK209, and Zn dust are purchased from Great cell, Sigma Aldrich, TCI and Avra laboratories. Dimethyl formamide (DMF), Dimethyl Sulfoxide (DMSO), Dichloromethane (DCM), hexane, methanol, ethanol, toluene, acetone, isopropanol, dilute hydrochloric acid is purchased from sigma, TCI and Avra laboratories of India.



Chapter 3

Unlocking Solar Cell Potential: EDTA as a Self-Assembling Chelating Molecule for Enhanced Electron Transport in Perovskite Solar Cells



Abstract

It is known that EDTA can form complexes with transition metal oxides by donating its lone-pair electrons to the vacant d-orbital of the transition metal atom. We hypothesized that EDTA-modified TiO₂ would serve as a more effective electron transport layer (ETL) in PSCs than TiO2 alone. To test this, we designed and fabricated an EDTA-TiO2 based device with the structure FTO/c-TiO₂/m-TiO₂/EDTA/Perovskite/HTM/Au. Triple cation perovskite was used as the active absorber due to its appropriate band gap and enhanced phase stability through Cs doping. The J-V curves of planar-type PSCs using EDTA-TiO₂ and TiO₂-based ETLs were analysed, with key parameters such as short-circuit current density (Jsc), open-circuit voltage (Voc), fill factor (FF), and PCE summarized in Table 1 (Figure (a), inset). The device with EDTA-TiO2 achieved a PCE of 19.77%, with Jsc = 25.07 mA/cm², Voc = 1.04 V, and FF = 75.50. In comparison, the device with TiO_2 (reference) showed a PCE of 17.58%, with Jsc =23.03 mA/cm², Voc = 1.05 V, and FF = 73.05. The superior performance of the EDTA-TiO₂ ETL is attributed to higher electron mobility, which enhances electron extraction, and a larger Voc due to the closer energy level alignment between EDTA-TiO₂ and the perovskite. Stability tests showed that the EDTA-TiO₂ based device retained 99% of its efficiency over 60 days, whereas the reference device with TiO₂ experienced a drop of more than 3% of its PCE. Additionally, the TiO₂-based PSCs exhibited negligible hysteresis due to the elimination of charge accumulation at the perovskite/ETL interface and improved electron extraction. Furthermore, EDTA treatment rendered the TiO₂ surface more hydrophilic, reducing the Gibbs free energy for heterogeneous nucleation and resulting in higher quality perovskite films.





3.1. Introduction

In recent years, Perovskite photovoltaics, with power conversion efficiencies (PCE) above 26%, have quickly progressed because of their superior photoelectric qualities. Perovskite solar cells are now considered to be excellent contenders for the upcoming generation of photovoltaic technology due to these developments. Lead, however, poses serious concerns to the environment and public health when it comes to both manufacturing and usage of water-soluble perovskites. Lead-free large-scale industrial adoption, the issue of lead toxicity must be addressed. Lead-free alternatives, such as those based on tin (Sn), silver bismuth (AgBi), and titanium (Ti), are being explored for eco-friendly commercialization, though their overall performance remains inadequate. Consequently, strategies to mitigate lead leakage are essential.

By focusing on leakage rates and improving the stability of perovskite solar cells (PSCs), lead-capturing approaches including polymer resin protective layers and self-healing encapsulation have shown efficacy in minimizing lead leakage. Nonetheless, these methods cannot entirely prevent lead leakage when device encapsulation is compromised by external factors like hail, sandstorms, or continuous rainfall.⁵⁹ Such damage can lead to lead ions contaminating soil and water, ultimately entering the human body through food and drinking water, posing severe health risks.⁶⁰ Research indicates that lead ions can cause blood protein poisoning, cell death, organ failure, and weight loss in organisms.⁶¹ Current mainstream strategies have not sufficiently mitigated lead toxicity.⁶² Therefore, an effective approach to isolate and detoxify lead ions is critical.

To attain a high device efficiency, an efficient ETL needs to fulfil multiple requirements: high electron mobility to effectively remove carriers from the active layer, minimize charge recombination, and lessen hysteresis; matched energy levels with the perovskite to attain the intended open-circuit voltage (*Voc*); and good optical transmittance to guarantee that enough light reaches the perovskite absorber.⁶³ Because of the comparatively poor electron mobility of the ETL, planar-type PSCs still lag behind mesoporous-type devices. This is probably because charge accumulation occurs at the ETL/perovskite interface.⁶⁴ Better PSC performance is anticipated when ETL electron mobility increases. Since EDTA has a potent chelating action, it has been useful in altering ETLs in Perovskite solar cells.⁶⁵⁻⁶⁸

We propose an EDTA complex formation with both ETL and perovskite, its known that EDTA can form complexes with transition metal oxides by donating its lone-pair electrons to the





vacant d-orbital of the transition metal atom. 53, 69, 70 We hypothesized that EDTA-modified TiO₂ would serve as a more effective electron transport layer (ETL) in PSCs than TiO2 alone. To test this, we designed and fabricated an EDTA-TiO2 based device with the structure FTO/c-TiO2/m-TiO₂/EDTA/Perovskite/HTM/Au. The J-V curves of planar-type PSCs using EDTA-TiO₂ and TiO₂-based ETLs were analysed, with key parameters such as short-circuit current density (*Isc*), open-circuit voltage (Voc), fill factor (FF), and PCE summarized in Table 1 (Figure (a), inset). The device with EDTA-TiO2 achieved a PCE of 19.77%, with $Jsc = 25.07 \text{ mA/cm}^2$, Voc = 1.04V, and FF = 75.50. In comparison, the device with TiO_2 (reference) showed a PCE of 17.58%, with $Jsc = 23.03 \text{ mA/cm}^2$, Voc = 1.05 V, and FF = 73.05. The superior performance of the EDTA-TiO₂ ETL is attributed to higher electron mobility, which enhances electron extraction, and a larger Voc due to the closer energy level alignment between EDTA-TiO₂ and the perovskite. Continuous illumination studies over 20 minutes demonstrated consistent PCE and current densities. Stability tests showed that the EDTA-TiO₂ based device retained 99% of its efficiency over 60 days, whereas the reference device with TiO₂ experienced a drop of more than 3% of its PCE. Further studies on electron-only device carrier parameters using conductivity and "spacecharge-limited current (SCLC) measurements" at different temperatures confirmed the robustness of the EDTA-TiO₂ ETL even at higher temperatures. In this work, we have successfully developed EDTA-complexed TiO₂ ETLs for planar-type PSCs, achieving a PCE as high as 19.77%. Furthermore, the TiO₂-based PSCs showed very less hysteresis because of enhanced electron extraction and the removal of charge accumulation at the perovskite/ETL interface. Moreover, EDTA treatment increased the hydrophilicity of the TiO₂ surface, lowering the Gibbs free energy required for heterogeneous nucleation and producing perovskite films of superior quality.

3.2. Experimental Section

The source of all the materials and the various characterization techniques used in this chapter are described in Chapter 2.

3.2.1. Fabrication of Perovskite solar cells:

Perovskite solar cell (PSC) devices were constructed with the architecture FTO/c-TiO₂/m-TiO₂/EDTA/Cs_{0.05}(FA_{0.85}MA_{0.15})_{0.95}Pb(I_{0.85}Br_{0.15})₃/HTM/Au. The fluorine-doped tin oxide (FTO) substrates (7 Ω /sq) were purchased from Great Cell Solar. These substrates were etched according to the mask design using 2M HCl and Zn powder, followed by sequential





cleaning in an ultrasonic bath with Hellmanex (from Sigma-Aldrich) for 30 minutes. They were then rinsed with deionized water, acetone, and isopropanol, and finally treated with oxygen plasma for 20 minutes. A compact layer of titanium dioxide (c-TiO₂) approximately 30 nm thick was deposited on the FTO by spin coating at 6000 rpm for 30 seconds, using a precursor solution of 0.1 mL titanium diisopropoxide bis(acetylacetonate) in 1 mL ethanol. The substrates were then heated on a hotplate at 150 °C for 10 minutes, followed by 450 °C for 30 minutes, and then allowed to cool to room temperature. A mesoporous TiO₂ (m-TiO₂) layer was applied over the compact layer by spin coating at 4000 rpm for 20 seconds using Titania paste (MPT-20, Great Cell Solar) diluted in ethanol to achieve a layer thickness of about 150 nm. The coated substrates were dried at 125 °C for 10 minutes, sintered at 500 °C for 30 minutes in a muffle furnace, and then cooled to room temperature. These mesoporous-coated substrates were sonicated in ethanol for 15 minutes, treated with a 0.1M TiCl₄ solution at 70 °C, annealed at 450 °C for 30 minutes in a muffle furnace, and then cooled to room temperature. Ethylenediaminetetraacetic acid (EDTA) layers was spin-coated at 5000 rpm for 60 s using the precursor solution made in IPA with super saturated, and filtered with 0.22-micron size PTFE syringe filter, and then dried at 100 °C for 10 min to remove the residual solvent. The perovskite films were deposited on the EDTA layer using a precursor solution consisting of NH₂CHNH₂I (1 M), PbI₂ (1.1 M), CH₃NH₃Br (0.2 M), PbBr₂ (0.2 M), and CsI (0.075 M) in anhydrous DMF and DMSO (4:1 v/v). The perovskite solution was spin-coated in two steps at 1000 and 6000 rpm for 10 and 30 seconds, respectively. During the second step, 100 µL of chlorobenzene was dropped during the spinning substrate 15 seconds before the end of the program. The substrates were then annealed at 100 °C for 1 hour in a glove box, and subsequently cooled.

A hole transport material (HTM) solution (60 mM in chlorobenzene), doped with bis(trifluoromethylsulfonyl)imide lithium salt (Li-TFSI, Aldrich), tris(2-(1H-pyrazol-1-yl)-4-tert-butylpyridine)cobalt(III)tris(bis(trifluoromethylsulfonyl)imide) (FK209), and 4-tert-butylpyridine (TBP, Aldrich), was then spin-coated onto the perovskite layer at 3000 rpm for 20 seconds. The molar ratios of Li-TFSI, FK209, and TBP in the HTM were 0.5, 0.03, and 3.3, respectively. Finally, an 80 nm layer of gold was thermally evaporated under high vacuum onto the device. The fabricated device with EDTA addition on top of m-TiO₂ layer, taken as EDTA device and without addition of EDTA taken as Ref device. The complete fabrication procedure schematically represented in Figure 1.



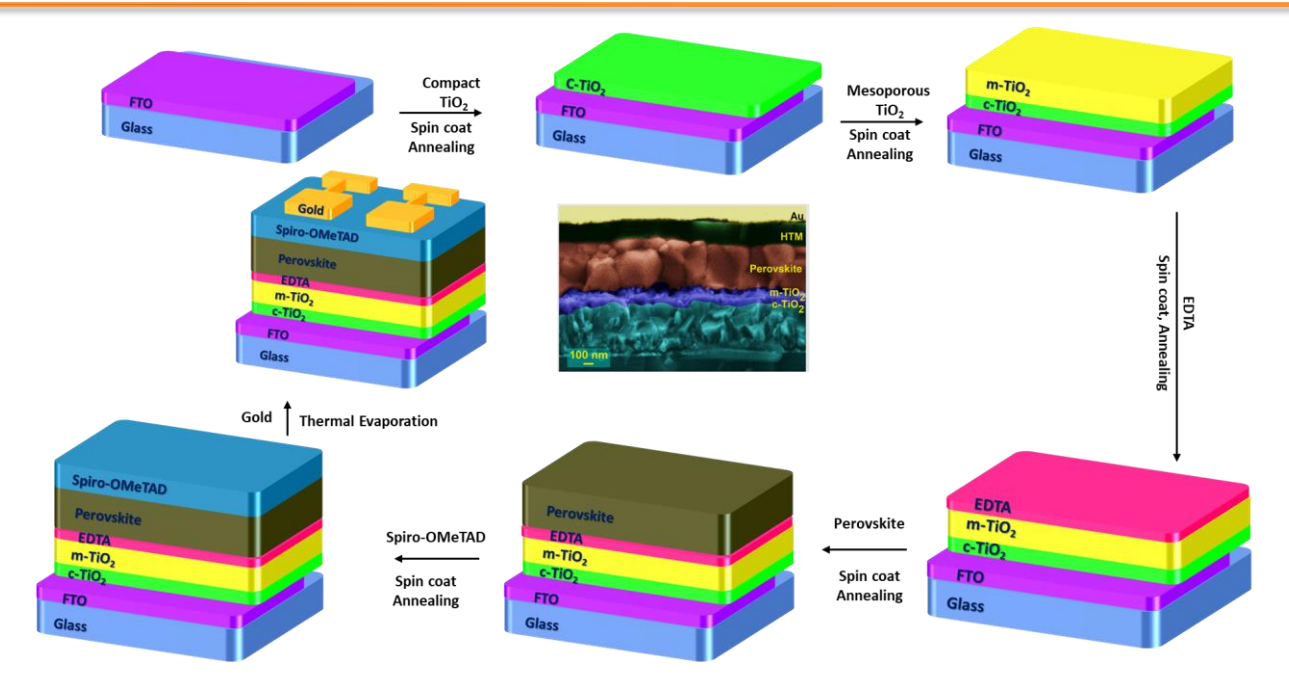


Figure. 3.1. Schematic route of fabrication of perovskite solar cell with the addition of EDTA.

3.2.2. Electron mobility of Perovskite layer with and without EDTA films:

To understand charge transport, we measured electron mobility using different electron transport layers (ETLs) within the same device structure. An electron-only device was designed with an FTO/TiO₂/PVK/Au configuration named as Ref and FTO/TiO₂/EDTA/PVK/Au named as EDTA. In this setup, we assumed the current is solely influenced by electrons. Neglecting diffusion and electric field effects, the current density was determined using the space-chargelimited current (SCLC) model. A 30-nm thick layer of compact TiO₂ coated onto FTO substrates, followed by spin-coating of m-TiO₂ on the FTO/c-TiO₂ layer, EDTA and Perovskite (PVK). Finally, another 80-nm thick Au layer was deposited on the FTO/TiO₂/EDTA/PVK and FTO/TiO₂/PVK samples. Dark current-voltage (J-V) measurements were performed using a Keithley 2400 source under ambient conditions. The electron mobility (µe) was extracted by fitting the J–V curves according to the Mott–Gurney law.⁷¹

The SCLC, I-V characteristics of the perovskite material under various environments, exhibited a sharp increase at V_{TFL} , where the current showed a significant rise (I \propto Vⁿ with n>3), indicating the transition to the trap-filled limit (TFL), where all trap states are occupied by charge carriers. Using the relationship between V_{TFL} and trap density (n_{traps}),

$$n_{traps} = \frac{2\varepsilon\varepsilon_0 V_{TFL}}{eL^2}$$





where ε is the dielectric constant of perovskite (usually taken 32 for FAPbI₃), ε_0 is the vacuum permittivity, L is the thickness of the material, and e is the elementary charge, we can estimate the trap density.

At higher biases, the current followed a quadratic dependence ($I \propto V^2$). By fitting this with the Mott-Gurney law,

$$J_d = \frac{9\varepsilon\varepsilon_0\mu V^2}{8L^3}$$

where J_d is the current density and V is the applied voltage, we can calculate the carrier mobility (μ) . The uncertainties represent the standard deviation based on measurements from five similar devices.

We can estimate the conductivity, conductance by using simple ohms law, further, the free charge carrier density (n_c) can be estimated using the relation $n_c=\sigma/e\mu$.

3.3. Results and Discussions

3.3.1. Characterization of EDTA films and perovskite films:

EDTA is well-known for its capacity to react with transition metal oxides to generate complexes by filling the d-orbitals of transition metal atoms with its lone-pair electrons. As a result, EDTA was chosen to alter TiO₂ and improve its functionality. Figure 3.2a presents the XRD crystal data of multi-crystalline perovskite thin films coated on glass substrates. The samples include perovskite directly coated on glass, on a TiO₂ layer, and with the addition of EDTA to the TiO₂ layers from bottom to top respectively. All samples exhibit characteristic perovskite diffraction peaks at approximately "14.2, 20.1, 24.7, 28.6, 32, 35.2, 40.8, 43.4, 50.5, and 52.7, corresponding to the (110), (012), (003), (220), (123), (114), (024), (015), (006), and (135) lattice planes, respectively." We can observe that incorporating EDTA can enhancing the crystallinity then the perovskite film on TiO₂ layer and reduce the trap density in the perovskite structure. The triple cation perovskite phase's purity was confirmed when no reflections other than those of the cubic phase were found in the ground crystal's powder XRD spectrum. Additionally, powder XRD analysis of TiO₂ thin films and TiO₂ with EDTA added revealed an amorphous structure.





Figure 3.2b shows the ultraviolet (UV-vis) absorption spectra for the pristine perovskite, perovskite coated on a TiO₂ layer, perovskite with EDTA and TiO₂, bare TiO₂, and TiO₂ with EDTA. The photo response of the perovskite structure is clearly enhanced by the addition of TiO₂ and EDTA. Owing probably to the compact and flawless triple cation perovskite layer, the EDTA-containing film showed the maximum absorption level, which ranged from 800 to 300 nm. In addition, as Figure 2c illustrates, the direct band gap energy of each sample was calculated from the absorption spectra via a Tauc plot. Roughly 1.6 eV is the calculated band gap value. The EDTA+TiO₂ film band gap is lower than that of the TiO₂ film, which aligns with the binding of EDTA to the TiO₂ layer.

The properties of photo-generated charge carrier transport were assessed using photoluminescence (PL) spectroscopy. In agreement with the perovskite absorption spectra, all samples showed a PL peak at around 765 nm, as shown in Figure 2d. Particularly, thin films combining TiO₂+PVK and TiO₂+EDTA+PVK showed a notable PL quenching effect, suggesting effective charge extraction and non-radiative recombination suppression. Significant gains in photovoltaic performance are linked to development. The perovskite coated on different ETLs' time-resolved this photoluminescence (TRPL) is shown in Figure 2e. Supplementary Table 1 provides details on the lives and related amplitudes. The slow decay component (71) is usually attributed to radiative recombination of free charge carriers because of bulk traps, whereas the quick decay component $(\tau 2)$ is a result of charge carrier quenching at the interface. The longest lifespans are seen in perovskite films coated on TiO₂ and TiO₂+EDTA. The lifetime of the glass/perovskite sample, on the other hand, has significantly decreased to less than half. The PL decay is dominated by $\tau 1$, suggesting extensive recombination prior to charge extraction, and the fast and slow decay lifetimes for the TiO₂/perovskite and EDTA/perovskite samples are extremely similar. Both $\tau 1$ and $\tau 2$ are shortened to 14.16 ns and 0.97 ns, respectively, when perovskite is deposited on TiO₂+EDTA. Furthermore, τ_2 seems to be the dominant factor in the photoluminescence decline, suggesting that electrons are efficiently transferred from the perovskite layer to the TiO2+EDTA with little loss through recombination.

Chapter-3

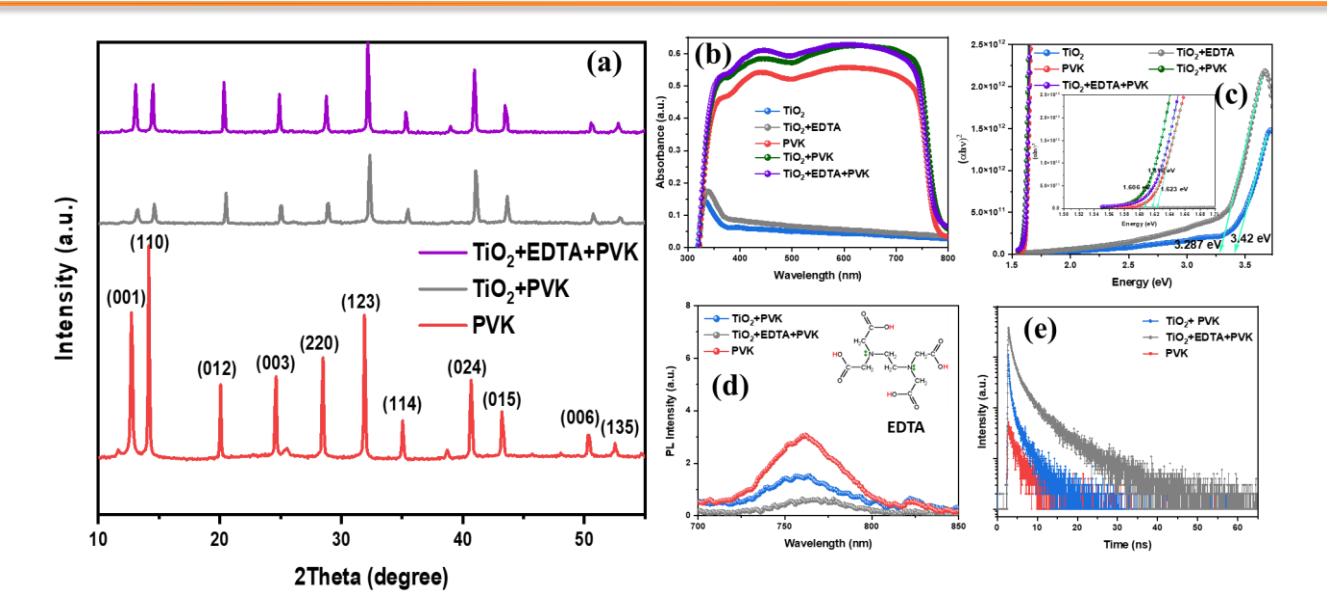


Figure. 3.2. (a) XRD spectra of perovskite (PVK), perovskite on TiO₂ and TiO₂ +EDTA films. (b,c) absorbance spectra and tau plot of perovskite (PVK), perovskite on TiO₂ and TiO₂ +EDTA films, and TiO₂ and TiO₂ +EDTA films. (d,e) Emission spectra and TRPL of perovskite (PVK), perovskite on TiO₂ and TiO₂ +EDTA films.

3.3.2. Photovoltaic Properties

TiO₂+EDTA is anticipated to outperform TiO₂ alone as an ETL in PSCs due to its enhanced optoelectronic capabilities that were previously described. Thus, with the device structure FTO/c-TiO₂/m-TiO₂/EDTA/Cs_{0.05}(FA_{0.85}MA_{0.15})_{0.95}Pb(I_{0.85}Br_{0.15})₃/HTM/Au, planar-type PSCs were designed and produced utilizing a variety of ETLs. With a little amount of Cs doping to improve phase stability, a triple cation perovskite was used as the active absorber due to its appropriate band gap. For the sake of illustration, cross-sectional SEM images of the entire device structures of the architecture with and without EDTA are shown in Supplementary Figure 3.3(e, f). EDTA-treated devices are designated as Ref devices, while EDTA-free devices are designated as EDTA-treated devices, with the perovskite film thickness being maintained at about 400 nm. Figure 3.3 (a, b) depicts the EDTA addition together with the shape of the TiO₂ layer. When using TiO₂ as the substrate, the perovskite grains are not big enough to penetrate the film thickness; however, when the grains are deposited on EDTA on TiO₂, they expand over the film thickness and are considerably larger, which is consistent with the top-view SEM results displayed in Figure 3.3(c, d).



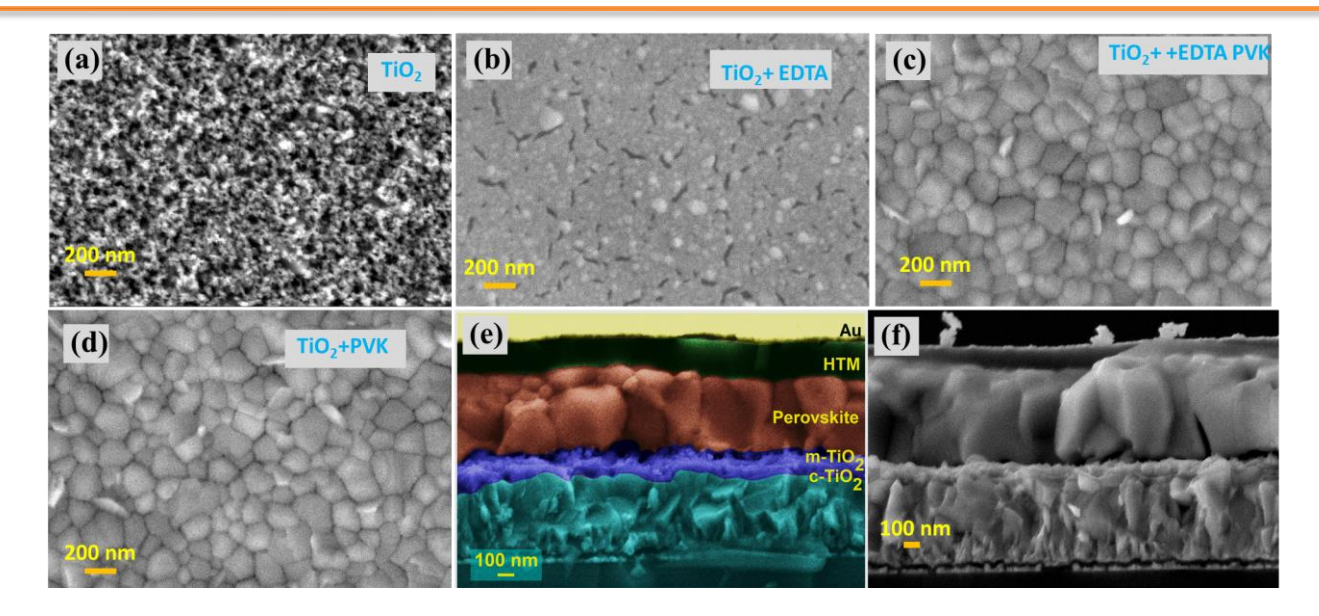


Figure. 3.3. (a, b) Top-view of TiO₂ and TiO₂+EDTA film. (c, d) Top-view of perovskite film on TiO₂+EDTA and TiO₂ film respectively. (e, f) Cross-section FESEM of PSC with TiO₂ and TiO₂+EDTA layers.

Key characteristics including short-circuit current density (Jsc), Voc, fill factor (FF), and PCE" are presented in Table 3.1. Figure 3.4a shows the J–V curves of planar-type PSCs employing various ETLs. With Jsc = 25.07 mA/cm², Voc = 1.04 V, and FF = 75.50, the EDTA-using device achieves a PCE of 19.77%. With Jsc = 23.03 mA/cm², Voc = 1.05 V, and FF = 73.05." In contrast, the TiO₂-containing device (reference) displayed a PCE of 17.58%. It is noteworthy that using EDTA+TiO₂ as the ETL increases Jsc, FF, and Voc to 25.07 mAcm⁻² and 0.75, respectively, and can result in a PCE of up to 19.77%. Since there is less electron mobility and more resistance, the device without an EDTA base performance reduced, as evidenced by lower Jsc and FF. As a result of greater electron mobility, which facilitates effective electron extraction, and a bigger Voc because EDTA+TiO₂ and perovskite have a tighter energy level alignment, planar-type PSCs with EDTA+TiO₂ ETL, on the other hand, perform better as shown by higher Jsc and FF.

Measurement	Voc (V)	Jsc (mA/cm²)	Fill Factor	Efficiency	R (ohms)
Ref	1.05	23.03	73.05	17.58	58.05
EDTA	1.04	25.07	75.50	19.77	38.60

Table 3.1: Photovoltaic J-V data for the EDTA and Ref devices.



Moreover, PSCs were evaluated under constant 100 mW cm⁻² irradiation. PCE changes are displayed in Figure 3.4b, and Supplementary Table S1 has precise J-V values. The TiO₂based device only keeps 78% of its initial efficiency after 1220 seconds of illumination, while the EDTA-TiO2-based device keeps 99% of its efficiency thereafter. This suggests that under both continuous and dark irradiation settings, the EDTA-TiO2 device has higher stability. Perovskite film deterioration and spiro-OMeTAD HTL instability are the primary causes of PSC instability. Since the spiro-OMeTAD HTL was the same for all devices, there should be consistency in the degradation from the HTL between them. When deposited on EDTA-TiO₂ instead of pristine TiO₂, the perovskite film's grain size increases threefold, which enhances the environmental stability of the EDTA-TiO₂-based PSCs by reducing moisture permeation at the grain boundaries. After then, each of the 30 unique devices for each ETL was manufactured and measured in order to examine repeatability, as shown in Figure 3.4 (e, f). Compiling data from Supplementary Table S2, Figure 3.4f displays the PCE distribution for devices with various ETLs. As opposed to devices based on EDTA and TiO₂, the EDTA+TiO₂ devices display remarkable repeatability with a very tiny standard deviation, suggesting that EDTA+TiO₂ is a great ETL for planar-type PSCs.

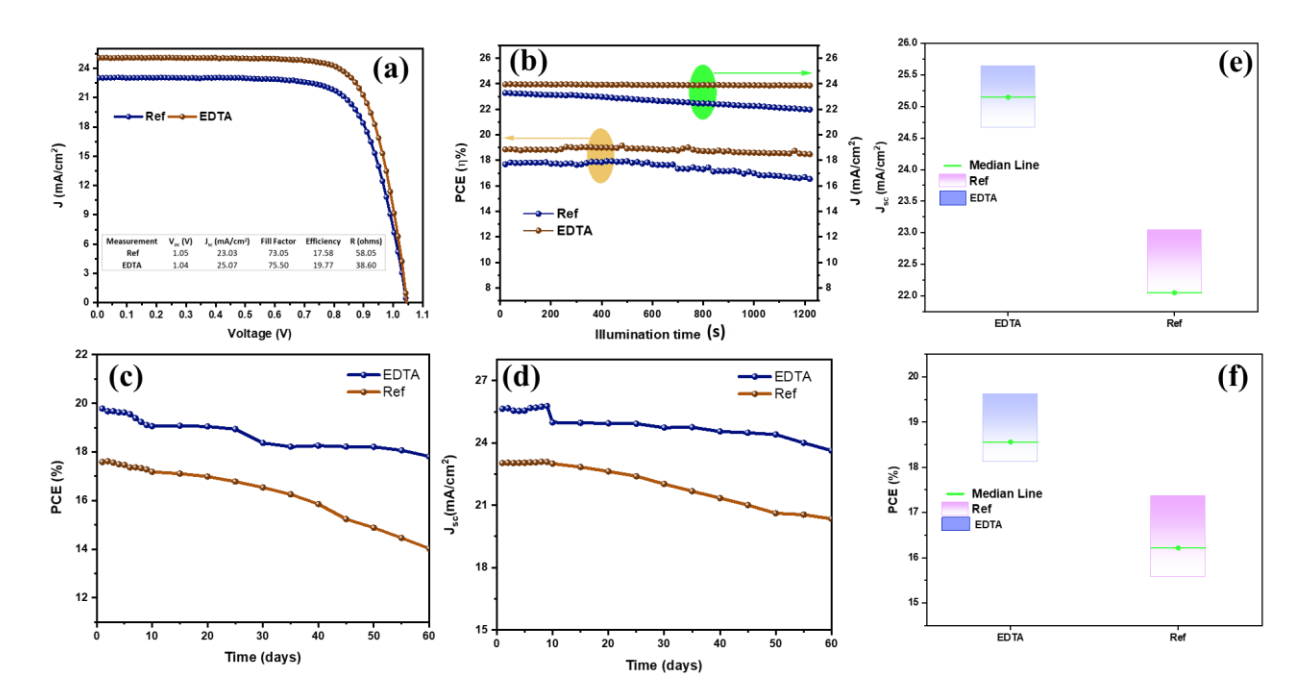


Figure. 3.4. (a) J-V characteristics parameters of EDTA and Ref devices, inset(table for all the photovoltaic parameters of EDTA and Ref devices), (b) Continuous irradiation of EDTA and Ref devices under 1 sun, (c,d) Stability data of EDTA and Ref devices with PCE and current densities respectively, (e, f) Reproducibility statistics of EDTA and Ref devices.





3.3.3 Stability and Carrier parameters:

The most important component for PSCs is stability. The PCE as a function of storage duration is shown in Figure 3.4(c, d), and Supplementary Table S3 contains specific J–V values. After storing in the dark for 60 days in ambient settings, the EDTA-TiO2 device maintains 92% of its initial efficiency, but the TiO2-based device only keeps 74%.

ITO/ETL/EDTA/perovskite/Au-only electron-only devices were created to measure the trap density in perovskite films that were produced on various substrates. For these devices, the dark current-voltage (I-V) curves are displayed in Figure 3.5 (a,b). Ohmic response is seen in the linear relationship at low bias voltages. The current increases nonlinearly, indicating that the traps are fully occupied, when the bias voltage beyond the kink point, which is known as the trap-filled limit voltage (VTFL). Chapter 2 has an equation that can be used to compute the trap density (N_t) $3.39 \times 10^{15} \text{ cm}^{-3}$ is the trap density for perovskite films on EDTA-TiO₂substrates. For layers TiO_2 over, the trap density remarkably increases to 7.36×10^{15} cm⁻³. The reduced density of the perovskite film's grain boundaries is responsible for this notable decrease in trap density. The main cause of the decreased hysteresis is also the fact that the trap density of the perovskite layer is greatly decreased when it is placed on EDTA-TiO2. Furthermore, the TiO2 ETL's electron mobility is only 1.42×10^{-5} cm² V⁻¹ s⁻¹, which is around 10 times slower than the doped spiro-OMeTAD's hole mobility (roughly 10^{-4} cm² V⁻¹ s⁻¹) HTL. Hysteresis is produced at the TiO₂/perovskite interface due to charge accumulation brought on by the decreased electron flow (F_e) as a result of this discrepancy in comparison to the hole flux (F_h). When EDTA-TiO₂ (1.42 $\times 10^{-5}$ cm² V⁻¹ s⁻¹), which has a high electron mobility, is utilized as the ETL. Thus, there is very little charge accumulation and hysteresis because EDTA-high TiO₂'s mobility promotes electron transfer from perovskite to EDTA-TiO₂ ETL.





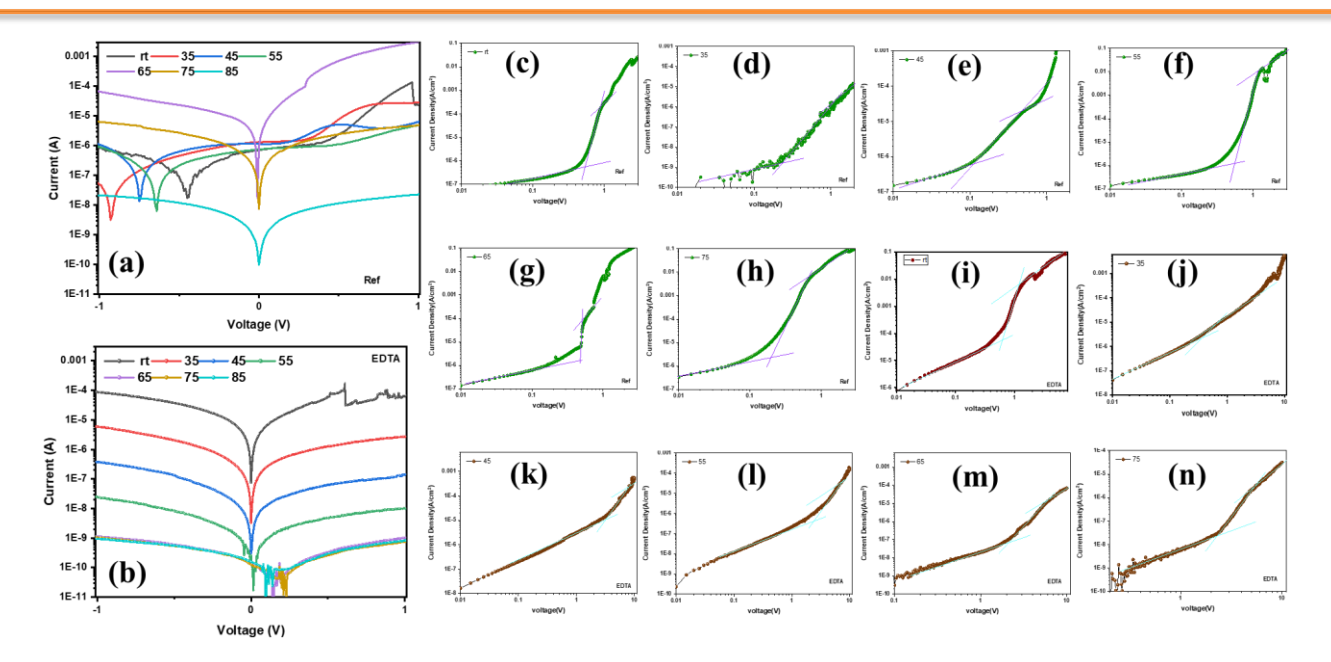


Figure. 3.5. (a,b) Semi log I-V curves of the EDTA and Ref devices with electron only device, (c-h) semi log J-V curves of the Ref devices with electron only device, at rt to 75^oC, (i-n) semi log J-V curves of the EDTA devices with electron only device, at rt to 75^oC.

3.4. Conclusions

The PCE of planar-type PSCs was increased to 19.77% with minimal hysteresis through the development of an extremely efficient EDTA-TiO₂ ETL. These planar-type PSCs exhibit exceptional performance because of the superior (bigger grain size, reduced trap density, and excellent crystallinity) perovskite films produced atop EDTA-TiO₂ ETLs. Because of the improved electron transport and less charge accumulation at the interface caused by the increased electron mobility, there is less J-V hysteresis and high efficiency. The longer grain size also increases stability over time by reducing perovskite breakdown at grain borders. Perovskite photovoltaics is predicted to advance with the help of this work, which demonstrates a promising method for creating high-quality ETLs.



Chapter 4

Leveraging Guanidinium Thiocyanate Self-Assembly to Enhance Perovskite Solar Cell Efficiency



Abstract

Employing self-assembled monolayers (SAMs) is a notable technique for interface engineering across various fields. SAMs are molecular assemblies that spontaneously form on a substrate through adsorption and typically consist of an anchoring group, a linker, and a functional group. The anchoring group enables the molecules to interact with the surface and arrange themselves in an orderly fashion, which is crucial for functionalization. The linker, often an aliphatic chain, influences the supramolecular structure via Van der Waals interactions, while the functional group plays a key role in modifying the surface properties. Employing SAMs on the perovskite film is proven to be an effective method to ameliorate the PCE and long-term stability of perovskite solar cells (PSCs). In this work, the perovskite films, Cs_{0.05}(FA_{0.85}MA_{0.15})_{0.95}Pb(I_{0.85}Br_{0.15})₃, were modified with guanidinium thiocyanate (GuSCN) as a SAM. Additionally, defect density is reduced, and the charge recombination process is effectively suppressed, leading to improved PCE and stability. With the addition of 1% GuSCN to the perovskite film, the device achieved a champion PCE of 19.95%, an Voc of 1.09 V, a Jsc of 24.69 mA/cm², and a FF of 74%. This represents a 3% improvement over the counterpart without GuSCN. The enhanced Cs_{0.05}(FA_{0.85}MA_{0.15})_{0.95}Pb(I_{0.85}Br_{0.15})₃ PSC also demonstrated better stability, retaining approximately 95% of its initial PCE after being stored for over 60 days without encapsulation in a desiccator, compared to only 64% for pristine PSCs. This work provides a simple strategy for reducing defects and improving the performance of PSCs.





4.1. Introduction

Organic-inorganic metal halide perovskite solar cells (PSCs) have demonstrated tremendous commercial potential over the last ten years, as seen by their amazing gains in photoelectric efficiency, which have increased from 3.8% to 26.1%.⁷² Planar inverted PSCs offer several advantages over their traditional counterparts, including negligible hysteresis, easier fabrication processes, and broader applicability in perovskite-based tandem solar cells.⁷³ However, issues such as interface defects and suboptimal charge transfer between the perovskite layer and the charge transport layer (CTL) significantly impact the photovoltaic performance of these devices.

Interface engineering is another effective strategy to enhance charge collection and improve perovskite quality. Various passivation molecules have been developed to eliminate charged defects, often incorporating specific functional groups to modulate defect passivation and improve carrier extraction and collection. Significant open-circuit voltage (Voc) and fill factor (FF) losses result from nonradiative recombination at grain boundaries and interfacial contacts, impeding the growth of PSCs. Grain boundaries and perovskite film surfaces are the main locations of defects. 74-76 By stimulating grain regrowth, growing grain size, and passivating flaws, interfacial modification is a straightforward yet efficient method to treat this problem. Several large organic ligands are utilized as precursor solution additives or surface passivants to improve device performance. These include guanidinium, ⁷⁷ phenylethylammonium (PEAX), ⁷⁸ and phenylethylammonium derivatives.⁷⁹ These compounds efficiently inhibit nonradiative recombination by forming two-dimensional perovskites or filling cationic vacancy defects.^{80,81} Though there are still disagreements regarding their inclusion in perovskite crystal lattices, the function of guanidinium salts is still up for question. Gua ions passivate recombination/trap centers at grain boundaries, according to De Marco et al., rather than replacing MA ions.⁸² It was shown in later research that when modest amounts of guanidinium chloride are introduced, nearby perovskite grains are crosslinked by Gua ions. 83 Even when guanidinium chloride and guanidinium thiocyanate are used to optimize shape, Alotaibi et al. found that Gua ions do not incorporate into the perovskite phase. 82, 84

Prior to this, interface modification was primarily concerned with defect passivation, which might limit current faults but not stop new ones from arising, making it challenging to





attain FFs above 80% for PSCs. 85, 86 The small grain size of perovskites, which prevents charge movement between grain borders, is mostly to blame for the comparatively low FF. Defect density can be reduced by post-treating the perovskite surface to passivate flaws and adding chemicals to the perovskite precursor solution to increase grain size. However, it is difficult to discover an addition that makes grain size larger without negatively impacting perovskite stability. To enhance FF and lower V_{OC} loss between the charge transport layer and the perovskite layer, it is therefore imperative to concurrently decrease grain boundaries and passivate defects. 87-

In order to concurrently suppress nonradiative recombination losses at grain boundaries and the perovskite surface, we present in this work a novel approach called grain regrowth and defect passivation (GRDP). GuSCN was employed in this study as an interface modification layer to raise the inverted PSCs' power conversion efficiency (PCE) and stability. The hydrogen bonding ability of Gua⁺ and the coordination and/or ionic bonding capabilities of anions play crucial roles in defect passivation. The incorporation of guanidine halide in PSCs led to improvements in fill factor (FF) due to reduced interfacial recombination losses and enhanced conductivity. Notably, SCN had a major impact on the perovskite crystal structure. It has been demonstrated that using SAMs on the perovskite film improves the PCE and long-term stability of PSCs. Guanidinium thiocyanate, or GuSCN, was used as a SAM in this work to modify the perovskite films, Cs_{0.05}(FA_{0.85}MA_{0.15})_{0.95}Pb(I_{0.85}Br_{0.15})₃. Furthermore, the reduction of defect density and effective suppression of the charge recombination process result in enhanced PCE and stability. The device obtained a champion PCE of 19.95%, a Voc of 1.09 V, a Jsc of 24.69 mA/cm², and an FF of 74% with the addition of 1% GuSCN to the perovskite film. Compared to the counterpart lacking GuSCN, this is a 3% improvement. In addition, the improved Cs_{0.05}(FA_{0.85}MA_{0.15})_{0.95}Pb(I_{0.85}Br_{0.15})₃ PSC showed superior stability, holding onto almost 95% of its initial PCE after more than 60 days of storage without being encapsulated in a desiccator, as opposed to only 64% for pristine PSCs. This paper offers a straightforward method for lowering errors and enhancing PSC performance.





4.2. Experimental Section

The source of all the materials and the various characterization techniques used in this chapter are described in Chapter 2.

4.2.1. Perovskite solar cell fabrication:

Perovskite solar cell (PSC) devices were constructed using the architecture: FTO/c-TiO₂/m-TiO₂/Perovskite/HTM/Au. The fluorine-doped tin oxide (FTO) substrates (7 Ω /sq, Great Cell Solar) were patterned using 2M HCl and Zn powder, following the mask design. After patterning, the substrates were cleaned in an ultrasonic bath with Hellmanex (Sigma-Aldrich) for 30 minutes, followed by rinses with deionized water, acetone, and isopropanol, and finally treated with oxygen plasma for 20 minutes. A compact titanium dioxide (c-TiO₂) layer of approximately 30 nm was deposited on the FTO via spin coating at 6000 rpm for 30 seconds. This layer was derived from a precursor solution containing 0.1 mL of titanium diisopropoxide bis(acetylacetonate) in 1 mL ethanol. The coated substrates were then heated on a hotplate at 150 °C for 10 minutes, increased to 450 °C for 30 minutes, and then allowed to cool to room temperature. Subsequently, a mesoporous TiO₂ (m-TiO₂) layer was applied on the compact layer by spin coating for 20 seconds at 4000 rpm using Titania paste (MPT-20, Great Cell Solar) diluted in ethanol to achieve an approximate thickness of 150 nm. These substrates were dried at 125 °C for 10 minutes and then sintered at 500 °C for 30 minutes in a muffle furnace, followed by a slow cooling to room temperature. The mesoporous-coated substrates underwent sonication in ethanol for 15 minutes, treatment with a 0.1M TiCl₄ solution at 70 °C, and a final annealing at 450 °C for 30 minutes in a muffle furnace, before cooling to room temperature. The perovskite films were then deposited on the m-TiO₂ layer using a precursor solution of NH₂CHNH₂I (1 M), PbI₂ (1.1 M), CH₃NH₃Br (0.2 M), PbBr₂ (0.2 M), and CsI (0.075 M) in anhydrous DMF and DMSO (4:1 v/v). This solution was spin-coated in a two-step process at 1000 and 6000 rpm for 10 and 30 seconds, respectively. During the second step, 100 µL of chlorobenzene was dropped onto the spinning substrate 15 seconds before the end. The coated substrates were then annealed at 100 °C for 1 hour inside a glove box and allowed to cool. In this work, employed Guanidinium thiocyanate (GuSCN) used as a self-assembling molecule towards perovskite layer and HTM layer, 0%, 0.5%, 1%, 1.5%, 2% and 3% millimoles of GuSCN taken in anhydrous IPA solvent, coated on perovskite layer by spinning at 3000 rpm for 20s, then annealed at 100 °C for 10 mins. An





HTM solution (60 mM in chlorobenzene), doped with bis(trifluoromethylsulfonyl)imide lithium salt (Li-TFSI, Aldrich), tris(2-(1H-pyrazol-1-yl)-4-tert-butylpyridine)cobalt(III)tris(bis(trifluoromethylsulfonyl)imide) (FK209), and 4-tert-butylpyridine (TBP, Aldrich), was spin-coated onto the perovskite layer at 3000 rpm for 20 seconds. The molar ratios of Li-TFSI, FK209, and TBP were 0.5, 0.03, and 3.3, respectively. Finally, an 80 nm thick layer of gold was thermally evaporated under high vacuum onto the device. The schematic fabrication procedure shown in figure 4.1.

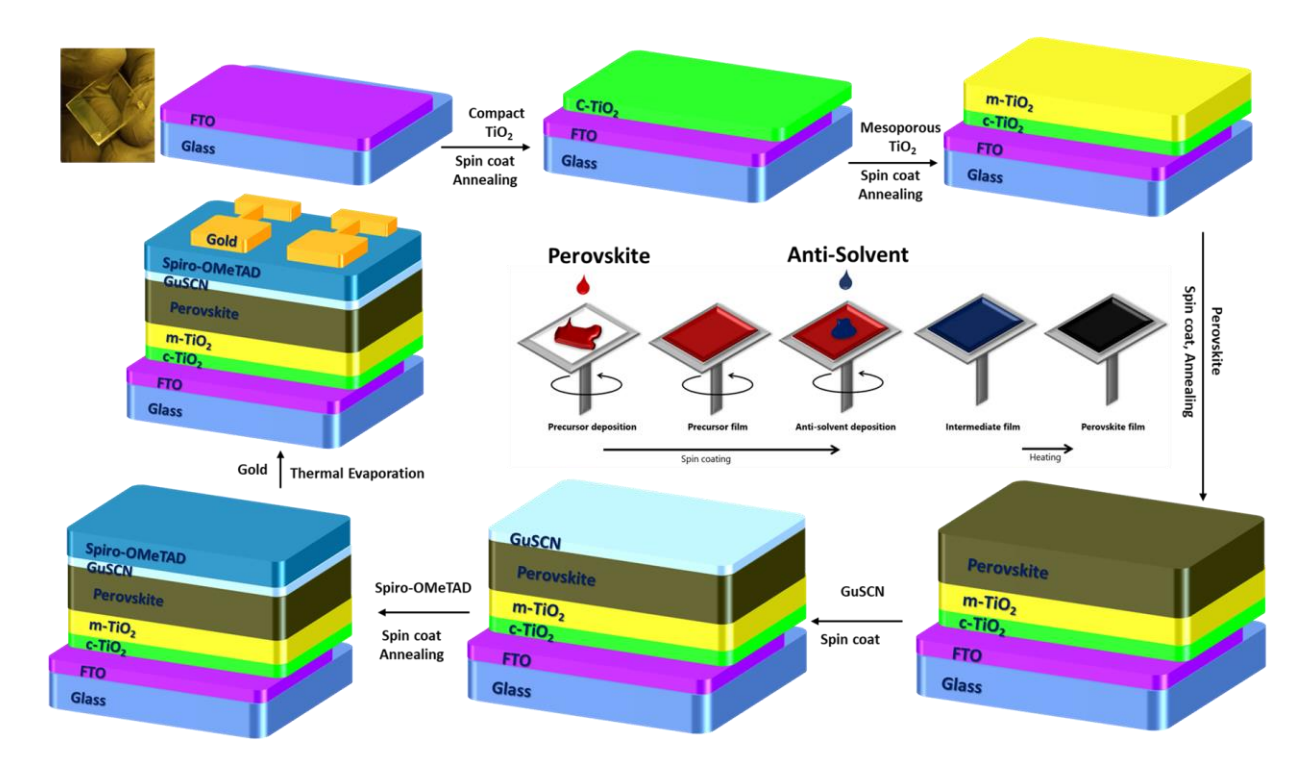


Figure. 4.1. Schematic route of fabrication of perovskite solar cell with the addition of GuSCN.

5.2.2. Hole mobility of Perovskite layer with and without GuSCN films:

To understand charge transport, we measured electron mobility using different electron transport layers (ETLs) within the same device structure. An electron-only device was designed with an FTO/TiO₂/PVK/Au configuration named as Ref and FTO/TiO₂/EDTA/PVK/Au named as EDTA. In this setup, we assumed the current is solely influenced by electrons. Neglecting diffusion and electric field effects, the current density was determined using the space-charge-limited current (SCLC) model. A 30-nm thick layer of compact TiO₂ coated onto FTO substrates, followed by spin-coating of m-TiO₂ on the FTO/c-TiO₂ layer, EDTA and Perovskite (PVK). Finally, another 80-nm thick Au layer was deposited on the FTO/TiO₂/EDTA/PVK and FTO/TiO₂/PVK samples. Dark current-voltage (J–V) measurements were performed using a



Keithley 2400 source under ambient conditions. The electron mobility (μ_e) was extracted by fitting the J–V curves according to the Mott–Gurney law.

The SCLC, I–V characteristics of the perovskite material under various environments, exhibited a sharp increase at V_{TFL} , where the current showed a significant rise (I \propto Vⁿ with n>3), indicating the transition to the trap-filled limit (TFL), where all trap states are occupied by charge carriers. Using the relationship between V_{TFL} and trap density (n_{traps}),

$$n_{traps} = \frac{2\varepsilon\varepsilon_0 V_{TFL}}{eL^2}$$

where ε is the dielectric constant of perovskite (usually taken 32 for FAPbI₃), ε_0 is the vacuum permittivity, L is the thickness of the material, and e is the elementary charge, we can estimate the trap density.

At higher biases, the current followed a quadratic dependence ($I \propto V^2$). By fitting this with the Mott-Gurney law,

$$J_d = \frac{9\varepsilon\varepsilon_0\mu V^2}{8L^3}$$

where J_d is the current density and V is the applied voltage, we can calculate the carrier mobility (μ) . The uncertainties represent the standard deviation based on measurements from five similar devices.

We can estimate the conductivity, conductance by using simple ohms law, further, the free charge carrier density (n_c) can be estimated using the relation $n_c = \sigma/e\mu$.

4.3. Results and Discussions

4.3.1. Spectral Characterization

To find out how GuSCN affected light absorbance, we looked at the perovskite films' ultraviolet-visible absorption spectra, as shown in Fig. 4.2(c). According to the findings, GuSCN improves perovskite films' ability to absorb light, especially in the 630–720 nm wavelength region. The ideal GuSCN concentration, which raises the *Jsc* of the gadget. The perovskite bandgaps of the Cs_{0.05}(FA_{0.85}MA_{0.15})_{0.95}Pb(I_{0.85}Br_{0.15})₃ perovskite, which are shown in Fig. 4.2(c) inset, demonstrate that GuSCN has no discernible effect on the perovskite bandgap. It remains at 1.6 eV.





To evaluate the grain quality, the X-ray diffraction (XRD) patterns of perovskite films are shown in Fig. 4.2(a). GuSCN concentrations greater than those without GuSCN cause the (100) crystal plane's diffraction peak to become more noticeable. Stronger peaks signify greater photovoltaic characteristics. Previous investigations have observed that the diffraction peaks of the (100) and (110) crystal planes are indicative of the photoactive α phase. GuSCN-treated perovskite films have narrower FWHM than control films, and as the GuSCN concentration increases, the FWHM values fall as well, suggesting that the GuSCN treatment causes the perovskite grains to enlarge. This result is consistent with the SEM images displayed in Fig. 4.2(e)–(f). Grain size is partially predicted by the XRD peak intensity, where larger grains are associated with higher intensity.

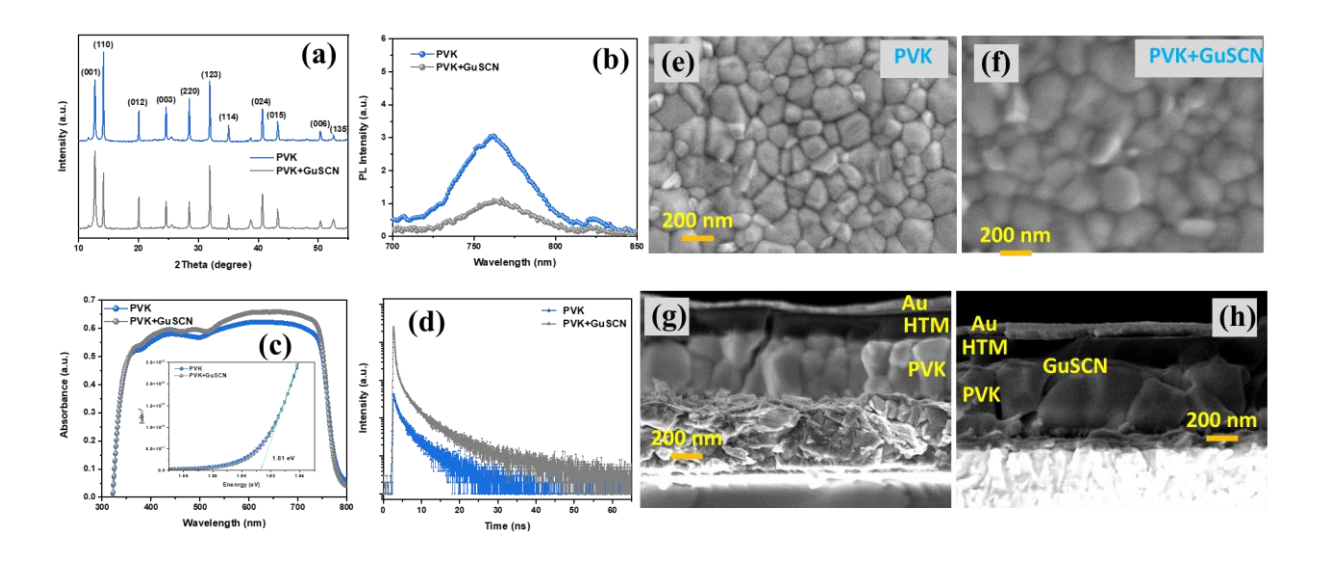


Figure. 4.2. (a) XRD spectra of perovskite (PVK), GuSCN on perovskite films. (c) absorbance spectra and tau plot of perovskite (PVK), GuSCN on perovskite films, (b, d) Emission spectra and TRPL of perovskite (PVK), GuSCN on perovskite films. (e, f) Top-view of of perovskite (PVK), GuSCN on perovskite films, (g, h) Cross-section FESEM of PSC with conventional and addition of GuSCN layers.

The impact of GuSCN on nonradiative recombination in perovskite films was investigated using steady-state photoluminescence (PL) spectra. No matter which direction the excitation light comes from, as shown in Fig. 4.2(b), the PL emission intensities of GuSCN-treated perovskite films are substantially lower than those of untreated control films. This implies that the perovskite films' nonradiative recombination is efficiently suppressed by GuSCN. Measurements of time-resolved photoluminescence (TRPL) validate this theory. As can be seen



in Fig. 4.2(d), the carrier lifetime in the perovskite treated with GuSCN is 36 ns, which is longer than the 20 ns seen in the control perovskite. The results show that GuSCN decreases the trap density in the perovskite film, which increases carrier lifetime and decreases nonradiative recombination.

The light absorber in this investigation used was the $Cs_{0.05}(FA_{0.85}MA_{0.15})_{0.95}Pb(I_{0.85}Br_{0.15})_3$ perovskite, which has a bandgap of 1.6 eV. GuSCN was added to the perovskite film as a post-treatment to improve its quality. Images from a surface scanning electron microscope (SEM) were utilized to track the morphological changes of perovskite films. The optimized concentration of GuSCN resulted in a notable increase of the perovskite grain sizes above the controlled perovskite film, as illustrated in Figure 4.2(e)–(f). Small grains were seen in the control perovskite films, but after treatment with 1 mmol% Grain boundary density was decreased and the average grain size was significantly raised using GuSCN. These results show that GuSCN efficiently promotes charge transfer within the perovskite layer, lowers grain boundary density, and promotes grain regeneration.

4.3.2. Photovoltaic Studies

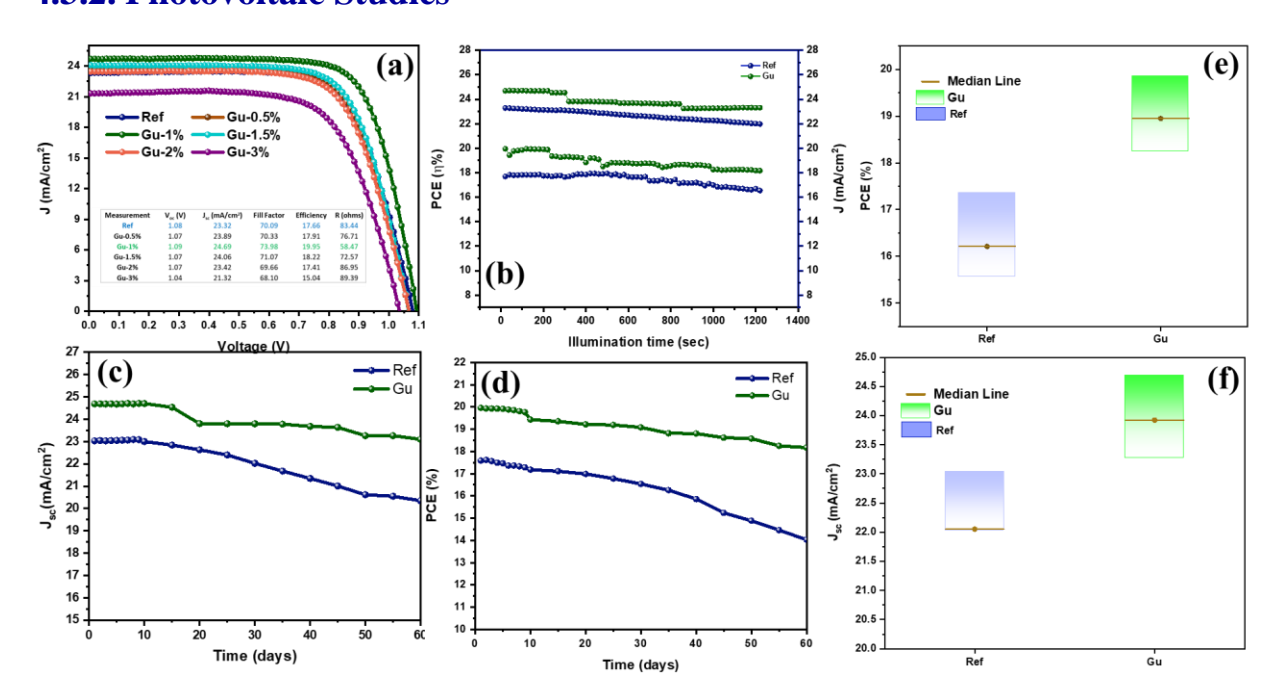


Fig. 4.3. (a) J-V characteristics parameters of Gu 0.5% to 3% and Ref devices, inset (table for all the photovoltaic parameters of Gu 0.5% to 3% and Ref devices), (b) Continuous irradiation of Gu and Ref devices under 1 sun, (c,d) Stability data of Gu and Ref devices with PCE and current densities respectively, (e, f) Reproducibility statistics of Gu and Ref devices





Based on the previously described enhanced optoelectronic capabilities, it is expected that the self-assembly of GuSCN on the perovskite layer will perform better than the controlled perovskite film. Thus, with the device structure FTO/c-TiO₂/m-TiO₂/Cs_{0.05}(FA_{0.85}MA_{0.15})_{0.95}Pb(I_{0.85}Br_{0.15})₃/GuSCN/ HTM/Au, planar-type PSCs were designed and produced utilizing a variety of ETLs. Because of its appropriate band gap and phase stability—which are further improved by a little amount of Cs doping—a triple cation perovskite was selected as the active absorber. Figure 4.2 (g, h) shows cross-sectional SEM images of the complete device structures with and without GuSCN, referred to as Gu and Ref devices, respectively, maintaining a perovskite film thickness of approximately 400 nm. Figures 4.2 (e, f) illustrate the perovskite layer morphology, revealing significantly larger grains with the addition of GuSCN. Figure 4.3a presents the J–V curves of planar-type PSCs using different mmol% of GuSCN, with key parameters like short-circuit current density (Jsc), Voc, fill factor (FF), and PCE summarized in Table 4.1. The device using 1 mmol% GuSCN achieves a PCE of 19.95%, with $Jsc = 24.69 \text{ mA/cm}^2$, Voc = 1.09 V, and FF = 74%. In comparison, the reference device which shows a PCE of 17.66%, with $Jsc = 23.32 \text{ mA/cm}^2$, Voc = 1.08 V, and FF = 70.09. Notably, incorporating GuSCN enhances Jsc, FF, and Voc to 24.69 mA/cm², 0.74 and 1.09 respectively, yielding a PCE of up to 19.95%. Since there is less hole mobility and more resistance, the device performs worse without GuSCN. This is explained by decreased *Jsc* and FF. On the other hand, planar-type PSCs containing GuSCN perform better, as seen by higher Jsc and FF. This is because improved hole mobility facilitates more efficient hole extraction, and a larger Voc results from a closer alignment of energy levels between HTM, GuSCN, and perovskite.

Measurement	V _{oc} (V)	J _{sc} (mA/cm ²)	Fill Factor	Efficiency	R (ohms)
Ref	1.08	23.32	70.09	17.66	83.44
Gu-0.5%	1.07	23.89	70.33	17.91	76.71
Gu-1%	1.09	24.69	73.98	19.95	58.47
Gu-1.5%	1.07	24.06	71.07	18.22	72.57
Gu-2%	1.07	23.42	69.66	17.41	86.95
Gu-3%	1.04	21.32	68.10	15.04	89.39

Table 4.1. Photovoltaic J-V data for the Gu 0.5% to 3% and Ref devices.

PSCs were also examined with 100 mW/cm² of continuous irradiation applied. PCE changes are displayed in Figure 4.3b, and Supplementary Table S6 provides specific J-V values.





When exposed to light for 1220 seconds, the GuSCN-based device keeps 95% of its initial efficiency, whereas the comparable device only keeps 80%. This demonstrates the Gu device's improved stability in both dark and continuous radiation scenarios. Perovskite film deterioration and spiro-OMeTAD HTL instability are the primary causes of PSC instability. Since the spiro-OMeTAD HTL was the same for all devices, there should be consistency in the degradation from the HTL between them. GuSCN deposition results in a threefold increase in the perovskite film's grain size, which enhances the environmental durability of GuSCN-based PSCs by reducing moisture infiltration at grain borders.

To further examine repeatability, data from 30 different devices for each Gu and Ref are shown in Figure 4.3(e, f). With data presented in Supplementary Table S7, Figure 4.3f displays the PCE distribution for devices with Gu and Ref devices. GuSCN is an excellent self-assembled monolayer (SAM) for planar-type PSCs, as demonstrated by the remarkable excellent repeatability and very minimal standard deviation of devices based on GuSCN when compared to Ref devices.

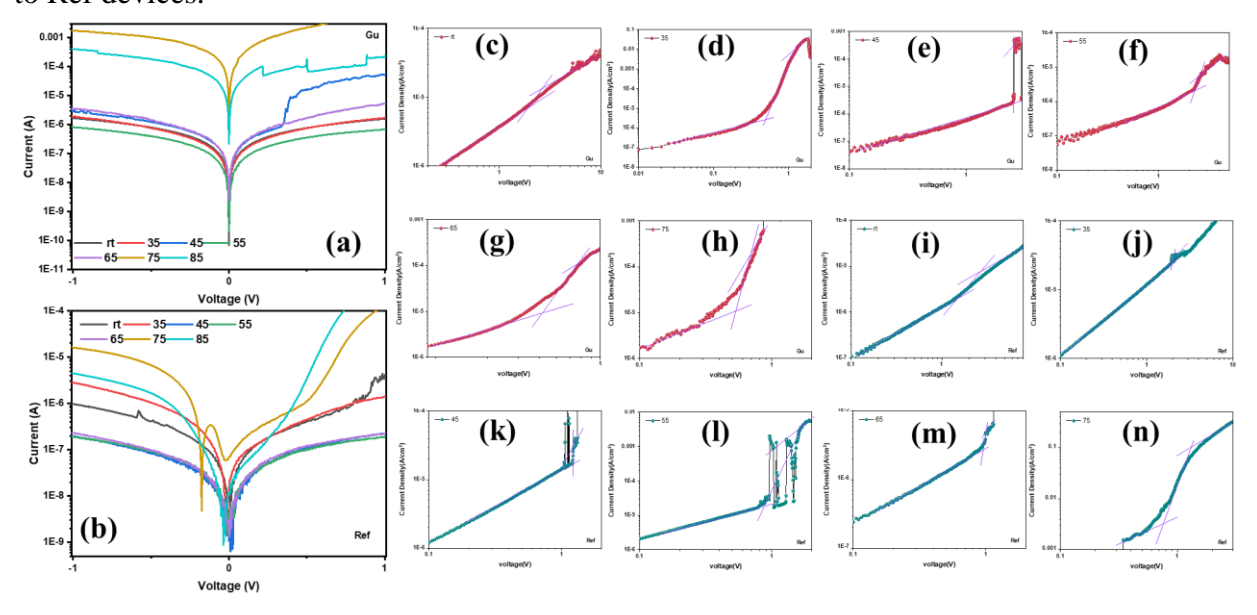


Figure. 4.4. (a,b) Semi log I-V curves of the Gu and Ref devices with hole only device, (c-h) semi log J-V curves of the Gu device with hole only device, at rt to 75°C, (i-n) semi log J-V curves of the Ref device with hole only device, at rt to 75°C.

4.3.3 Stability and Carrier Parameters

For PSCs, stability is essential. With comprehensive J–V parameters in Supplementary Table S8, Figures 4.3(c, d) display the PCE as a function of storage time. After 60 days of storage in ambient light without illumination, the GuSCN-based device maintains 90% of its original efficiency, compared to only 70% for the Ref device. The purpose of fabricating hole-only





devices with the structure FTO/perovskite/GuSCN/SpiroOMeTAD/Au was to evaluate the trap density in perovskite films placed on various substrates. For these devices, the dark current–voltage (I–V) curves are shown in Figures 4.4(a, b). The linear connection shows an ohmic response at low bias voltages. The traps are thought to be fully occupied when the current increases nonlinearly when the bias voltage beyond the kink point, also known as the trap-filled limit voltage (V_{TFL}). You can use the formula from Chapter 2 to determine the trap density (N_t). It is 1.34×10^{16} cm⁻³ for the perovskite film. The inclusion of GuSCN remarkably reduces this to 3.54×10^{15} cm⁻³. Because the perovskite layer has a reduced grain boundary density, there has been a notable decrease in trap density.

Additionally, the hole mobility of the doped Spiro-OMeTAD (approximately 10^{-4} cm² V⁻¹ s⁻¹) HTL is much faster than the electron mobility of the TiO₂ ETL, which is only 9.92×10^{-4} cm² V⁻¹ s⁻¹. Hysteresis is the outcome of charge accumulation brought on by this reduced electron mobility at the TiO2/perovskite/HTM interaction. On the other hand, when the high hole mobility perovskite/GuSCN (2.1×10^{-6} cm² V⁻¹ s⁻¹) is employed as the SAM, it improves hole transport from perovskite to GuSCN, resulting in little charge accumulation and hysteresis.

4.4. Conclusions

In conclusion, we provide a technique for both defect passivation and grain regrowth in triple cation PSCs to concurrently minimize nonradiative recombination losses at perovskite grain borders and surfaces. Grain regrowth is encouraged and bulk and boundary defects are decreased by applying GuSCN post-treatment to the perovskite film. The device's PCE, *Jsc*, *Voc*, and FF are so greatly improved by this modification. In comparison to the untreated reference PSCs, which had a PCE of 17.66%, the GuSCN-treated PSCs with a 1.66 eV bandgap reach 18%. Furthermore, after 60 days in a desiccator, the opaque PSC treated with GuSCN preserves 90% of its original PCE, indicating outstanding stability. In order to minimize nonradiative recombination losses in PSCs and regrowth perovskite grains, this work offers a simple and efficient method that will speed up PSC business.



Chapter 5

Exploring the Effects of Temperature Annealing on Electron Transport Layers to Ease the Perovskite Solar Cell Fabrication



Abstract

Organic-inorganic halide perovskites (OIHPs) have garnered significant attention in photovoltaic technology owing to their remarkable properties, such as high absorption coefficients, unprecedented long carrier diffusion lengths, ease of fabrication using solutionprocessed techniques, low optical band gaps, low recombination rates, ambipolar nature, and high charge carrier mobilities. Over the past decade, PSCs have made a linear progression, with numerous publications emerging worldwide. Currently, the PCE of perovskite solar cells exceeds 26%. fabricated device with the FTO/c-TiO₂/m-TiO₂/ we structure $Cs_{0.05}(FA_{0.85}MA_{0.15})_{0.95}Pb(I_{0.85}Br_{0.15})_3/GuSCN/HTM/Au$. However, the fabrication of PSCs typically being a laborious process of almost three days, involving the high-temperature annealing required for the electron-transporting layers. We hypothesized that by reducing the annealing temperatures, the overall performance of the device could be maintained while shortening the fabrication time. To validate this, we experimented with different annealing stages for each coating of compact TiO₂, mesoporous TiO₂, and TiCl₄ treatment. Ultimately, we achieved promising results by lowering the annealing temperatures for compact TiO2, resulting in a champion PCE of 18.03%, an *Voc* of 1.02 V, a *Jsc* of 24.08 mA/cm², and an FF of 73.46%. In this work, we have optimized the fabrication of PSCs by reducing procedural steps while maintaining performance metrics. By implementing a streamlined approach with reduced annealing temperatures for electron-transporting layers, we have accomplished decent efficiency gains compared to conventional methods. This research contributes to sustainable energy solutions by paving the way for more efficient production processes in perovskite solar cell technology.





5.1. Introduction

Among the most promising photovoltaic technologies are perovskite solar cells (PSCs), which employ organic-inorganic halide perovskite materials. They've made quick progress in the last few years, and their power conversion efficiencies (PCE) are now at 26.1%. PSCs have attracted a lot of attention because of their straightforward manufacturing method and inexpensive raw ingredients. The improvements in PSC performance can be primarily ascribed to the well-established fabrication methods that were taken from organic photovoltaic cells (OPVs)⁹⁰ and dye-sensitized solar cells (DSSCs)⁹¹, as well as to the extensive research that was conducted to enhance the optical, charge transport, and crystallinity properties of perovskite layers.^{53, 70, 92-94}

DSSCs and OPVs provided materials and technologies that PSC researchers initially used, especially for the charge and selective transport layers. The stability and functionality of PSCs are greatly influenced by the interfaces between the electron and hole transport layers (HTL and ETL) and the perovskite layer. Therefore, for further improving PSC performance and long-term stability, it is crucial to optimize these layers, improve the quality of the interface, and design novel charge transport layers that are well-aligned with the energy levels of perovskite materials. 95-97

The conventional ETL used in PSCs is titanium dioxide (TiO₂). With its conduction band minimum (CBM) matching that of perovskites, TiO₂ is an n-type high-bandgap semiconductor that offers effective electron transport with little energy loss. TiO₂ thin films come in three varieties that are commonly used in PSCs: mesoscopic, nanostructured, and compact (dense). The enormous surface area of mesoscopic and nanostructured films enables the presence of a large amount of photoactive material and strong light scattering, hence enhancing photon absorption. However, large surface areas and severe scattering effects are less critical because of the high absorption coefficient of perovskites. This makes the construction of planar PSCs with compact TiO₂ layers, which remove electrons from the perovskite layer and block holes from external electrodes, a simple and promising one. 98-101

Compact TiO₂ ETLs are frequently deposited using the spin-coating method. By varying the rotation rate, this straightforward technique makes it simple to modify the film's thickness. A crucial factor in ETLs is their thickness; while cutting it can lessen film resistance, doing so also runs the danger of creating pinholes and cracks, which can cause serious charge recombination.





Excessively thin films are not suited for use as ETLs since they can also show quantum size effects. In extremely thin films, tunneling can also lead to charge recombination. 102, 103

As a result, creating PSCs with great efficiency requires carefully adjusting the thickness of the charge transport layers. A thorough understanding of the charge transport processes in PSCs still requires thorough characterization methods, despite the abundance of research on ETL thickness tuning. For a deeper understanding of these phenomena, we used photoluminescence and impedance spectroscopy to create planar PSCs with compact TiO₂ ETLs and investigated the effect of TiO₂ ETL thickness on electronic processes.¹⁰⁴

The majority of high-efficiency PSCs on the market now rely on mesoporous designs, which are more expensive and can only be used in flexible and tandem devices when processing at high temperatures is necessary. In order to overcome this, low-temperature, economically viable synthesis techniques have been used to create planar-type PSCs. Planar-type PSCs, while still promising, usually obtain lower certified PCEs than their mesoporous counterparts. ¹⁰⁵

Due to its exceptional photoelectric characteristics, TiO₂ is still the most commonly employed ETL in high-efficiency n-i-p planar-type PSCs. In contrast to conventional HTLs, which have strong hole mobility (about 10⁻³ cm² V⁻¹ s⁻¹), TiO₂ has low electron mobility (about 10⁻⁴ cm² V⁻¹ s⁻¹), which causes charge accumulation at the TiO₂/perovskite interface, resulting in hysteresis and increased inefficiency. To enhance performance, chemical engineering and doping have been used in the development of low-temperature TiO₂ ETLs. One method of achieving a PCE of 20.1% is to change the TiO₂ microstructure at low temperatures by adding chlorine. ¹⁰⁶, ¹⁰⁷





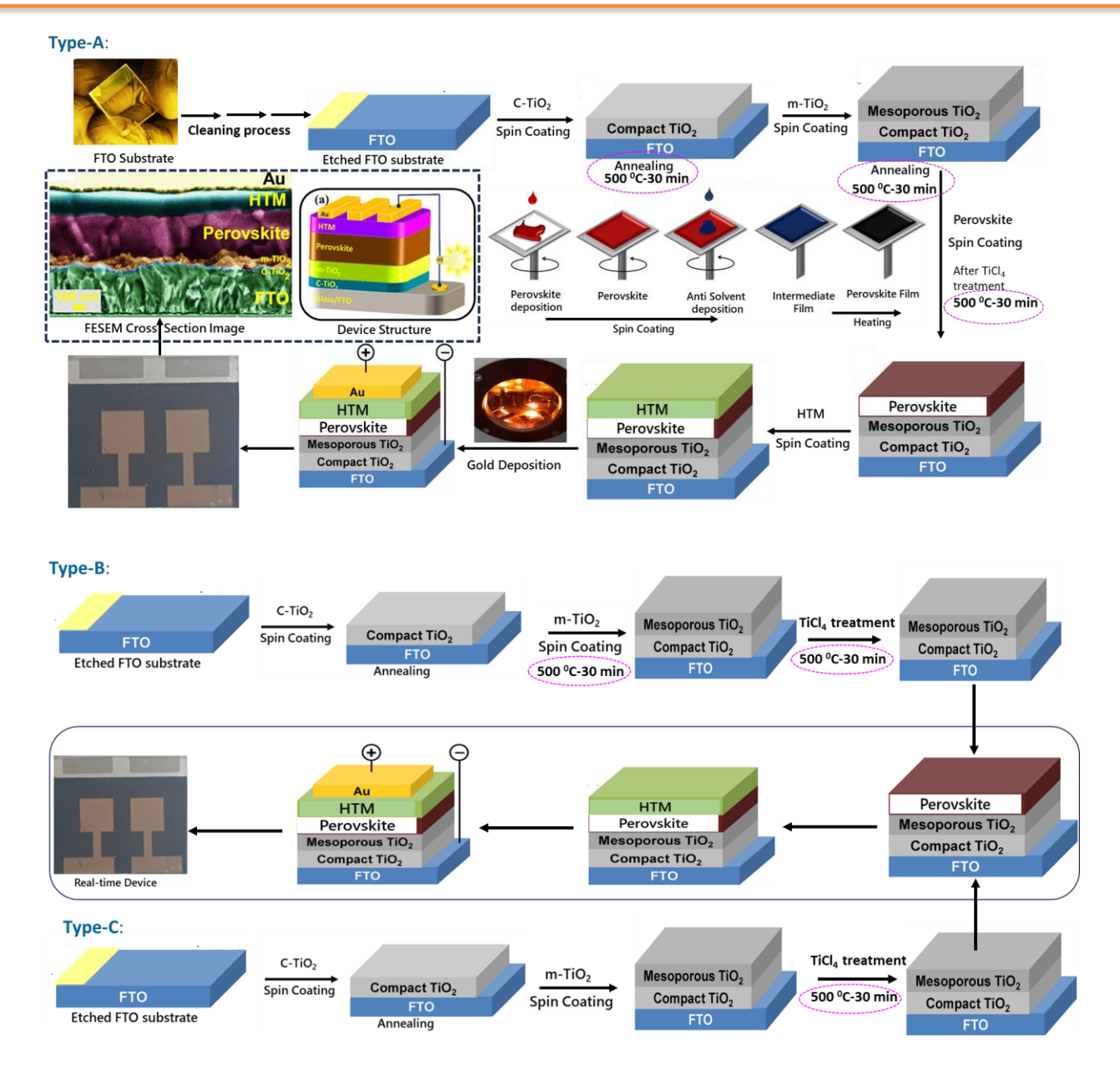


Figure. 5.1. Schematic route of fabrication of perovskite solar cell with ETL layer different annealing stages prescribed in Type-A, B and C.

5.2. Experimental Section

Perovskite solar cell (PSC) devices were fabricated following the structure: $FTO/c-TiO_2/m-TiO_2/Perovskite/HTM/Au$. The fluorine-doped tin oxide (FTO) substrates (7 Ω/sq) from Great Cell Solar were etched using a 2M HCl and Zn powder solution according to the mask design. The substrates were then cleaned in an ultrasonic bath using Hellmanex (from Sigma-Aldrich) for 30 minutes, rinsed with deionized water, acetone, and isopropanol, and finally treated with oxygen plasma for 20 minutes. A compact layer of titanium dioxide (c-TiO₂), approximately 30



nm thick, was deposited on the FTO by spin coating at 6000 rpm for 30 seconds. This layer was prepared from a precursor solution of 0.1 mL titanium diisopropoxide bis(acetylacetonate) in 1 mL ethanol. The coated substrates were heated on a hotplate at 150 °C for 10 minutes, followed by 500 °C for 30 minutes, and then allowed to cool to room temperature. Next, a mesoporous TiO2 (m-TiO2) layer was spin-coated on top of the compact layer at 4000 rpm for 20 seconds, using Titania paste (MPT-20, Great Cell Solar) diluted in ethanol to achieve a thickness of about 150 nm. These substrates were then dried at 125 °C for 10 minutes, sintered at 500 °C for 30 minutes in a muffle furnace, and cooled to room temperature. The mesoporous-coated substrates were then sonicated in ethanol for 15 minutes, treated with a 0.1M TiCl₄ solution at 70 °C, and annealed at 500 °C for 30 minutes in a muffle furnace, followed by cooling to room temperature. However, the fabrication of PSCs typically being a laborious process of almost three days, involving the high-temperature annealing required for the electron-transporting layers. We hypothesized that by reducing the annealing temperatures, the overall performance of the device could be maintained while shortening the fabrication time. To validate this, we experimented with different annealing stages for each coating of compact TiO₂, mesoporous TiO₂, and TiCl₄ treatment. Each stage of annealing limited to particular layer/treatment, following same as mentioned fabrication procedure, taken as Type-A, skipping only c-TiO₂ annealing at high temperature taken as Type-B and skipping both c-TiO₂ annealing and c-TiO₂ annealing at high temperature taken as Type-C. The complete schematic procedure of the PSC fabrication shown in figure 5.1 a and b. For all, followed the same remaining procedural fabrication, the perovskite films were deposited on the m-TiO₂ layer using a precursor solution composed of NH₂CHNH₂I (1 M), PbI₂ (1.1 M), CH₃NH₃Br (0.2 M), PbBr₂ (0.2 M), and CsI (0.075 M) in an anhydrous DMF: DMSO mixture (4:1 v/v). The perovskite solution was applied using a two-step spincoating process at 1000 and 6000 rpm for 10 and 30 seconds, respectively. During the second step, 100 µL of chlorobenzene was added to the spinning substrate 15 seconds before the end of the process. The substrates were then annealed at 100 °C for 1 hour in a glove box and allowed to cool. The hole transport material (HTM) solution, which was 60 mM in chlorobenzene and doped with bis(trifluoromethylsulfonyl)imide lithium salt (Li-TFSI, Aldrich), tris(2-(1Hpyrazol-1-yl)-4-tert-butylpyridine)cobalt(III)tris(bis(trifluoromethylsulfonyl)imide) (FK209), and 4-tert-butylpyridine (TBP, Aldrich), was then spin-coated onto the perovskite layer at 3000 rpm for 20 seconds. The molar ratios for Li-TFSI, FK209, and TBP in the HTM were 0.5, 0.03, and 3.3, respectively. Finally, an 80 nm layer of gold was thermally evaporated under high vacuum onto the device.





5.2.2. Electron mobility of Perovskite layer with Type- A, B and C layers:

To understand charge transport, we measured electron mobility using different electron transport layers (ETLs) within the same device structure. An electron-only device was designed with an FTO/TiO₂/PVK/Au configuration named as Ref and FTO/TiO₂/EDTA/PVK/Au named as EDTA. In this setup, we assumed the current is solely influenced by electrons. Neglecting diffusion and electric field effects, the current density was determined using the space-charge-limited current (SCLC) model. A 30-nm thick layer of compact TiO₂ coated onto FTO substrates, followed by spin-coating of m-TiO₂ on the FTO/c-TiO₂ layer, EDTA and Perovskite (PVK). Finally, another 80-nm thick Au layer was deposited on the FTO/TiO₂/EDTA/PVK and FTO/TiO₂/PVK samples. Dark current-voltage (J–V) measurements were performed using a Keithley 2400 source under ambient conditions. The electron mobility (μ_e) was extracted by fitting the J–V curves according to the Mott–Gurney law.

The SCLC, I–V characteristics of the perovskite material under various environments, exhibited a sharp increase at V_{TFL} , where the current showed a significant rise (I \propto Vⁿ with n>3), indicating the transition to the trap-filled limit (TFL), where all trap states are occupied by charge carriers. Using the relationship between V_{TFL} and trap density (n_{traps}),

$$n_{traps} = \frac{2\varepsilon\varepsilon_0 V_{TFL}}{eL^2}$$

where ε is the dielectric constant of perovskite (usually taken 32 for FAPbI₃), ε_0 is the vacuum permittivity, L is the thickness of the material, and e is the elementary charge, we can estimate the trap density.

At higher biases, the current followed a quadratic dependence ($I \propto V^2$). By fitting this with the Mott-Gurney law,

$$J_d = \frac{9\varepsilon\varepsilon_0\mu V^2}{8L^3}$$

where J_d is the current density and V is the applied voltage, we can calculate the carrier mobility (μ) . The uncertainties represent the standard deviation based on measurements from five similar devices.

We can estimate the conductivity, conductance by using simple ohms law, further, the free charge carrier density (n_c) can be estimated using the relation $n_c = \sigma/e\mu$.





5.3. Results and Discussions

5.3.1. Photophysical Properties

Figure 5.2 (c and d) depicts the absorption and transmittance spectra of TiO₂ films and coated perovskite film for absorbance studies and TiO₂ films for transmittance studies, which are known for their strong UV absorption due to their wide-band gap semiconductor properties. The spectra indicate that as the TiO₂ films Type-A, Type-B and Type-C with different annealing stages, the absorption intensity diminishes. Using the Tauc plot method, the optical band gap of these films was estimated, and all gave nearly same band gap 1.6 eV.

Then, employing photoluminescence quenching as an indication, we examined the impact of TiO2 layer thickness on charge transfer from a perovskite layer to a TiO2. The luminescence properties of TiO2 films containing perovskite were examined in order to comprehend the effects of varying annealing stages and defects. Type-A through Type-C luminescence spectra of TiO2+Perovskite films annealed at various stages are displayed in Figure 5.2e. Perovskite layers on several types of glass substrates are shown in the spectrum's photoluminescence spectra. λmax = 785 nm is the photoluminescence peak seen in the perovskite. The highest fluorescence intensity is observed, as expected, in the perovskite layer on the glass substrate. On the other hand, fluorescence is visibly quenched upon deposition on TiO2 layers. Effective electron transport from the perovskite to TiO2 was first demonstrated by an increase in quenching upon reduction of TiO2 with Type-C to Type-A, indicating that charge transfer is inhibited.

Time-resolved photoluminescence (TRPL) was utilized to evaluate PL lifetimes (τ PL) and compare the PL intensity degradation for different types of perovskite layers on TiO2. The PL intensity decay for perovskite layers is faster and for TiO2 layers is higher, as Figure 5.2f shows. But the PL decay period increases for thinner layers of TiO2, suggesting a decline in charge transfer efficiency.

Figure 3.2b displays X-ray diffraction (XRD) data for multi-crystalline perovskite thin films deposited on glass substrates. The samples include perovskite directly coated on types A to C TiO₂. The XRD patterns show distinct perovskite diffraction peaks at approximately "14.2°, 20.1°, 24.7°, 28.6°, 32°, 35.2°, 40.8°, 43.4°, 50.5°, and 52.7°, corresponding to the (110), (012), (003), (220), (123), (114), (024), (015), (006), and (135) lattice planes," respectively. The XRD





spectrum of the ground crystal confirms that no additional phases are present other than the cubic phase, verifying the purity of the triple cation perovskite.

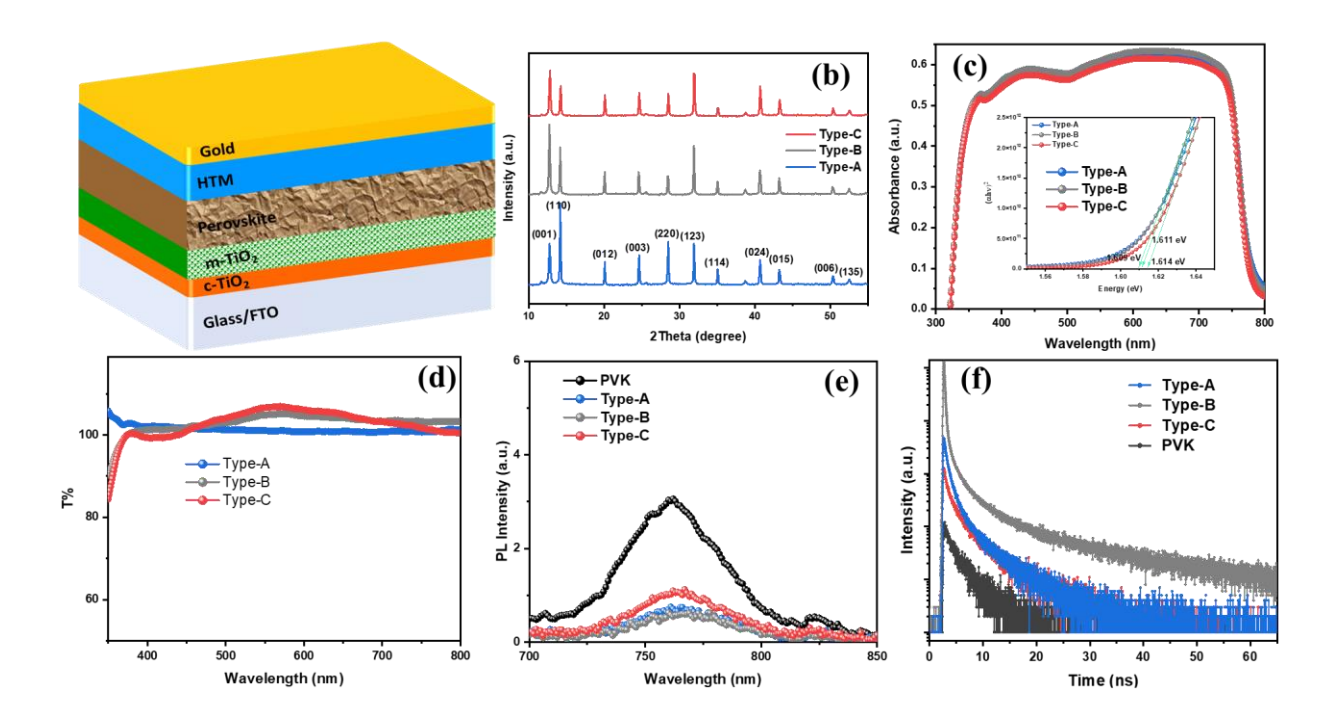


Figure 5.2. (a) Conventional Device architectire for perovskite solar cells (b) XRD spectra of perovskite (PVK), perovskite on Type-A, B and C ETL annealing stages films. (b) absorbance spectra and tau plot (inset) of perovskite (PVK), perovskite on Type-A, B and C ETL films. (b) Transmittance spectra Type-A, B and C ETL films. (e, f) Emission spectra and TRPL of perovskite (PVK), perovskite on Type-A, B and C ETL films.

5.3.2. Photoelectric Properties:

Building on the previously discussed superior optoelectronic properties, the types of devices fabricated with different annealing stages, even though at lower temperature annealing can outperform without compromising the photovoltaic properties. To explore this, planar-type PSCs were designed and fabricated using various annealing stages ETLs mentioned in fabrication procedure, with the device structure FTO/c-TiO₂/m-TiO₂/ Cs_{0.05}(FA_{0.85}MA_{0.15})_{0.95}Pb(I_{0.85}Br_{0.15})₃/ HTM/Au. An appropriate band gap and phase stability, augmented by a minor doping of Cs, led to the selection of a triple cation perovskite as the active absorber. Keeping the perovskite layer thickness at about 400 nm, cross-sectional SEM pictures of the whole device structures of type-A through C are displayed in Figure 5.3 (d, e, f). Figures 5.3 (a, b, c) illustrate the perovskite



layer morphology on TiO₂ layer annealing at different stages named as type A to C, revealing significantly larger grains for type-B. Figures 5.3 (g, h, i) represents the morphology of c-TiO₂/m-TiO₂/TiCl₄ combinedly, but as mentioned fabrication section, layers annealed at different stages of higher temperatures.

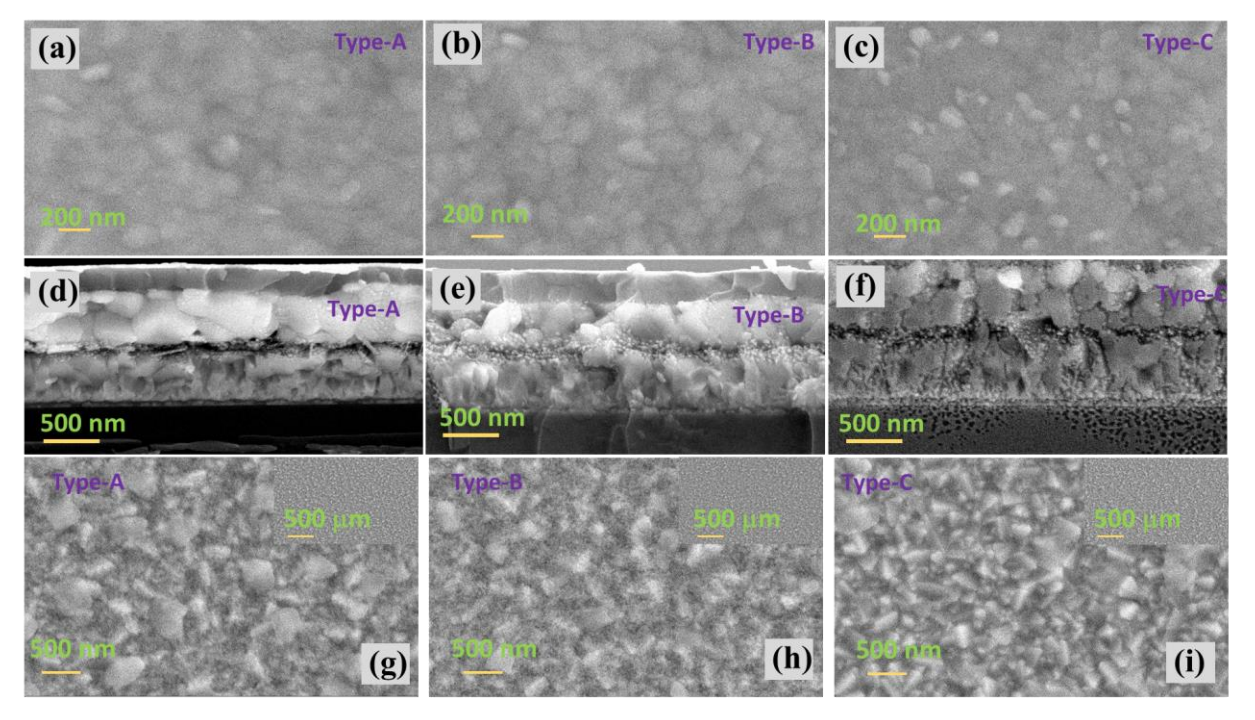


Figure. 5.3. (a, b,c) Top-view of perovskite film on Type-A, B and C ETL annealing stages films , (g, h, i) Top-view of Type-A, B and C ETL annealing stages films, (d, e, f) Cross-section FESEM of PSC with Type-A, B and C devices.

Key parameters such as the fill factor (FF), PCE, *Voc*, short-circuit current density (*Jsc*), and fill factor (A) are presented in Table 5.1. Figure 5.4a shows the J–V curves of planar-type PSCs utilizing different kinds, A to C, with FF = 73.46%, *Voc* = 1.02 V, *Jsc* = 24.08 mA/cm², and PCE of 18.06%, the type-B device is utilized successfully. FF = 72.88%, *Voc* = 1.03 V, *Jsc* = 23.06 mA/cm², and PCE of 17.36% are displayed by the reference device (Type-A), in contrast. Notably, by skipping the annealing temperature of c-TiO₂ layer at higher temperatures, the performance getting enhanced. The lower performance of the device by skipping both higher annealing temperatures of c-TiO₂ and m-TiO₂ attributed to lower hole mobility and higher resistance. In contrast, planar-type PSCs with type-B exhibit superior performance, indicated by higher *Jsc* and FF, thanks to higher hole mobility promoting effective hole extraction, and a larger *Voc*, even though, intentionally missing the higher annealing temperatures of c-TiO₂. PSCs were also evaluated at 100 mW/cm2 under continuous irradiation. With specific J–V parameters found



in Supplementary Table 9, Figure 5.4b illustrates how the PCE varies over time. After 1320 seconds of illumination, the all-type devices type-A to C deuterated its efficiency and current density values. From the graph, we understand that the higher annealing temperatures is necessarily needed for the mesoporous TiO₂ layer, since type-C degraded very quickly under continuous sun light irradiation. This shows that the gadgets' stability is deteriorating under both continuous and dark illumination. Perovskite film deterioration and spiro-OMeTAD HTL instability are the primary causes of PSC instability. Since the spiro-OMeTAD HTL was the same for all devices, there should be consistency in the degradation from the HTL between them. Additionally, to examine repeatability, Figure 5.4 (e, f) shows data from 30 different devices for each type and Ref. For devices with varying ETL annealings, Figure 5.4f displays the PCE distribution, with statistics found in Supplementary Tables S12. Surprisingly, one of the most important factors for PSCs is device stability. With comprehensive J–V parameters supplied in Supplementary Table S11, Figures 5.4(c, d) show the PCE as a function of storage time. After 30 days, 70% of the device's initial efficiency is still present.

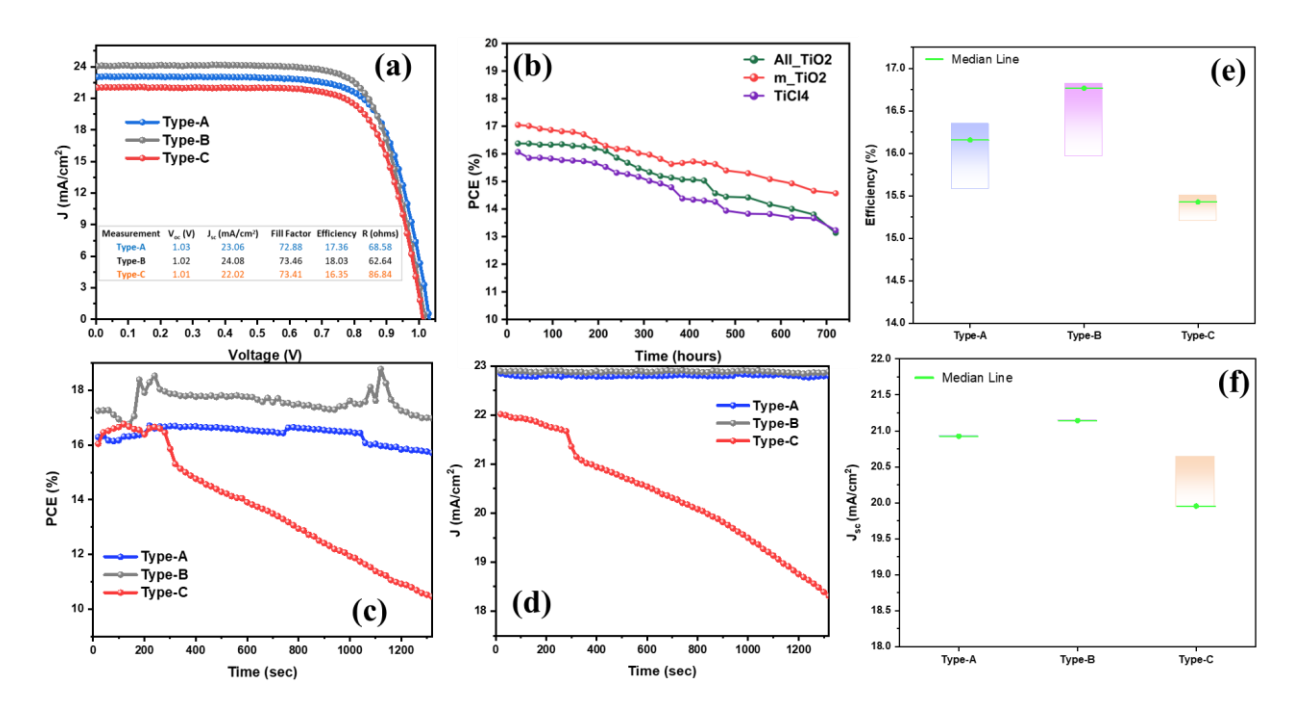


Figure. 5.4. (a) J-V characteristics parameters of Type- A, B and C devices, inset (table for all the photovoltaic parameters of Type- A, B and C devices), (b) Stability data of Type- A, B and C devices with PCE, (c, d) Continuous irradiation of Type- A, B and C devices under 1 sun (e, f) R eproducibility statistics of Type- A, B and C devices.



Measurement	V _{oc} (V)	J _{sc} (mA/cm ²)	Fill Factor	Efficiency	R (ohms)
Type-A	1.03	23.06	72.88	17.36	68.58
Type-B	1.02	24.08	73.46	18.03	62.64
Type-C	1.01	22.02	73.41	16.35	86.84

Table 4.1. Photovoltaic J-V data for the Type-A, B and C devices.

5.3.2. Stability and carrier studies:

Electron-only devices with the structure FTO/c-TiO₂/ m-TiO₂/TiCl₄/perovskite/Au were created in order to assess the trap density in perovskite films formed on Type-A to C. For these devices, the dark current–voltage (I–V) curves are displayed in Figures 5.5(a), b, and c). Ohmic response is indicated by the linear relationship at low bias voltages. The current increases nonlinearly, signifying that the traps are fully occupied, when the bias voltage exceeds the kink point, also known as the trap-filled limit voltage (V_{TFL}). The equation discussed in Chapter 2 can be used to compute the trap density (N_t). For type-B, the trap density dramatically drops to 1.2×10^{15} cm⁻³ from 4.53×10^{15} cm⁻³ for the perovskite film. Mentioned in supplementer table S13-15. The reduced density of the grain boundary in the perovskite film is responsible for this significant decrease in trap density.

Additionally, the TiO_2 ETL's electron mobility is only 9.92×10^{-4} cm² V⁻¹ s⁻¹, which is almost an order of magnitude slower than the doped Spiro-OMeTAD's hole mobility (around 10^{-3} cm² V⁻¹ s⁻¹) HTL. Hysteresis is brought on by the decreased electron mobility, which causes charge accumulation at the TiO_2 /perovskite/HTM contact. However, when utilizing perovskite, which has a high electron mobility (2.27×10^{-3} cm² V⁻¹ s⁻¹), it improves electron transport from the perovskite to TiO_2 layers, which results in very little charge accumulation and hysteresis and has very good repeatability with a tiny standard deviation.



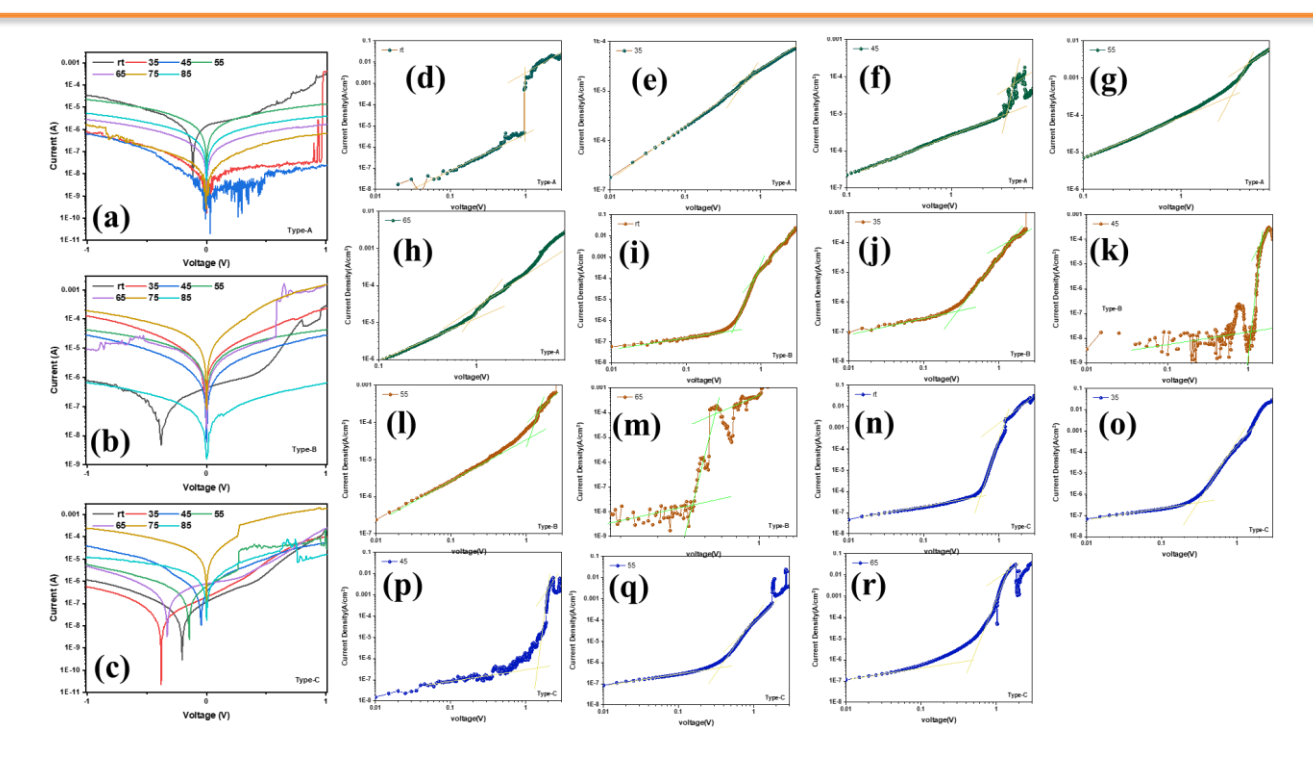


Figure. 5.5. (a, b, c) Semi log I-V curves of the Type- A, B and C devices with electron only device, (d-h) semi log J-V curves of the Type-A devices with electron only device, at rt to 65^oC, (i-m) semi log J-V curves of the Type-B devices with electron only device, at rt to 65^oC. (n-r) semi log J-V curves of the Type-C devices with electron only device, at rt to 65^oC.

5.4. Conclusions

In conclusion, the high-temperature annealing needed for the electron-transport layers causes the conventional method of creating perovskite solar cells (PSCs) to be labor-intensive. We reasoned that the fabrication time may be reduced without sacrificing device performance by reducing the annealing temperatures. We changed the annealing temperatures for compact TiO₂, mesoporous TiO₂, and TiCl₄ treatment for each layer in order to evaluate this. According to our experiments, compact TiO₂ performed well when the annealing temperatures were lowered. Our maximum power conversion efficiency (PCE), which is comparable to traditional devices, was 18.03%. Through process simplification and excellent performance preservation, this study successfully optimized PSC manufacture. We have advanced perovskite solar cell technology and increased efficiency by using a more effective annealing strategy, which helps to create more sustainable energy production ways.



Chapter 6

Summary and Conclusion



6.1. Summary

Chapter-1:

This section provides a comprehensive statistical review of energy consumption and production globally and in India. It covers the evolution of solar cells, highlighting the significance of perovskite solar cells over silicon solar cells. Additionally, it delves into the background, working principles, key properties, and advantages of perovskite solar cells. Current commercialization issues, causes of degradation, and methods to enhance the stability and durability of perovskite solar cells are discussed comprehensively.

Chapter-2:

This section presents the fundamental scientific concepts essential to this dissertation, which is primarily based on semiconductor physics with a focus on the energetics of the materials used. Key quantities are introduced and are briefly discussed, followed by an explanation of semiconductor junctions and their importance in solar cells. The principles of photovoltaics and the operation of solar cells are examined. Halide perovskite solar cells (PSCs) and their most significant characteristics are introduced, besides a discussion on crucial parameters such as power conversion efficiency, fill factor, short circuit current density, voltage at open circuit, conductivity, mobility, trap field density, and carrier density of electrons and holes, using relevant equations. The fabrication procedures, materials procured, experimental methods, and various instruments used for characterizing the samples in all the working chapters are also described.

Chapter-3:

It is known that EDTA can form complexes with transition metal oxides by donating its lone-pair electrons to the vacant d-orbital of the transition metal atom. We hypothesized that EDTA-modified TiO₂ would serve as a more effective electron transport layer (ETL) in PSCs than TiO₂ alone. To test this, we designed and fabricated an EDTA-TiO₂ based device with the structure FTO/c-TiO₂/m-TiO₂/EDTA/Cs_{0.05}(FA_{0.85}MA_{0.15})_{0.95}Pb(I_{0.85}Br_{0.15})₃/HTM/Au.

 $Cs_{0.05}(FA_{0.85}MA_{0.15})_{0.95}Pb(I_{0.85}Br_{0.15})_3$ was used as the active absorber due to its appropriate band gap and enhanced phase stability through Cs doping. The J-V curves of planar-type PSCs using EDTA-TiO₂ and TiO₂-based ETLs were analysed, with key parameters such as short-circuit current density (Jsc), open-circuit voltage (Voc), fill factor (FF), and PCE. The device with EDTA-TiO₂ achieved a PCE of 19.77%, with Jsc = 25.07 mA/cm², Voc = 1.04 V, and FF = 75.50.





In comparison, the device with TiO_2 (reference) showed a PCE of 17.58%, with Jsc = 23.03 mA/cm², Voc = 1.05 V, and FF = 73.05. The superior performance of the EDTA-TiO₂ ETL is attributed to higher electron mobility, which enhances electron extraction, and a larger Voc due to the closer energy level alignment between EDTA-TiO₂ and the perovskite. Continuous illumination studies over 20 minutes demonstrated consistent PCE and current densities. Stability tests showed that the EDTA-TiO₂ based device retained 99% of its efficiency over 60 days, whereas the reference device with TiO_2 experienced a drop of more than 3% of its PCE. Further studies on electron-only device carrier parameters using conductivity and space-charge-limited conduction (SCLC) measurements at different temperatures confirmed the robustness of the EDTA-TiO₂ ETL even at higher temperatures. In this work, we have successfully developed EDTA-complexed TiO_2 ETLs for planar-type PSCs, achieving a PCE as high as 19.77%. Additionally, the TiO_2 -based PSCs exhibited negligible hysteresis due to the elimination of charge accumulation at the perovskite/ETL interface and improved electron extraction. Furthermore, EDTA treatment rendered the TiO_2 surface more hydrophilic, reducing the Gibbs free energy for heterogeneous nucleation and resulting in higher quality perovskite films.

Chapter-4:

Employing self-assembled monolayers (SAMs) is a notable technique for interface engineering across various fields. SAMs are molecular assemblies that spontaneously form on a substrate through adsorption and typically consist of an anchoring group, a linker, and a functional group. The anchoring group enables the molecules to interact with the surface and arrange themselves in an orderly fashion, which is crucial for functionalization. The linker, often an aliphatic chain, influences the supramolecular structure via Van der Waals interactions, while the functional group plays a key role in modifying the surface properties.

Following the approach described in Chapter 3, we have fabricated a device with configuration FTO/c-TiO₂/m-TiO₂ /Cs_{0.05}(FA_{0.85}MA_{0.15})_{0.95}Pb(I_{0.85}Br_{0.15})₃/GuSCN/HTM/Au. Employing SAMs on the perovskite film is proven to be an effective method to ameliorate the PCE and long-term stability of perovskite solar cells (PSCs). In this work, the perovskite films, Cs_{0.05}(FA_{0.85}MA_{0.15})_{0.95}Pb(I_{0.85}Br_{0.15})₃, were modified with guanidinium thiocyanate (GuSCN) as a SAM. Upon introduction of the GuSCN precursor solution to the perovskite film, the crystal quality of the resulting films improved, with enhanced orientations of the (100) and (200) crystal planes. This optimization of energy level alignment benefits electron extraction. Additionally, defect density is reduced, and the charge recombination process is effectively suppressed, leading





to improved PCE and stability. With the addition of 1% GuSCN to the perovskite film, the device achieved a champion PCE of 19.95%, an *Voc* of 1.09 V, a *Jsc* of 24.69 mA/cm², and a FF of 74%. This represents a 3% improvement over the counterpart without GuSCN. The enhanced Cs_{0.05}(FA_{0.85}MA_{0.15})_{0.95}Pb(I_{0.85}Br_{0.15})₃ PSC also demonstrated better stability, retaining approximately 95% of its initial PCE after being stored for over 60 days without encapsulation in a desiccator, compared to only 64% for pristine PSCs. This work provides a simple strategy for reducing defects and improving the performance of PSCs. Further studies on hole-only device carrier parameters using conductivity and SCLC measurements at different temperatures confirmed the sustainability of the GuSCN PSCs even at higher temperatures.

Chapter-5

Organic-inorganic halide perovskites (OIHPs) have garnered significant attention in photovoltaic technology owing to their remarkable properties, such as high absorption coefficients, unprecedented long carrier diffusion lengths, ease of fabrication using solution-processed techniques, low optical band gaps, low recombination rates, ambipolar nature, and high charge carrier mobilities. Over the past decade, PSCs have made a linear progression, with numerous publications emerging worldwide. Currently, the PCE of perovskite solar cells exceeds 26%. Following the approach described in Chapter 3, we fabricated a device with the structure FTO/c- TiO_2/m - $TiO_2/Cs_{0.05}(FA_{0.85}MA_{0.15})_{0.95}Pb(I_{0.85}Br_{0.15})_3/GuSCN/$ HTM/ Au. fabrication of PSCs typically being a laborious process of almost three days, involving the hightemperature annealing required for the electron-transporting layers. We hypothesized that by reducing the annealing temperatures, the overall performance of the device could be maintained while shortening the fabrication time. To validate this, we experimented with different annealing stages for each coating of compact TiO₂, mesoporous TiO₂, and TiCl₄ treatment. Ultimately, we achieved promising results by lowering the annealing temperatures for compact TiO2, resulting in a champion PCE of 18.03%, an Voc of 1.02 V, a Jsc of 24.08 mA/cm², and an FF of 73.46%. In this work, we have optimized the fabrication of PSCs by reducing procedural steps while maintaining performance metrics. By implementing a streamlined approach with reduced annealing temperatures for electron-transporting layers, we have accomplished decent efficiency gains compared to conventional methods. We also investigated carrier mobilities, concentrations, and trap densities at various temperatures, demonstrating the stability and performance of the PSCs under higher temperatures. This research contributes to sustainable energy solutions by paving the way for more efficient production processes in perovskite solar cell technology.





Chapter-6

Deals with the summary and conclusion of the complete thesis work, in addition, the future scopes of this work also outlined.

6.2. Conclusion

In chapter 3, The PCE of planar-type PSCs was increased to 19.77% with minimal hysteresis through the development of an extremely efficient EDTA-TiO₂ ETL. These planar-type PSCs exhibit exceptional performance because of the superior (bigger grain size, reduced trap density, and excellent crystallinity) perovskite films produced atop EDTA-TiO₂ ETLs. Because of the improved electron transport and less charge accumulation at the interface caused by the increased electron mobility, there is less J-V hysteresis and high efficiency. The longer grain size also increases stability over time by reducing perovskite breakdown at grain borders. Perovskite photovoltaics is predicted to advance with the help of this work, which demonstrates a promising method for creating high-quality ETLs.

In chapter 4 conclusion, we provide a technique for both defect passivation and grain regrowth in triple cation PSCs to concurrently minimize nonradiative recombination losses at perovskite grain borders and surfaces. Grain regrowth is encouraged and bulk and boundary defects are decreased by applying GuSCN post-treatment to the perovskite film. The device's PCE, *Jsc*, *Voc*, and FF are so greatly improved by this modification. In comparison to the untreated reference PSCs, which had a PCE of 17.66%, the GuSCN-treated PSCs with a 1.66 eV bandgap reach 18%. Furthermore, after 60 days in a desiccator, the opaque PSC treated with GuSCN preserves 90% of its original PCE, indicating outstanding stability. In order to minimize nonradiative recombination losses in PSCs and regrowth perovskite grains, this work offers a simple and efficient method that will speed up PSC business.

In chapter 5 conclusion, the high-temperature annealing needed for the electron-transport layers causes the conventional method of creating perovskite solar cells (PSCs) to be labor-intensive. We reasoned that the fabrication time may be reduced without sacrificing device performance by reducing the annealing temperatures. We changed the annealing temperatures for compact TiO₂, mesoporous TiO₂, and TiCl₄ treatment for each layer in order to evaluate this. According to our experiments, compact TiO₂ performed well when the annealing temperatures were lowered. Our maximum power conversion efficiency (PCE), which is comparable to traditional devices, was 18.03%. Through process simplification and excellent performance





preservation, this study successfully optimized PSC manufacture. We have advanced perovskite solar cell technology and increased efficiency by using a more effective annealing strategy, which helps to create more sustainable energy production ways.

6.3. Scope for Future Work

Reported Self-Assembling Molecules

Various self-assembling molecules have been explored for enhancing perovskite solar cells (PSCs). Amphiphilic block copolymers like PEG-b-P4VP and P3HT-b-PEG can self-assemble at the perovskite surface, passivating defects and improving film morphology, leading to better stability and charge transport. Fullerene derivatives such as PCBM and ICBA are notable for their ability to self-assemble at the interface of the perovskite and electron transport layers, enhancing charge extraction and reducing recombination losses. Small molecules like Spiro-OMeTAD and 2D materials such as hexagonal boron nitride also show promise, with their self-assembling properties contributing to improved hole transport and stability. Additionally, self-assembling monolayers (SAMs) formed by alkylphosphonic acids and carboxylic acid-terminated molecules can modify surface energy and morphology, leading to higher-quality films. Peptide-based molecules, including peptide amphiphiles, are being investigated for their ability to guide perovskite crystal growth, resulting in uniform and stable films.

Future Directions

The future of self-assembling molecules in PSCs lies in innovative molecular designs and hybrid structures. Developing molecules with tailored functional groups for specific interactions with perovskite components can enhance defect passivation and stability. Multifunctional molecules that integrate passivation, charge transport, and light absorption capabilities could simplify device architectures. Hybrid structures combining organic self-assembling molecules with inorganic nanomaterials are expected to offer superior properties. Scalable manufacturing techniques, such as roll-to-roll processing and inkjet printing, are crucial for cost-effective production. Enhancing environmental and mechanical stability through the design of protective self-assembling molecules will further improve the commercial viability of PSCs. Computational approaches, including machine learning and molecular dynamics simulations, are instrumental in predicting and screening new self-assembling molecules, guiding the development of advanced materials for high-performance PSCs.





Additional Self-Assembling Molecules for Future Research

In addition to the molecules already explored, several other self-assembling molecules hold promise for future research in PSCs. Metal-organic frameworks (MOFs) are a versatile class of materials that can be engineered to self-assemble into porous structures, potentially enhancing light harvesting and charge transport. Conjugated polyelectrolytes (CPEs) can form self-assembled films with high conductivity and tunable electronic properties, making them attractive for both electron and hole transport layers. Dendrimers, with their highly branched and tunable structures, can self-assemble into nanoscale architectures that enhance charge mobility and reduce recombination.

Another promising direction involves the use of supramolecular polymers, which can form highly ordered structures through non-covalent interactions, offering excellent control over film morphology and interfacial properties. Liquid crystals, which can self-align into ordered phases, might be used to create highly anisotropic films with superior charge transport properties. Lastly, incorporating bio-inspired molecules, such as DNA or protein-based structures, could lead to novel self-assembly mechanisms and functionalities, leveraging the precise molecular recognition and binding capabilities inherent in biological systems.

Exploring these additional classes of self-assembling molecules could open new avenues for enhancing the efficiency, stability, and manufacturability of PSCs, pushing the boundaries of current photovoltaic technology.

Single Crystalline Perovskite Thin Films in Future Directions

Single crystalline perovskite thin films represent a promising direction for the next generation of perovskite solar cells (PSCs). Unlike polycrystalline films, single crystalline perovskite films have fewer grain boundaries, resulting in reduced defect densities and higher carrier mobilities. These characteristics can significantly improve the efficiency of PSCs by enhancing charge transport and reducing recombination losses. Furthermore, single crystalline films typically exhibit better environmental stability due to the absence of grain boundaries that often serve as pathways for moisture and oxygen ingress.

The future development of single crystalline perovskite thin films will likely focus on scalable and reproducible fabrication techniques. Methods such as solution growth, vapor deposition, and space-confined growth are being explored to produce high-quality single crystalline films.





Innovations in these techniques will be essential to make the process compatible with large-scale manufacturing. Additionally, the integration of single crystalline films with flexible substrates could lead to the development of flexible and lightweight PSCs, broadening their application in portable and wearable electronics.

Another exciting direction is the use of single crystalline perovskite films in tandem solar cells. Their superior optical and electronic properties make them ideal candidates for the top cell in tandem configurations, potentially achieving efficiencies beyond the Shockley-Queisser limit. Combining single crystalline perovskite films with other high-efficiency materials, such as silicon or CIGS, could lead to highly efficient, commercially viable tandem solar cells. As research progresses, addressing challenges such as large-area fabrication, long-term stability, and cost-effectiveness will be crucial for the widespread adoption of single crystalline perovskite thin films in PSCs.





Appendix



Chapter-3

Table: S1 (Continuous irradiation data)

	Ref	EDTA	Ref	EDTA
T'()				
Time(sec)	PCE (%)	PCE (%)	J _{sc} (mA/cm²)	J _{sc} (mA/cm²)
20	17.6869	18.8574	23.27996	23.96288
40	17.8284	18.8714	23.273	23.97251
60	17.7899	18.8525	23.23918	23.96035
80	17.7995	18.7732	23.229	23.96314
100	17.8178	18.8436	23.20255	23.95204
120	17.821	18.8337	23.19612	23.9514
140	17.8151	18.8224	23.16592	23.95498
160	17.8229	18.8316	23.15463	23.95558
180	17.8505	18.8318	23.12938	23.96203
200	17.7405	18.8477	23.12716	23.93856
220	17.7502	18.8029	23.11158	23.94262
240	17.694	18.8786	23.10551	23.95344
260	17.7461	19.0539	23.08132	23.95379
280	17.7558	19.0296	23.12778	23.95295
300	17.6449	18.9673	23.0843	23.93992
320	17.6921	19.0253	23.07236	23.94565
340	17.785	19.0222	23.04728	23.93135
360	17.8789	19.0176	23.01777	23.93703
380	17.8797	18.9944	23.00768	23.91771
400	17.8558	19	22.97456	23.9284
420	17.9349	18.9964	22.9416	23.92911
440	17.9364	18.9853	22.91507	23.92187
460	17.8909	18.961	22.86669	23.92135
480	17.8932	19.1537	22.86125	23.93678
500	17.9398	18.9269	22.83968	23.93285
520	17.8047	18.9468	22.79952	23.91195
540	17.8742	18.9156	22.77033	23.91346
560	17.7417	18.9333	22.73886	23.90935
580	17.8371	18.9018	22.72442	23.90606
600	17.6753	18.893	22.70216	23.89836
620	17.6382	18.849	22.65633	23.91188
640	17.6515	18.8471	22.64152	23.90456
660	17.623	18.7938	22.63114	23.90641
680	17.6738	18.8534	22.60848	23.90916
700	17.338	18.7683	22.58234	23.89578
720	17.3383	18.9176	22.56542	23.89945
740	17.3289	19.0064	22.53839	23.90712
760	17.4433	18.8307	22.49037	23.89389
780	17.3397	18.7518	22.46946	23.88739
800	17.2988	18.7256	22.45536	23.91249
820	17.4334	18.7095	22.44892	23.89281
840	17.1167	18.6889	22.41464	23.89819
860	17.1774	18.7701	22.39164	23.91828
880	17.1491	18.6786	22.3819	23.89625
900	17.1599	18.7354	22.36507	23.89071
920	17.1913	18.6402	22.33287	23.89412
940	17.1076	18.6311	22.31686	23.8735
960	16.9443	18.6248	22.27855	23.88807
980	17.1002	18.6039	22.27497	23.8792
1000	16.9858	18.6029	22.26471	23.88204
1020	16.8452	18.587	22.24737	23.87691
1040	16.8133	18.5903	22.21867	23.87982
1060	16.84	18.5566	22.18248	23.86646
1080	16.786	18.5649	22.15187	23.87865
1100	16.7792	18.564	22.12063	23.88655
1120	16.7045	18.5637	22.10287	23.87347
1140	16.693	18.532	22.08134	23.8682
1160	16.6303	18.7507	22.06262	23.87742





1180	16.6061	18.5321	22.02358	23.87192
1200	16.6814	18.4979	22.00905	23.87542
1220	16.538	18.4794	21.97485	23.86353

Table: S2 (Reproducibility statistics)

	Ref		EDTA		
device count	Jsc mA/cm2	PCE(%)	Jsc mA/cm22	PCE(%)3	
1	25.91479	18.7169	23.09051	17.3271	
2	25.83043	18.9349	23.08276	17.2793	
3	25.77401	19.1041	23.06415	17.3659	
4	25.73813	19.2294	23.05868	17.3598	
5	25.6973	19.3876	23.04681	17.4651	
6	25.68027	19.5493	23.0442	17.6146	
7	25.66621	19.6677	23.03066	17.5589	
8	25.64191	19.7795	23.03803	17.696	
9	25.62267	19.8139	23.04111	17.4876	
10	25.5931	19.8612	23.03163	17.583	
11	25.57213	19.8411	21.93405	13.9914	
12	25.57179	19.8078	22.01432	15.1021	
13	25.55107	19.676	22.04639	15.5632	
14	25.53666	19.6212	22.0468	15.7188	
15	25.54834	19.6182	22.06204	15.8473	
16	24.61358	16.3755	22.03963	15.9615	
17	24.6805	17.3906	22.05712	16.14	
18	24.6832	17.6417	22.06713	16.1315	
19	24.67411	17.7185	22.04737	16.1784	
20	24.65923	17.8744	22.03958	16.1954	
21	24.64093	18.0304	22.04324	16.2291	
22	24.62647	18.0861	22.02951	16.2603	
23	24.64662	18.1145	22.02283	16.2648	
24	24.67781	18.1939	22.02504	16.3177	
25	24.75366	18.2163	22.02026	16.3509	
26	24.73735	18.3662	22.10639	15.1334	
27	24.66431	18.3411	22.05556	15.2853	
28	24.63467	18.3198	22.0211	15.3613	
29	24.62293	18.3992	22.04289	15.4479	
30	24.6071	18.1813	22.00464	15.4404	





Table: S3 (Stability data)

	EDTA		Ref	
Days	Jsc mA/cm2	PCE(%)	Jsc mA/cm22	PCE(%)3
1	25.64191	19.7795	23.03163	17.583
2	25.66621	19.6677	23.0442	17.6146
3	25.55107	19.676	23.03066	17.5589
4	25.53666	19.6212	23.04111	17.4876
5	25.54834	19.6182	23.04681	17.4651
6	25.68027	19.5493	23.05868	17.3598
7	25.6973	19.3876	23.06415	17.3659
8	25.73813	19.2294	23.09051	17.3271
9	25.77401	19.1041	23.08276	17.2793
10	24.98635	19.0626	23.00052	17.1774
15	24.96577	19.0729	22.83968	17.1076
20	24.93866	19.0463	22.63114	16.9858
25	24.92346	18.9379	22.39654	16.7792
30	24.73735	18.3662	22.02358	16.538
35	24.75366	18.2163	21.67526	16.2534
40	24.55072	18.256	21.34568	15.8563
45	24.48713	18.2151	21.00564	15.2349
50	24.40639	18.2075	20.61506	14.8815
55	24.00139	18.0666	20.54875	14.4619
60	23.62858	17.8142	20.34564	14.0256

Table: S4 (FTO/TiO₂/PVK/Au)

Temperature (°C)	Mobility (cm²/(V·sec))	V _{TFL} (V)	Trap density (cm ⁻³⁾	Conductance (S)	Conductivity (S/cm)	Charge Carrier Density (cm ⁻³⁾
rt	1.42634E-05	0.24	3.3984E+15	1.37E-04	4.2835E-08	1.87696E+16
35	5.35062E-07	0.15	2.124E+15	2.80E-06	8.73959E-10	1.02086E+16
45	4.45455E-08	0.29	4.1064E+15	4.37E-06	1.36602E-09	1.9166E+17
55	6.39505E-09	0.47	6.6552E+15	2.09E-07	6.53553E-11	6.38729E+16
65	7.06503E-10	0.71	1.00536E+16	5.35E-08	1.67043E-11	1.47772E+17
75	2.02962E-10	0.94	1.33104E+16	7.03E-09	2.19575E-12	6.76158E+16
85	1.26074E-10	1.7	2.4072E+16	2.20E-09	6.86881E-13	3.40516E+16

Table: S5 (FTO/TiO₂/EDTA/PVK/Au)

Temperature (°C)	Mobility (cm²/(V·sec))	V _{TFL} (V)	Trap density (cm ⁻³⁾	Conductance (S)	Conductivity (S/cm)	Charge Carrier Density (cm ⁻³⁾
rt	8.07113E-05	0.52	7.3632E+15	0.00388	1.2125E-06	9.38918E+16
35	7.27117E-05	0.24	4.3632E+15	0.00457	1.42813E-06	1.22756E+17
45	3.12834E-06	0.09	1.2744E+15	0.00696	0.000002175	4.34535E+18
55	0.000385562	0.29	4.1064E+15	0.00374	1.16875E-06	1.89456E+16
65	1.13166E-06	0.2	2.832E+15	0.00376	0.000001175	6.48939E+18
75	0.000714767	0.1	1.416E+15	1.45E-05	4.53056E-09	3.96158E+13
85	1.489E-07	0.79	1.11864E+16	2.17E-06	6.78069E-10	2.84616E+16





Chapter-4

Table: S6 (Continuous irradiation data)

	Ref	Gu	Ref	Gu
Time(sec)	PCE (%)	PCE (%)	Jsc (mA/cm2)	Jsc (mA/cm2)
20	17.6869	19.9509	23.27996	24.68893
40	17.8284	19.4264	23.273	24.70011
60	17.7899	19.7636	23.23918	24.70635
80	17.7995	19.8071	23.229	24.68778
100	17.8178	19.8552	23.20255	24.70354
120	17.821	19.9509	23.19612	24.68893
140	17.821	19.9246	23.16592	24.68754
160	17.8229	19.9203	23.15463	24.68166
180	17.8505	19.9169	23.12938	24.6877
200	17.7405	19.9102	23.12716	24.67825
220	17.7502	19.8803	23.11158	24.6889
240	17.694	19.3521	23.10551	24.53524
260	17.7461	19.3321	23.08132	24.53444
280	17.7558	19.2569	23.12778	24.53118
300	17.6449	19.2966	23.0843	24.53524
320	17.6921	19.2946	23.07236	23.80903
340	17.785	19.254	23.04728	23.81356
360	17.8789	19.2622	23.01777	23.82286
380	17.8797	19.2107	23.00768	23.80048
400	17.8558	18.8335	22.97456	23.81762
420	17.9349	19.1928	22.9416	23.81367
440	17.9364	19.1835	22.91507	23.79643
460	17.8909	19.079	22.86669	23.79469
480	17.8932	18.509	22.86125	23.78224
500	17.9398	18.6542	22.83968	23.77669
520	17.8047	18.8141	22.79952	23.77751
540	17.8742	18.8016	22.77033	23.7734
560	17.7417	18.8034	22.73886	23.6751
580	17.8371	18.7917	22.72442	23.68086
600	17.6753	18.8004	22.70216	23.67827
620	17.6382	18.7457	22.65633	23.68194
640	17.6515	18.7272	22.64152	23.67847
660	17.623	18.7427	22.63114	23.65615
680	17.6738	18.7674	22.60848	23.67165
700	17.338	18.757	22.58234	23.66035
720	17.3383	18.7302	22.56542	23.64211
740	17.3289	18.6147	22.53839	23.63504
760	17.4433	18.4348	22.49037	23.60726
780	17.3397	18.4931	22.46946	23.60901
800	17.2988	18.5522	22.45536	23.64542
820	17.4334	18.6387	22.44892	23.608
840	17.1167	18.6604	22.41464	23.6098
860	17.1774	18.6744	22.39164	23.24107
880	17.1491	18.6497	22.3819	23.24959
900	17.1599	18.5813	22.36507	23.25406
920	17.1913	18.6378	22.33287	23.24452
940	17.1076	18.6272	22.31686	23.25439
960	16.9443	18.5747	22.27855	23.26001
980	17.1002	18.5402	22.27497	23.25569
1000	16.9858	18.2473	22.26471	23.2607
1020	16.8452	18.2614	22.24737	23.25978
1040	16.8133	18.2079	22.21867	23.2658
1060	16.84	18.2292	22.18248	23.26899
1080	16.786	18.2371	22.15187	23.27553
1100	16.7792	18.2436	22.12063	23.30215
1120	16.7045	18.2458	22.10287	23.29959
1140	16.693	18.2435	22.08134	23.3127
1160	16.6303	18.228	22.06262	23.30285





1180	16.6061	18.2348	22.02358	23.31248
1200	16.6814	18.1703	22.00905	23.29692
1220	16.538	18.1692	21.97485	23.30336

Table: S7 (Reproducibility statistics)

	Ref		Gu		
device count	Jsc mA/cm2	PCE(%)	Jsc mA/cm2	PCE(%)	
1	23.09051	17.3271	19.9509	24.68893	
2	23.08276	17.2793	19.4264	24.70011	
3	23.06415	17.3659	19.7636	24.70635	
4	23.05868	17.3598	19.8071	24.68778	
5	23.04681	17.4651	19.8552	24.70354	
6	23.0442	17.6146	19.9509	24.68893	
7	23.03066	17.5589	19.9246	24.68754	
8	23.03803	17.696	19.9203	24.68166	
9	23.04111	17.4876	19.9169	24.6877	
10	23.03163	17.583	19.9102	24.67825	
11	21.93405	13.9914	19.8803	24.6889	
12	22.01432	15.1021	19.3521	24.53524	
13	22.04639	15.5632	19.3321	24.53444	
14	22.0468	15.7188	19.2569	24.53118	
15	22.06204	15.8473	19.2966	24.53118	
16	22.03963	15.9615	18.6378	23.24452	
17	22.05712	16.14	18.6272	23.25439	
18	22.06713	16.1315	18.5747	23.26001	
19	22.04737	16.1784	18.5402	23.25569	
20	22.03958	16.1954	18.2473	23.2607	
21	22.04324	16.2291	18.2614	23.25978	
22	22.02951	16.2603	18.2079	23.2658	
23	22.02283	16.2648	18.2292	23.26899	
24	22.02504	16.3177	18.2371	23.27553	
25	22.02026	16.3509	18.2436	23.30215	
26	22.10639	15.1334	18.2458	23.29959	
27	22.05556	15.2853	18.2435	23.3127	
28	22.0211	15.3613	18.228	23.30285	
29	22.04289	15.4479	18.2348	23.31248	
30	22.00464	15.4404	18.1703	23.29692	





Table: S8 (Stability data)

Ref		Gu	
Jsc mA/cm2	PCE(%)	Jsc mA/cm2	PCE(%)
23.03163	17.583	19.9509	24.68893
23.0442	17.6146	19.9246	24.68754
23.03066	17.5589	19.9203	24.68166
23.04111	17.4876	19.9169	24.6877
23.04681	17.4651	19.9102	24.67825
23.05868	17.3598	19.8803	24.6889
23.06415	17.3659	19.8552	24.70354
23.09051	17.3271	19.8071	24.68778
23.08276	17.2793	19.7636	24.70635
23.00052	17.1774	19.4264	24.70011
22.83968	17.1076	19.3521	24.53524
22.63114	16.9858	19.2107	23.80048
22.39654	16.7792	19.1835	23.79643
22.02358	16.538	19.079	23.79469
21.67526	16.2534	18.8141	23.77751
21.34568	15.8563	18.8004	23.67827
21.00564	15.2349	18.6147	23.63504
20.61506	14.8815	18.5747	23.26001
20.54875	14.4619	18.2473	23.2607
20.34564	14.0256	18.1703	23.09692
	Jsc mA/cm2 23.03163 23.0442 23.03066 23.04111 23.04681 23.05868 23.06415 23.09051 23.08276 23.00052 22.83968 22.63114 22.39654 22.02358 21.67526 21.34568 21.00564 20.61506 20.54875	Jsc mA/cm2 PCE(%) 23.03163 17.583 23.0442 17.6146 23.03066 17.5589 23.04111 17.4876 23.04681 17.4651 23.05868 17.3598 23.06415 17.3659 23.09051 17.3271 23.08276 17.2793 23.00052 17.1774 22.83968 17.1076 22.63114 16.9858 22.02358 16.538 21.67526 16.2534 21.34568 15.8563 21.00564 15.2349 20.61506 14.8815 20.54875 14.4619	Jsc mA/cm2 PCE(%) Jsc mA/cm2 23.03163 17.583 19.9509 23.0442 17.6146 19.9246 23.03066 17.5589 19.9203 23.04111 17.4876 19.9169 23.04681 17.4651 19.9102 23.05868 17.3598 19.8803 23.06415 17.3659 19.8552 23.09051 17.3271 19.8071 23.08276 17.2793 19.7636 23.00052 17.1774 19.4264 22.83968 17.1076 19.3521 22.63114 16.9858 19.2107 22.39654 16.7792 19.1835 22.02358 16.538 19.079 21.67526 16.2534 18.8141 21.34568 15.8563 18.8004 21.00564 15.2349 18.6147 20.54875 14.4619 18.2473

Table: S9 (FTO/PVK/HTM/Au)

Temperature (°C)	Mobility (cm²/(V·sec))	V _{TFL} (V)	Trap density (cm ⁻³⁾	Conductance (S)	Conductivity (S/cm)	Charge Carrier Density (cm ⁻³⁾
rt	1.67801E-07	0.95	1.3452E+16	1.48E-06	4.62E-10	1.71988E+16
35	8.94446E-08	0.96	1.35936E+16	1.83E-06	5.73E-10	4.00069E+16
45	1.21544E-05	0.16	2.2656E+15	9.40E-05	2.94E-08	1.22E+17
55	0.000161847	0.44	6.2304E+15	6.83E-07	2.13E-10	8.23635E+16
65	2.67778E-05	0.5	7.08E+15	8.44E-06	2.64E-09	3.72E+16
75	4.28158E-06	0.23	3.2568E+15	0.00122	3.81E-07	5.56526E+17
85	1.43395E-06	0.58	8.2128E+15	9.31E-06	2.64E-10	1.22E+15

Table: S10 (FTO/PVK/GuSCN/HTM/Au)

Temperature (°C)	Mobility (cm²/(V·sec))	V _{TFL} (V)	Trap density (cm ⁻³⁾	Conductance (S)	Conductivity (S/cm)	Charge Carrier Density (cm ⁻³⁾
rt	1.56395E-08	0.25	3.54E+15	0.0026	8.125E-07	3.24698E+20
35	1.45937E-09	1.63	2.30808E+16	0.00479	1.49688E-06	6.41064E+17
45	9.92463E-09	0.25	1.2254E+15	2.24E-07	6.99134E-11	4.40277E+16
55	9.35932E-09	0.27	3.8232E+15	1.73E-07	5.40888E-11	3.61196E+16
65	6.3484E-09	0.63	8.9208E+15	2.13E-07	6.67172E-11	6.56831E+16
75	2.10957E-06	1.09	1.54344E+16	0.00192	0.0000006	1.77761E+18
85	3.23425E-10	1.24	1.75584E+16	0.00257	8.03125E-07	1.55199E+22





Chapter-5

Table: S11 (Continuous irradiation data)

	Type-A		Туре-В		Type-C	
Time(sec)	Jsc mA/cm2	PCE (%)	Jsc mA/cm2	PCE (%)	Jsc mA/cm2	PCE (%)
20	22.84881	16.2961	22.89759	17.2559	22.01978	16.0472
40	22.83045	16.3319	22.88467	17.2691	21.99917	16.4649
60	22.81759	16.1701	22.89592	17.279	21.95916	16.5239
80	22.80071	16.1464	22.89549	17.1101	21.93888	16.6047
100	22.79272	16.1733	22.89681	16.9515	21.94357	16.6591
120	22.793	16.3112	22.89286	16.7573	21.91974	16.7689
140	22.78814	16.3203	22.87864	16.7759	21.89792	16.6741
160	22.78766	16.342	22.88228	17.063	21.86651	16.5904
180	22.81775	16.373	22.87302	18.3986	21.82445	16.5563
200	22.80812	16.4086	22.89504	17.9184	21.78505	16.3897
220	22.81436	16.7096	22.89996	18.2976	21.75182	16.617
240	22.80351	16.6129	22.90158	18.5393	21.7336	16.6638
260	22.78767	16.6816	22.90374	18.0435	21.70317	16.6101
280	22.81704	16.6663	22.88191	17.9624	21.67208	16.4557
300	22.81909	16.6952	22.87727	17.8794	21.35909	15.8618
320	22.79548	16.6991	22.87986	17.8669	21.15211	15.3088
340	22.79067	16.6567	22.8819	17.8063	21.07887	15.1361
360	22.79449	16.6754	22.86467	17.7926	21.01779	15.0037
380	22.80333			17.8308	20.99481	14.8825
400		16.6763	22.87572		20.99481	
	22.78602	16.6842		17.7696		14.7671
420	22.79617	16.654	22.87023	17.7963	20.91458	14.6867
440	22.79016	16.6564	22.89082	17.7701	20.87154	14.561
460	22.789	16.636	22.89356	17.8113	20.83328	14.4902
480	22.80249	16.6522	22.88926	17.7609	20.78915	14.3916
500	22.80563	16.6201	22.88871	17.8201	20.74428	14.2847
520	22.80067	16.6164	22.87651	17.77	20.69653	14.2236
540	22.80736	16.6032	22.87825	17.7884	20.66722	14.131
560	22.80084	16.5754	22.90725	17.8153	20.61001	14.0686
580	22.7947	16.5803	22.89455	17.7812	20.58443	14.0538
600	22.80531	16.547	22.88072	17.7652	20.5442	13.9058
620	22.80478	16.5286	22.88153	17.7569	20.49533	13.8228
640	22.79964	16.5179	22.89395	17.6658	20.45061	13.7426
660	22.80015	16.4978	22.89728	17.5823	20.38665	13.665
680	22.80596	16.4934	22.91191	17.7234	20.35844	13.5919
700	22.81133	16.4864	22.90419	17.5647	20.3114	13.4897
720	22.81896	16.4459	22.89445	17.7118	20.27642	13.3953
740	22.8231	16.4413	22.91605	17.5382	20.21177	13.2925
760	22.82082	16.636	22.89356	17.5441	20.17518	13.1784
780	22.80902	16.6522	22.88926	17.4689	20.12352	13.0676
800	22.80384	16.6201	22.88871	17.5046	20.08196	12.9392
820	22.80971	16.6164	22.87651	17.4495	20.04251	12.8768
840	22.79978	16.6032	22.87825	17.4643	19.9836	12.7183
860	22.79934	16.5754	22.90725	17.3841	19.92995	12.6595
880	22.8012	16.5803	22.89455	17.4046	19.88338	12.504
900	22.79849	16.547	22.88072	17.3347	19.81801	12.4115
920	22.80172	16.5286	22.88153	17.3112	19.75807	12.3128
940	22.80399	16.5179	22.89395	17.2965	19.6907	12.1942
960	22.84623	16.4978	22.89333	17.421	19.62267	12.1353
980		16.4978				
	22.83256		22.91191	17.4269	19.56352	12.0647
1000	22.82912	16.4864	22.90419	17.6206	19.4929	11.9247
1020	22.81655	16.4459	22.89445	17.5102	19.41252	11.8667
1040	22.81772	16.4413	22.91605	17.4981	19.3619	11.7366
1060	22.81932	16.0784	22.89077	17.5901	19.26802	11.6331
1080	22.82291	16.0129	22.89048	18.1199	19.20566	11.5283
1100	22.81327	16.0425	22.8826	17.6234	19.13385	11.3843
1120	22.83387	15.972	22.87461	18.7848	19.0596	11.3034
		l	i	ĺ	Ī	Ī





1160	22.80628	15.9211	22.86787	17.6672	18.91338	11.0568
1180	22.80223	15.9316	22.85634	17.4475	18.832	10.9872
1200	22.80041	15.8398	22.86116	17.2584	18.75745	10.9206
1220	22.77897	15.8603	22.84629	17.208	18.69393	10.8785
1240	22.77116	15.811	22.86221	17.0958	18.63262	10.7941
1260	22.77948	15.8184	22.87035	17.0805	18.56156	10.6853
1280	22.7913	15.7889	22.86658	16.9944	18.48225	10.5859
1300	22.79545	15.7661	22.8651	16.9983	18.39012	10.5205
1320	22.80055	15.7112	22.8847	16.9864	18.31129	10.4585
1340	22.80156	15.6948	22.86462	16.8933	18.2264	10.3256
1360	22.79388	15.6948	22.86462	16.8971	18.13987	10.1059

Table: S12 (Stability data)

	PCE (%)				
Time (h)	Type-A	Туре-В	Type-C		
24	16.3739	17.0448	16.0674		
48	16.3732	17.0121	15.8526		
72	16.3334	16.9092	15.8575		
96	16.329	16.8655	15.8286		
120	16.3477	16.8149	15.7713		
144	16.2928	16.7944	15.7558		
168	16.2715	16.7058	15.7321		
192	16.2005	16.4771	15.6691		
216	16.1082	16.2917	15.525		
240	15.8594	16.1759	15.3144		
264	15.6772	16.1756	15.2672		
288	15.4789	16.0251	15.1675		
312	15.3364	15.9697	15.0195		
336	15.1941	15.8163	14.924		
360	15.1386	15.6306	14.7883		
384	15.0694	15.6689	14.3789		
408	15.0617	15.7215	14.3378		
432	15.0271	15.667	14.3039		
456	14.5696	15.6281	14.2601		
480	14.4451	15.397	13.9397		
528	14.4213	15.2984	13.8272		
576	14.1674	15.0834	13.8166		
624	14.0048	14.9269	13.6938		
672	13.8001	14.6597	13.6672		
720	13.1359	14.5695	13.2292		





Table: S13 (Type-A)

Temperature (°C)	Mobility (cm²/(V·sec))	V _{TFL} (V)	Trap density (cm ⁻³⁾	Conductance (S)	Conductivity (S/cm)	Charge Carrier Density (cm ⁻³⁾
rt	1.10279E-06	0.24	3.3984E+15	0.00401	1.25313E-06	7.10199E+18
35	1.38231E-07	0.6	8.496E+15	7.44E-04	2.32513E-07	1.05129E+19
45	4.62588E-09	0.4	9.4586E+15	4.29E-07	1.34166E-10	1.8127E+17
55	0.039168605	0.31	2.426E+16	1.55E-04	4.84634E-08	7.73314E+12
65	4.60049E-07	0.22	3.1152E+15	4.35E-05	1.3602E-08	1.8479E+17
75	1.33624E-07	0.32	4.5312E+15	3.07E-05	9.59863E-09	4.48957E+17
85	8.00542E-07	0.75	5.386E+15	2.68E-05	8.37809E-09	6.54095E+16

Table: S14 (Type-B)

Temperature (°C)	Mobility (cm²/(V·sec))	V _{TFL} (V)	Trap density (cm ⁻³⁾	Conductance (S)	Conductivity (S/cm)	Charge Carrier Density (cm ⁻³⁾
rt	4.2622E-05	0.37	5.2392E+15	0.00127	3.96875E-07	5.81969E+16
35	2.04934E-06	0.29	4.1064E+15	8.03E-04	2.50838E-07	7.64997E+17
45	2.50943E-06	0.26	3.1152E+15	0.00245	7.65625E-07	1.90687E+18
55	3.83428E-06	0.31	4.3896E+15	4.47E-05	1.39772E-08	2.27833E+16
65	4.01934E-05	0.13	1.8408E+15	0.0067	2.09375E-06	3.25575E+17
75	0.000417652	0.16	2.2656E+15	0.0067	2.09375E-06	3.13322E+16
85	6.24963E-06	0.75	1.062E+16	1.88E-06	5.86178E-10	5.86213E+14

Table: S15 (Type-C)

Temperature (°C)	Mobility (cm²/(V·sec))	V _{TFL} (V)	Trap density (cm ⁻³⁾	Conductance (S)	Conductivity (S/cm)	Charge Carrier Density (cm ⁻³⁾
rt	6.20204E-05	0.48	6.7968E+15	0.00156	4.875E-07	4.9127E+16
35	9.93171E-05	0.23	3.2568E+15	0.00114	3.5625E-07	2.24187E+16
45	4.39414E-05	0.31	4.5236E+15	0.00464	0.00000145	2.0624E+17
55	3.83649E-07	0.25	3.54E+15	0.00845	2.64063E-06	4.30182E+19
65	1.27736E-06	0.1	1.416E+15	0.00216	0.000000675	3.3027E+18
75	4.65987E-07	0.23	3.2568E+15	0.00222	6.9375E-07	9.30484E+18
85	0.000458737	0.13	1 8408F+15	5 36F-05	1 67603F-08	2.28348F+14





Bibliography



References:

- (1) Gautam, N. K.; Kaushika, N. D. Reliability evaluation of solar photovoltaic arrays. *Solar Energy* **2002**, 72 (2), 129-141. DOI: https://doi.org/10.1016/S0038-092X(01)00085-8.
- (2) Messmer, C.; Goraya, B. S.; Nold, S.; Schulze, P. S.; Sittinger, V.; Schön, J.; Goldschmidt, J. C.; Bivour, M.; Glunz, S. W.; Hermle, M. The race for the best silicon bottom cell: Efficiency and cost evaluation of perovskite–silicon tandem solar cells. *Progress in Photovoltaics: Research and Applications* **2021**, *29* (7), 744-759.
- (3) Green, M. A.; Ho-Baillie, A.; Snaith, H. J. The emergence of perovskite solar cells. *Nature photonics* **2014**, *8* (7), 506-514.
- (4) Park, N.-G. Halide perovskite photovoltaics: History, progress, and perspectives. *MRS Bulletin* **2018**, 43 (7), 527-533.
- (5) Lee, S. W.; Bae, S.; Kim, D.; Lee, H. S. Historical analysis of high-efficiency, large-area solar cells: toward upscaling of perovskite solar cells. *Advanced Materials* **2020**, *32* (51), 2002202.
- (6) Chauhan, A. K.; Kumar, P.; Sharma, S. N. Perovskite solar cells: Past, present, and future. In *Photovoltaics Beyond Silicon*, Elsevier, 2024; pp 113-163.
- (7) Zhu, P.; Chen, C.; Dai, J.; Zhang, Y.; Mao, R.; Chen, S.; Huang, J.; Zhu, J. Toward the commercialization of perovskite solar modules. *Advanced Materials* **2024**, *36* (15), 2307357.
- (8) Saeed, A.; Wang, L.; Miao, Q. High-performance Perovskite-based Tandem Solar Cells: Recent Advancement, Challenges, and Steps Towards Industrialization. *Solar RRL*.
- (9) Li, F.; Lin, F. R.; Jen, A. K. Y. Current state and future perspectives of printable organic and perovskite solar cells. *Advanced Materials* **2024**, *36* (17), 2307161.
- (10) Ann, M. H.; Kim, J.; Kim, M.; Alosaimi, G.; Kim, D.; Ha, N. Y.; Seidel, J.; Park, N.; Yun, J. S.; Kim, J. H. Device design rules and operation principles of high-power perovskite solar cells for indoor applications.

 Nano Energy 2020, 68, 104321.
- (11) Roy, P.; Sinha, N. K.; Tiwari, S.; Khare, A. A review on perovskite solar cells: Evolution of architecture, fabrication techniques, commercialization issues and status. *Solar Energy* **2020**, *198*, 665-688.





- (12) Ren, M.; Qian, X.; Chen, Y.; Wang, T.; Zhao, Y. Potential lead toxicity and leakage issues on lead halide perovskite photovoltaics. *Journal of Hazardous Materials* **2022**, *426*, 127848.
- (13) Park, N. G. Research direction toward scalable, stable, and high efficiency perovskite solar cells. *Advanced Energy Materials* **2020**, *10* (13), 1903106.
- (14) Wu, M.; Haji Ladi, N.; Yi, Z.; Li, H.; Shen, Y.; Wang, M. Stability Issue of Perovskite Solar Cells under Real-World Operating Conditions. *Energy Technology* **2020**, *8* (4), 1900744.
- (15) Gao, Y.; Lin, R.; Xiao, K.; Luo, X.; Wen, J.; Yue, X.; Tan, H. Performance optimization of monolithic all-perovskite tandem solar cells under standard and real-world solar spectra. *Joule* **2022**, *6* (8), 1944-1963. (16) Teixeira, C. O.; Castro, D.; Andrade, L.; Mendes, A. Selection of the ultimate perovskite solar cell materials and fabrication processes towards its industrialization: A review. *Energy Science & Engineering*
- **2022**, *10* (4), 1478-1525.
- (17) Schileo, G.; Grancini, G. Lead or no lead? Availability, toxicity, sustainability and environmental impact of lead-free perovskite solar cells. *Journal of materials chemistry C* **2021**, *9* (1), 67-76.
- (18) Yan, L.; Huang, H.; Cui, P.; Du, S.; Lan, Z.; Yang, Y.; Qu, S.; Wang, X.; Zhang, Q.; Liu, B. Fabrication of perovskite solar cells in ambient air by blocking perovskite hydration with guanabenz acetate salt. *Nature Energy* **2023**, *8* (10), 1158-1167.
- (19) Adil Afroz, M.; Ghimire, N.; Reza, K. M.; Bahrami, B.; Bobba, R. S.; Gurung, A.; Chowdhury, A. H.; Iyer, P. K.; Qiao, Q. Thermal stability and performance enhancement of perovskite solar cells through oxalic acid-induced perovskite formation. *ACS Applied Energy Materials* **2020**, *3* (3), 2432-2439.
- (20) Zhu, X.; Lau, C. F. J.; Mo, K.; Cheng, S.; Xu, Y.; Li, R.; Wang, C.; Zheng, Q.; Liu, Y.; Wang, T. Inverted planar heterojunction perovskite solar cells with high ultraviolet stability. *Nano Energy* **2022**, *103*, 107849.
- (21) Zhang, Z.; Huang, Y.; Jin, J.; Jiang, Y.; Xu, Y.; Zhu, J.; Zhao, D. Mechanistic understanding of oxidation of tin-based perovskite solar cells and mitigation strategies. *Angewandte Chemie* **2023**, *135* (45), e202308093.





- (22) Zhang, Z.; Tian, X.; Wang, C.; Jin, J.; Jiang, Y.; Zhou, Q.; Zhu, J.; Xu, J.; He, R.; Huang, Y. Revealing superoxide-induced degradation in lead-free tin perovskite solar cells. *Energy & Environmental Science* **2022**, *15* (12), 5274-5283.
- (23) Zhu, W.; Wang, S.; Zhang, X.; Wang, A.; Wu, C.; Hao, F. Ion migration in organic–inorganic hybrid perovskite solar cells: current understanding and perspectives. *Small* **2022**, *18* (15), 2105783.
- (24) Yuan, G.; Xie, W.; Song, Q.; Ma, S.; Ma, Y.; Shi, C.; Xiao, M.; Pei, F.; Niu, X.; Zhang, Y. Inhibited crack development by compressive strain in perovskite solar cells with improved mechanical stability. *Advanced Materials* **2023**, *35* (17), 2211257.
- (25) Shao, S.; Loi, M. A. The role of the interfaces in perovskite solar cells. *Advanced Materials Interfaces* **2020**, *7* (1), 1901469.
- (26) Chi, W.; Banerjee, S. K. Stability improvement of perovskite solar cells by compositional and interfacial engineering. *Chemistry of Materials* **2021**, *33* (5), 1540-1570.
- (27) Zhang, B.; Wang, Z.; Huang, H.; Zhang, L.; Gu, M.; Cheng, Y.; Wu, K.; Zhou, J.; Zhang, J. Work function and band alignment of few-layer violet phosphorene. *Journal of materials chemistry A* **2020**, *8* (17), 8586-8592.
- (28) Cahen, D.; Kahn, A. Electron energetics at surfaces and interfaces: concepts and experiments. Advanced Materials **2003**, *15* (4), 271-277.
- (29) Hartnagel, P.; Kirchartz, T. Understanding the light-intensity dependence of the short-circuit current of organic solar cells. *Advanced theory and simulations* **2020**, *3* (10), 2000116.
- (30) Li, P.; Lu, Z.-H. Interface Engineering in Organic Electronics: Energy-Level Alignment and Charge Transport. *Small Science* **2021**, *1* (1), 2000015.
- (31) Shockley, W.; Queisser, H. Detailed balance limit of efficiency of p–n junction solar cells. In *Renewable energy*, Routledge, 2018; pp Vol2_35-Vol32_54.
- (32) Kagan, C. R.; Mitzi, D. B.; Dimitrakopoulos, C. D. Organic-inorganic hybrid materials as semiconducting channels in thin-film field-effect transistors. *Science* **1999**, *286* (5441), 945-947.





- (33) Wang, Z.; Ganose, A. M.; Niu, C.; Scanlon, D. O. Two-dimensional eclipsed arrangement hybrid perovskites for tunable energy level alignments and photovoltaics. *Journal of Materials Chemistry C* **2019**, *7* (17), 5139-5147.
- (34) Ishihara, T.; Takahashi, J.; Goto, T. Optical properties due to electronic transitions in twodimensional semiconductors (C n H 2 n+ 1 NH 3) 2 Pbl 4. *Physical review B* **1990**, *42* (17), 11099.
- (35) Voorhoeve, R.; Johnson Jr, D.; Remeika, J.; Gallagher, P. Perovskite Oxides: Materials Science in Catalysis: Perovskite oxides, long known in solid-state chemistry and physics,. find new applications in catalysis. *Science* **1977**, *195* (4281), 827-833.
- (36) Moniruddin, M.; Ilyassov, B.; Zhao, X.; Smith, E.; Serikov, T.; Ibrayev, N.; Asmatulu, R.; Nuraje, N. Recent progress on perovskite materials in photovoltaic and water splitting applications. *Materials Today Energy* **2018**, *7*, 246-259.
- (37) Veldhuis, S. A.; Boix, P. P.; Yantara, N.; Li, M.; Sum, T. C.; Mathews, N.; Mhaisalkar, S. G. Perovskite materials for light-emitting diodes and lasers. *Advanced materials* **2016**, *28* (32), 6804-6834.
- (38) Rose, G. Beschreibung einiger neuen Mineralien des Urals. *Annalen der Physik* **1839**, *124* (12), 551-573.
- (39) Poglitsch, A.; Weber, D. Dynamic disorder in methylammoniumtrihalogenoplumbates (II) observed by millimeter-wave spectroscopy. *The Journal of chemical physics* **1987**, *87* (11), 6373-6378.
- (40) Onoda-Yamamuro, N.; Yamamuro, O.; Matsuo, T.; Suga, H. pT phase relations of CH3NH3PbX3 (X= Cl, Br, I) crystals. *Journal of Physics and Chemistry of Solids* **1992**, *53* (2), 277-281.
- (41) Brivio, F.; Frost, J. M.; Skelton, J. M.; Jackson, A. J.; Weber, O. J.; Weller, M. T.; Goni, A. R.; Leguy, A. M.; Barnes, P. R.; Walsh, A. Lattice dynamics and vibrational spectra of the orthorhombic, tetragonal, and cubic phases of methylammonium lead iodide. *Physical Review B* **2015**, *92* (14), 144308.
- (42) Noel, N. K.; Stranks, S. D.; Abate, A.; Wehrenfennig, C.; Guarnera, S.; Haghighirad, A.-A.; Sadhanala, A.; Eperon, G. E.; Pathak, S. K.; Johnston, M. B. Lead-free organic–inorganic tin halide perovskites for photovoltaic applications. *Energy & Environmental Science* **2014**, *7* (9), 3061-3068.





- (43) Li, J.; Cao, H.-L.; Jiao, W.-B.; Wang, Q.; Wei, M.; Cantone, I.; Lü, J.; Abate, A. Biological impact of lead from halide perovskites reveals the risk of introducing a safe threshold. *Nature communications* **2020**, *11* (1), 310.
- (44) Nasti, G.; Abate, A. Tin halide perovskite (ASnX3) solar cells: a comprehensive guide toward the highest power conversion efficiency. *Advanced Energy Materials* **2020**, *10* (13), 1902467.
- (45) Unger, E.; Kegelmann, L.; Suchan, K.; Sörell, D.; Korte, L.; Albrecht, S. Roadmap and roadblocks for the band gap tunability of metal halide perovskites. *Journal of Materials Chemistry A* **2017**, *5* (23), 11401-11409.
- (46) Tao, S.; Schmidt, I.; Brocks, G.; Jiang, J.; Tranca, I.; Meerholz, K.; Olthof, S. Absolute energy level positions in tin-and lead-based halide perovskites. *Nature communications* **2019**, *10* (1), 2560.
- (47) Campbell, I. H.; Rubin, S.; Zawodzinski, T. A.; Kress, J. D.; Martin, R. L.; Smith, D.; Barashkov, N. N.; Ferraris, J. P. Controlling Schottky energy barriers in organic electronic devices using self-assembled monolayers. *Physical Review B* **1996**, *54* (20), R14321.
- (48) Vilan, A.; Cahen, D. Chemical modification of semiconductor surfaces for molecular electronics. *Chemical reviews* **2017**, *117* (5), 4624-4666.
- (49) Topping, J. On the mutual potential energy of a plane network of doublets. *Proceedings of the Royal Society of London. Series A, Containing Papers of a Mathematical and Physical Character* **1927**, *114* (766), 67-72.
- (50) Taucher, T. C.; Zojer, E. The potential of x-ray photoelectron spectroscopy for determining interface dipoles of self-assembled monolayers. *Applied Sciences* **2020**, *10* (17), 5735.
- (51) Chen, Q.; Mao, L.; Li, Y.; Kong, T.; Wu, N.; Ma, C.; Bai, S.; Jin, Y.; Wu, D.; Lu, W. Quantitative o perando visualization of the energy band depth profile in solar cells. *Nature communications* **2015**, *6* (1), 7745.
- (52) Yang, D.; Yang, R.; Wang, K.; Wu, C.; Zhu, X.; Feng, J.; Ren, X.; Fang, G.; Priya, S.; Liu, S. High efficiency planar-type perovskite solar cells with negligible hysteresis using EDTA-complexed SnO2. *Nature Communications* **2018**, *9* (1), 3239. DOI: 10.1038/s41467-018-05760-x.





- (53) Zhao, W.; Guo, P.; Wu, J.; Lin, D.; Jia, N.; Fang, Z.; Liu, C.; Ye, Q.; Zou, J.; Zhou, Y. TiO2 Electron Transport Layer with p—n Homojunctions for Efficient and Stable Perovskite Solar Cells. *Nano-Micro Letters* **2024**, *16* (1), 191.
- (54) Li, Q.; Wang, Z.; Ma, J.; Han, M.; Gao, P.; Cai, M.; Zhang, Y.; Song, Y.; Peng, S. Unveiling the surface-interface properties of perovskite crystals and pivotal regulation strategies. *Nano Research* **2024**, *17* (5), 3950-3981. DOI: 10.1007/s12274-023-6291-9.
- (55) Bakr, Z. H.; Wali, Q.; Fakharuddin, A.; Schmidt-Mende, L.; Brown, T. M.; Jose, R. Advances in hole transport materials engineering for stable and efficient perovskite solar cells. *Nano energy* **2017**, *34*, 271-305.
- (56) Burschka, J.; Pellet, N.; Moon, S.-J.; Humphry-Baker, R.; Gao, P.; Nazeeruddin, M. K.; Grätzel, M. Sequential deposition as a route to high-performance perovskite-sensitized solar cells. *Nature* **2013**, *499* (7458), 316-319.
- (57) Yang, M.; Tian, T.; Fang, Y.; Li, W.-G.; Liu, G.; Feng, W.; Xu, M.; Wu, W.-Q. Reducing lead toxicity of perovskite solar cells with a built-in supramolecular complex. *Nature Sustainability* **2023**, *6* (11), 1455-1464.
- (58) Babayigit, A.; Duy Thanh, D.; Ethirajan, A.; Manca, J.; Muller, M.; Boyen, H.-G.; Conings, B. Assessing the toxicity of Pb-and Sn-based perovskite solar cells in model organism Danio rerio. *Scientific reports* **2016**, *6* (1), 18721.
- (59) Okorieimoh, C. C. Long-Term Durability of Rooftop Grid-Connected Solar Photovoltaic Systems. **2022**.
- (60) Ogbomo, O. O. Optimised solder interconnections in crystalline silicon (c-Si) photovoltaic modules for improved performance in elevated temperature climate. **2020**.
- (61) Flora, G.; Gupta, D.; Tiwari, A. Toxicity of lead: a review with recent updates. *Interdisciplinary toxicology* **2012**, *5* (2), 47-58.





- (62) Chen, C. H.; Cheng, S. N.; Hu, F.; Su, Z. H.; Wang, K. L.; Cheng, L.; Chen, J.; Shi, Y. R.; Xia, Y.; Teng, T. Y. Lead Isolation and Capture in Perovskite Photovoltaics toward Eco-Friendly Commercialization.

 Advanced Materials 2024, 2403038.
- (63) Wang, Z.; Zhu, X.; Feng, J.; Wang, C.; Zhang, C.; Ren, X.; Priya, S.; Liu, S.; Yang, D. Antisolvent-and Annealing-Free Deposition for Highly Stable Efficient Perovskite Solar Cells via Modified ZnO. *Advanced Science* **2021**, *8* (13), 2002860.
- (64) Marques, N.; Jana, S.; Mendes, M. J.; Águas, H.; Martins, R.; Panigrahi, S. Surface modification of halide perovskite using EDTA-complexed SnO 2 as electron transport layer in high performance solar cells. *RSC advances* **2024**, *14* (18), 12397-12406.
- (65) Wu, R.; Meng, J.; Shi, Y.; Xia, Z.; Yan, C.; Zhang, L.; Liu, W.; Zhao, J.; Deng, J.; Zhang, X. Multifunctional buried interface modification for efficient and stable SnO 2-based perovskite solar cells. *Journal of Materials Chemistry A* **2024**, *12* (21), 12672-12680.
- (66) Geng, Q.; Zhang, S.; Sui, H.; Liu, X.; Li, Y.; Zhong, H.; Yao, C.; Zhang, Q.; Chu, X. Natural Chelating Agent-Treated Electron Transfer Layer for Friendly Environmental and Efficient Perovskite Solar Cells. *ACS Applied Materials & Interfaces* **2024**.
- (67) Patil, P.; Maibam, A.; Sangale, S. S.; Mann, D. S.; Lee, H.-J.; Krishnamurty, S.; Kwon, S.-N.; Na, S.-I. Chemical bridge-mediated heterojunction electron transport layers enable efficient and stable perovskite solar cells. *ACS Applied Materials & Interfaces* **2023**, *15* (24), 29597-29608.
- (68) Wu, J.; Zhang, N.; Sun, J.; Yang, W.; Sha, X.; Zhang, L.; Long, H.; Ying, Z.; Yang, X.; Liu, S. Molecule-Assisted Chemical Bath Deposition of Tin Oxide Electron Transport Layers in Perovskite Solar Cells. *physica status solidi* (a) **2023**, 220 (14), 2200897.
- (69) Ku, Z.; Rong, Y.; Xu, M.; Liu, T.; Han, H. Full Printable Processed Mesoscopic CH3NH3Pbl3/TiO2 Heterojunction Solar Cells with Carbon Counter Electrode. *Scientific Reports* **2013**, *3* (1), 3132. DOI: 10.1038/srep03132.





- (70) Rong, Y.; Ku, Z.; Mei, A.; Liu, T.; Xu, M.; Ko, S.; Li, X.; Han, H. Hole-Conductor-Free Mesoscopic TiO2/CH3NH3Pbl3 Heterojunction Solar Cells Based on Anatase Nanosheets and Carbon Counter Electrodes. *The Journal of Physical Chemistry Letters* **2014**, *5* (12), 2160-2164. DOI: 10.1021/jz500833z. (71) Bach, U.; Lupo, D.; Comte, P.; Moser, J.-E.; Weissörtel, F.; Salbeck, J.; Spreitzer, H.; Grätzel, M. Solidstate dye-sensitized mesoporous TiO2 solar cells with high photon-to-electron conversion efficiencies. *Nature* **1998**, *395* (6702), 583-585.
- (72) Alotaibi, M. H.; Alzahrani, Y. A.; Arora, N.; Alyamani, A.; Albadri, A.; Albrithen, H.; Al-Lehyani, I. H.; Alenzi, S. M.; Alanzi, A. Z.; Alghamdi, F. S. Halide versus nonhalide salts: the effects of guanidinium salts on the structural, morphological, and photovoltaic performances of perovskite solar cells. *Solar Rrl* **2020**, *4* (2), 1900234.
- (73) Teale, S.; Degani, M.; Chen, B.; Sargent, E. H.; Grancini, G. Molecular cation and low-dimensional perovskite surface passivation in perovskite solar cells. *Nature Energy* **2024**, 1-14.
- (74) Castro-Méndez, A. F.; Hidalgo, J.; Correa-Baena, J. P. The role of grain boundaries in perovskite solar cells. *Advanced Energy Materials* **2019**, *9* (38), 1901489.
- (75) Ochoa-Martinez, E.; Ochoa, M.; Ortuso, R. D.; Ferdowsi, P.; Carron, R.; Tiwari, A. N.; Steiner, U.; Saliba, M. Physical passivation of grain boundaries and defects in perovskite solar cells by an isolating thin polymer. *ACS Energy Letters* **2021**, *6* (7), 2626-2634.
- (76) Phung, N.; Al-Ashouri, A.; Meloni, S.; Mattoni, A.; Albrecht, S.; Unger, E. L.; Merdasa, A.; Abate, A. The role of grain boundaries on ionic defect migration in metal halide perovskites. *Advanced Energy Materials* **2020**, *10* (20), 1903735.
- (77) Hou, X.; Hu, Y.; Liu, H.; Mei, A.; Li, X.; Duan, M.; Zhang, G.; Rong, Y.; Han, H. Effect of guanidinium on mesoscopic perovskite solar cells. *Journal of Materials Chemistry A* **2017**, *5* (1), 73-78.
- (78) Nishimura, N.; Kanda, H.; Katoh, R.; Kogo, A.; Murakami, T. N. Thermally stable phenylethylammonium-based perovskite passivation: spontaneous passivation with phenylethylammonium bis (trifluoromethylsulfonyl) imide during deposition of PTAA for enhancing photovoltaic performance of perovskite solar cells. *Journal of Materials Chemistry A* **2024**.





- (79) Zhang, Y.; Jang, S.; Hwang, I.-W.; Jung, Y. K.; Lee, B. R.; Kim, J. H.; Kim, K. H.; Park, S. H. Bilateral interface engineering for efficient and stable perovskite solar cells using phenylethylammonium iodide. *ACS applied materials & interfaces* **2020**, *12* (22), 24827-24836.
- (80) Cheng, H.; Feng, Y.; Fu, Y.; Zheng, Y.; Shao, Y.; Bai, Y. Understanding and minimizing non-radiative recombination losses in perovskite light-emitting diodes. *Journal of Materials Chemistry C* **2022**, *10* (37), 13590-13610.
- (81) Wu, G.; Yang, T.; Li, X.; Ahmad, N.; Zhang, X.; Yue, S.; Zhou, J.; Li, Y.; Wang, H.; Shi, X. Molecular engineering for two-dimensional perovskites with photovoltaic efficiency exceeding 18%. *Matter* **2021**, *4* (2), 582-599.
- (82) Wang, Q.; Xu, Y.; Zhang, L.; Yang, A.; Bai, T.; Liu, F.; Lyu, M.; Zhu, J. Guanidinium thiocyanate additive engineering for high-performance CsPbIBr2 solar cells with an efficiency of 10.90%. *ACS Applied Energy Materials* **2022**, *5* (3), 3110-3118.
- (83) Zhong, Y.; Yang, J.; Wang, X.; Liu, Y.; Cai, Q.; Tan, L.; Chen, Y. Inhibition of ion migration for highly efficient and stable perovskite solar cells. *Advanced Materials* **2023**, *35* (52), 2302552.
- (84) Lin, Q.; Kubicki, D. J.; Omrani, M.; Alam, F.; Abdi-Jalebi, M. The race between complicated multiple cation/anion compositions and stabilization of FAPbI 3 for halide perovskite solar cells. *Journal of Materials Chemistry C* **2023**, *11* (7), 2449-2468.
- (85) Mali, S. S.; Patil, J. V.; Shao, J.-Y.; Zhong, Y.-W.; Rondiya, S. R.; Dzade, N. Y.; Hong, C. K. Phase-heterojunction all-inorganic perovskite solar cells surpassing 21.5% efficiency. *Nature Energy* **2023**, *8* (9), 989-1001. DOI: 10.1038/s41560-023-01310-y.
- (86) Zou, J.; Liu, W.; Deng, W.; Lei, G.; Zeng, S.; Xiong, J.; Gu, H.; Hu, Z.; Wang, X.; Li, J. An efficient guanidinium isothiocyanate additive for improving the photovoltaic performances and thermal stability of perovskite solar cells. *Electrochimica Acta* **2018**, *291*, 297-303.
- (87) Yang, L.; Xiao, Y.; Han, G.; Chang, Y.; Zhang, Y.; Li, Y.; Hou, W.; Su, L.; Li, H. Synergistic effect of guanidine thiocyanate additive and dimethyl sulfoxide post-treatment towards efficient and stable perovskite solar cell. *Thin Solid Films* **2019**, *689*, 137495.





- (88) Cheng, N.; Li, W.; Zhang, M.; Wu, H.; Sun, S.; Zhao, Z.; Xiao, Z.; Sun, Z.; Zi, W.; Fang, L. Enhance the performance and stability of methylammonium lead iodide perovskite solar cells with guanidinium thiocyanate additive. *Current Applied Physics* **2019**, *19* (1), 25-30.
- (89) Zhang, Y.; Chen, J.; Lian, X.; Qin, M.; Li, J.; Andersen, T. R.; Lu, X.; Wu, G.; Li, H.; Chen, H. Highly efficient guanidinium-based quasi 2D perovskite solar cells via a two-step post-treatment process. *Small Methods* **2019**, *3* (11), 1900375.
- (90) Agarwala, P.; Kabra, D. A review on triphenylamine (TPA) based organic hole transport materials (HTMs) for dye sensitized solar cells (DSSCs) and perovskite solar cells (PSCs): evolution and molecular engineering. *Journal of Materials Chemistry A* **2017**, *5* (4), 1348-1373.
- (91) Reddy, N. P.; Santhosh, R.; Thogiti, S.; Muniramaiah, R.; Joseph, D. P.; Murali, B. Nanostructured ternary perovskite oxides as photoconversion efficiency enhancers for DSSC. *Journal of Materials Chemistry C* **2022**, *10* (4), 1403-1413, 10.1039/D1TC04584A. DOI: 10.1039/D1TC04584A.
- (92) Alsalloum, A. Y.; Turedi, B.; Zheng, X.; Mitra, S.; Zhumekenov, A. A.; Lee, K. J.; Maity, P.; Gereige, I.; AlSaggaf, A.; Roqan, I. S.; et al. Low-Temperature Crystallization Enables 21.9% Efficient Single-Crystal MAPbI3 Inverted Perovskite Solar Cells. *ACS Energy Letters* **2020**, *5* (2), 657-662. DOI: 10.1021/acsenergylett.9b02787.
- (93) Liu, T.; Liu, L.; Hu, M.; Yang, Y.; Zhang, L.; Mei, A.; Han, H. Critical parameters in TiO2/ZrO2/Carbon-based mesoscopic perovskite solar cell. *Journal of Power Sources* **2015**, *293*, 533-538. DOI: https://doi.org/10.1016/j.jpowsour.2015.05.106.
- (94) Wang, Q.; Liu, S.; Ming, Y.; Guan, Y.; Li, D.; Zhang, C.; Wang, Z.; Rong, Y.; Hu, Y.; Han, H. Improvements in printable mesoscopic perovskite solar cells via thinner spacer layers. *Sustainable Energy & Fuels* **2018**, *2* (11), 2412-2418, 10.1039/C8SE00332G. DOI: 10.1039/C8SE00332G.
- (95) Chen, M.; Fu, W.; Shi, M.; Hu, X.; Pan, J.; Ling, J.; Li, H.; Chen, H. An ester-functionalized diketopyrrolopyrrole molecule with appropriate energy levels for application in solution-processed organic solar cells. *Journal of Materials Chemistry A* **2013**, *1* (1), 105-111.





- (96) Kranthiraja, K.; Arivunithi, V. M.; Aryal, U. K.; Park, H.-Y.; Cho, W.; Kim, J.; Reddy, S. S.; Kim, H.-K.; Kang, I.-N.; Song, M.; et al. Efficient and hysteresis-less perovskite and organic solar cells by employing donor-acceptor type π -conjugated polymer. *Organic Electronics* **2019**, *72*, 18-24. DOI: https://doi.org/10.1016/j.orgel.2019.05.044.
- (97) Karuthedath, S.; Paleti, S. H.; Sharma, A.; Yin, H.; P. De Castro, C. S.; Chen, S.; Xu, H.; Alshehri, N.; Ramos, N.; Khan, J. I. Rationalizing the Influence of Tunable Energy Levels on Quantum Efficiency to Design Optimal Non-Fullerene Acceptor-Based Ternary Organic Solar Cells. *Advanced Energy Materials* **2023**, 2203464.
- (98) Zhang, X.; Yao, T.; Wang, Y.; Li, Z.; Yin, J.; Wang, H.; Jiang, W.; Liu, S.; Cui, Y.; Ding, W. Preliminary exploration of the influence of N+/NHx+ ions/groups bombardment at TiO2 ETLs on performance of MAPbI3 perovskite solar cells. *Applied Surface Science* **2024**, *645*, 158727.
- (99) Baqandwan, H.; Samsuri, S. A. M.; Halim, M. M.; Pakhuruddin, M. Z. Nanostructured TiO2 thin films sputtered at room temperature as electron transport layer for flexible perovskite solar cell applications: Impact of varying RF power. *Physica B: Condensed Matter* **2024**, *679*, 415788.
- (100) Wu, S.; Li, C.; Lien, S. Y.; Gao, P. Temperature Matters: Enhancing Performance and Stability of Perovskite Solar Cells through Advanced Annealing Methods. *Chemistry* **2024**, *6* (1), 207-236.
- (101) Elumalai, T. R.; Ramasamy, E.; Mallick, S.; Rao, T.; Veerappan, G. Low-temperature curable TiO 2 sol for separator and HTM-free carbon-based perovskite solar cells. *Materials Advances* **2024**, *5* (2), 539-548.
- (102) Wang, J.; Dong, Z.; Wang, J.; Zhang, J.; Zhai, Z.; Qiu, F.; Wu, J.; Lin, Y.; Zhang, J. Room-temperature processed TiO 2 to construct composite electron transport layers for efficient planar perovskite solar cells. *Journal of Materials Chemistry A* **2023**, *11* (41), 22206-22215.
- (103) Yoo, Y.; Seo, G.; Park, H. J.; Kim, J.; Jang, J.; Cho, W.; Kim, J. H.; Shin, J.; Choi, J. S.; Lee, D. Low-temperature rapid UV sintering of sputtered TiO 2 for flexible perovskite solar modules. *Journal of Materials Chemistry A* **2024**, *12* (3), 1562-1572.





(104) Chen, K.-T.; Hsu, C.-H.; Jiang, S.-C.; Liang, L.-S.; Gao, P.; Qiu, Y.; Wu, W.-Y.; Zhang, S.; Zhu, W.-Z.; Lien, S.-Y. Effect of annealing temperature on tantalum-doped TiO 2 as electron transport layer in Perovskite solar cells. *IEEE Transactions on Electron Devices* **2022**, *69* (3), 1149-1154.

(105) Kemat, R.; Sahari, S. K.; Baharin, A. The effects of annealing temperature dependence on the doping of titanium dioxide (TiO2) and reduced graphene oxide (RGO) for perovskite solar cell application. *International Journal of Nanoelectronics and Materials* **2020**, *13*.

(106) Passatorntaschakorn, W.; Khampa, W.; Musikpan, W.; Ngamjarurojana, A.; Gardchareon, A.; Ruankham, P.; Bhoomanee, C.; Wongratanaphisan, D. Low-Temperature TiO2 Electron Transporting Layer for Planar Hole Transport Material-Free Carbon Electrode-CsFA-Based Perovskite Solar Cells. *physica status solidi (a)* **2024**, 2400470.

(107) Zhen, C.; Wu, T.; Chen, R.; Wang, L.; Liu, G.; Cheng, H.-M. Strategies for modifying TiO2 based electron transport layers to boost perovskite solar cells. *Acs Sustainable Chemistry & Engineering* **2019**, 7 (5), 4586-4618.





Publications and Presentations



List of Publications & Presentations

- 14. Santhosh, R.; Ketavath, R.; Murali, B. Unadorned Molecular Engineering of Phenoxazine-Core-Based Hole-Transport Materials for Sustainable Perovskite Solar Cells. ACS Applied Energy Materials 2023, 6 (17), 9001-9011.
- 15. Muniramaiah, R.; Reddy, N. P.; Santhosh, R.; Maharana, G.; Fernandes, J. M.; Padmanaban, D. B.; Kovendhan, M.; Veerappan, G.; Laxminarayana, G.; Banavoth, M.; et al. Anionic Fluorine and Cationic Niobium Codoped Tin Oxide Thin Films as Transparent Conducting Electrodes for Optoelectronic Applications. *physica status solidi* (a) 2023, 220 (14), 2200703.
- 16. Muniramaiah, R.; Reddy, N. P.; Santhosh, R.; Fernandes, J. M.; Padmanaban, D. B.; Maharana, G.; Kovendhan, M.; Veerappan, G.; Laxminarayana, G.; Banavoth, M.; et al. Solvent effect on the optoelectronic properties of fluorine doped SnO2 thin films prepared by spray-pyrolysis. *Surfaces and Interfaces* 2022, 33, 102174.
- 17. Purushotham Reddy, N.; Santhosh, R.; Fernandes, J. M.; Muniramaiah, R.; Murali, B.; Paul Joseph, D. Nanocrystalline Sb-doped-BaSnO3 perovskite electron transport layer for dye-sensitized solar cells. *Materials Letters* 2022, 311, 131629.
- 18. Reddy, N. P.; Muniramaiah, R.; Santhosh, R.; Fernandes, J. M.; Padmanaban, D. B.; Maharana, G.; Kovendhan, M.; Paul Joseph, D.; Murali, B. Cost-effective Sb-doped SnO2 films as stable and efficient alternative transparent conducting electrodes for dyesensitized solar cells. *Journal of Materials Chemistry C* 2022, 10 (20), 7997-8008.
- 19. Reddy, N. P.; Santhosh, R.; Thogiti, S.; Muniramaiah, R.; Joseph, D. P.; Murali, B. Nanostructured ternary perovskite oxides as photoconversion efficiency enhancers for DSSC. *Journal of Materials Chemistry C* 2022, 10 (4), 1403-1413.
- 20. Chander, A.; Chiuyen, P.; Murali, B.; Santosh, R.; Guping, T. Polymer Properties: Functionalization and Surface Modified Nanoparticles. In Role of Novel Drug Delivery Vehicles in Nanobiomedicine, Rajeev, K. T., Neeraj, G., Rahul, S., Prakash Singh, B. Eds.; IntechOpen, 2019; p Ch. 7.
- 21. Purushothamreddy, N.; Santhosh, R.; Ketavath, R.; Murali, B.; Joseph, D. P. Optimization of nanocrystalline Sb doped BaSnO3 for dye-sensitized solar cell applications. AIP Conference Proceedings 2020, 2265 (1), 030650.
- 22. Amgoth, C.; Santhosh, R.; Malavath, T.; Singh, A.; Murali, B.; Tang, G. Solvent-Assisted [(Glycine)-(MP-SiO₂NPs)] Aggregate for Drug Loading and Cancer Therapy. *Chemistry Select* 2020, 5 (27), 8221-8232.



23. Amgoth, C.; Singh, A.; Santhosh, R.; Yumnam, S.; Mangla, P.; Karthik, R.; Guping, T.; Banavoth, M. Solvent assisted size effect on AuNPs and significant inhibition on K562 cells. *RSC Advances* 2019, 9 (58), 33931-33940.

- 24. Rompivalasa Santhosh, Savu Ramu Naidu, Banavoth Murali, Unlocking Solar Cell Potential: EDTA as a Self-Assembling Chelating Molecule for Enhanced Electron Transport in Perovskite Solar Cells, (Manuscript under Communication).
- 25. Rompivalasa Santhosh, Savu Ramu Naidu, Ranadeep raj S, Banavoth Murali, Leveraging Guanidinium Thiocyanate Self-Assembly to Enhance Perovskite Solar Cell Efficiency (Manuscript under Communication).
- 26. Rompivalasa Santhosh, Savu Ramu Naidu, Ranadeep raj S, Banavoth Murali, Exploring the Effects of Temperature Annealing on Electron Transport Layers to Ease the Perovskite Solar Cell Fabrication (Manuscript under Communication).

Scientific Presentations

Oral Presentations:

Carbazole substituted Triphenylamine based Organic small molecules as
efficient HTMs for PSCs - School of Chemistry, 20th Annual In-House
Symposium held at University of Hyderabad, Telangana, India (CHEMFEST2023).

Poster Presentations:

- Organic Small Molecules as Efficient Hole Transporting Materials for Perovskite Solar Cells- International Conference 33rd AGM of MRSI and 4th Indian Materials Conclave, Conducted by International Union of Materials Research Society-International Conference in Asia – 2022 (IUMRS-ICA 2022) and IIT Jodhpur, India – Dec 19-23, 2022. Got Best poster presentation award.
- Carbazole substituted Triphenylamine based Organic small molecules as
 efficient HTMs for PSCs School of Chemistry, 20th Annual In-House
 Symposium held at University of Hyderabad, Telangana, India (CHEMFEST2023).
- Single crystalline Perovskite Thin Films: Application in Solar Cell School of Chemistry, 19th Annual In-House Symposium held at University of Hyderabad, Telangana, India (CHEMFEST-2022).



Participated in Workshops:

- National Workshop on Advanced Material Characterization Techniques
 (NWAMCT-2018), held on 31st August 2018, Conducted by Department of
 Physics-2018, Osmania University (OU)-Hyderabad, Telangana.
- Energy Materials and Innovative Challenges and its Applications, held on 6th-10th October 2018, Conducted by JNTU-(GAIN-2018)-Hyderabad, Telangana.
- Science Communication 101 Workshop, held on 28th August, 2019, Conducted by TIFR, Hyderabad, Telangana.
- Workshop on Perovskite Solar Cells held on 15th 16th October, 2019, Conducted by the IIT-Bombay and Continuing Education& Quality Improvement Programs (CE&QIP).
- **Short Course on Spectroscopic Ellipsometry**, held on 4th- 5th November, 2019, Conducted by JNCASR, Bangalore, Karnataka.



University of Hyderabad

"Harmonizing Energy: Unveiling Enhancement Strategies for High-Efficiency Perovskite Solar Cells"

by Santhosh Rompivalasa

Indira Gandhi Memorial Library
UNIVERSITY OF HYDERABAD
Central University P. O.

HYDERABAD-500 046.

Submission date: 01-Aug-2024 02:34PM (UTC+0530)

Submission ID: 2425730146

File name: Thesis_antiplagarism_rompivalasa_santhosh.docx (444.73K)

Word count: 23793

Character count: 140029

"Harmonizing Energy: Unveiling Enhancement Strategies for High-Efficiency Perovskite Solar Cells"

ORIGINALITY REPORT PUBLICATIONS SIMILARITY INDEX **INTERNET SOURCES** STUDENT PAPERS **PRIMARY SOURCES** publishup.uni-potsdam.de 2% Internet Source vtechworks.lib.vt.edu Internet Source Submitted to University of Hyderabad, Hyderabad Student Paper Hao Huang, Ziyu Li, Zhijia Chen, Denggao Li, % 4 Hongxi Shi, Keqi Zhu, Chenyu Wang, Zhangbo Lu, Shihua Huang, Dan Chi. "Interfacial modification engineering for efficient and stable MA-free wide-bandgap perovskite solar cells by grain regrowth", Materials Chemistry Frontiers, 2024 **Publication**

T.M. Mukametkali, B.R. Ilyassov, A.K. Aimukhanov, T.M. Serikov, A.S. Baltabekov, L.S. Aldasheva, A.K. Zeinidenov. "Effect of the TiO2 electron transport layer thickness on

<1%

charge transfer processes in perovskite solar cells", Physica B: Condensed Matter, 2023

Publication

6	George G. Njema, Joshua K. Kibet, Silas M. Ngari. "A review of interface engineering characteristics for high performance perovskite solar cells", Measurement: Energy, 2024 Publication	<1%
7	www.mdpi.com Internet Source	<1%
8	www.epjap.org Internet Source	<1%
9	www.nature.com Internet Source	<1%
10	Dong Yang, Ruixia Yang, Kai Wang, Congcong Wu et al. "High efficiency planar-type perovskite solar cells with negligible hysteresis using EDTA-complexed SnO2", Nature Communications, 2018	<1%
11	"Perovskite Optoelectronic Devices", Springer Science and Business Media LLC, 2024 Publication	<1%
12	Ajay Kumar Jena, Ashish Kulkarni, Tsutomu Miyasaka. "Halide Perovskite Photovoltaics:	<1%

Background, Status, and Future Prospects", Chemical Reviews, 2019

Publication

13	Jiangzhao Chen, Nam-Gyu Park. "Materials and Methods for Interface Engineering toward Stable and Efficient Perovskite Solar Cells", ACS Energy Letters, 2020 Publication	<1%
14	pubs.rsc.org Internet Source	<1%
15	www.researchgate.net Internet Source	<1%
16	Herzog, Martin. "RINGOSTAR - An Evolutionary Performance Upgrade of Optical Ring Networks", Technische Universität Berlin, 2006. Publication	<1%
17	Yanbo Gao, Yanjie Wu, Hongbin Lu, Cong Chen, Yue Liu, Xue Bai, Lili Yang, William W. Yu, Qilin Dai, Yu Zhang. "CsPbBr3 perovskite nanoparticles as additive for environmentally stable perovskite solar cells with 20.46% efficiency", Nano Energy, 2019	<1%
		_

Xuerui Pang, Jing Huang, Chunxia Lin, Yingfang Zhang, Nian Cheng, Wei Zi, Zhu-Zhu Sun, Zhen Yu, Zhiqiang Zhao. "Buried

<1%

Interface Regulation by Bio-Functional Molecules for Efficient and Stable Planar Perovskite Solar Cells", Chemistry – A European Journal, 2022

Publication

patents.google.com <1% 19 Internet Source Mahesh Kumar, Sheher Yar Khan, Shuli Liu, 20 Wenjie Ji et al. "Scientific mapping and data analysis of the research landscape in perovskite solar cell technology", Solar Energy, 2024 **Publication** Meiying Zhang, Fengmin Wu, Dan Chi, Keli <1% 21 Shi, Shihua Huang. "High-efficiency perovskite solar cells with poly(vinylpyrrolidone)-doped SnO as an electron transport layer ", Materials Advances, 2020 Publication Submitted to University of Surrey <1% 22 Student Paper Chen, Qi, Nicholas De Marco, Yang (Michael) 23 Yang, Tze-Bin Song, Chun-Chao Chen, Hongxiang Zhao, Ziruo Hong, Huanping Zhou, and Yang Yang. "Under the spotlight: The organic-inorganic hybrid halide perovskite for optoelectronic applications",

www.science.gov
Internet Source

29

24	Zhelu Hu, José Miguel García-Martín, Yajuan Li, Laurent Billot et al. "TiO Nanocolumn Arrays for More Efficient and Stable Perovskite Solar Cells ", ACS Applied Materials & Interfaces, 2020 Publication	<1%
25	solarstarinfo.com Internet Source	<1%
26	Luis K. Ono, Emilio J. Juarez-Perez, Yabing Qi. "Progress on Perovskite Materials and Solar Cells with Mixed Cations and Halide Anions", ACS Applied Materials & Interfaces, 2017 Publication	<1%
27	Samira Vafaei, Mohammad Hossein Hekmatshoar, Farhang Abbasi. "Poly(3-dodecylthiophene)-grafted multi-walled carbon nanotubes: an additive for improving charge transport properties of triple cation perovskite solar cells", Journal of Materials Science: Materials in Electronics, 2023 Publication	<1%
28	fastercapital.com Internet Source	<1%

3	theses.lib.polyu.edu.hk Internet Source	<1%
3	openprairie.sdstate.edu Internet Source	<1%
3	2 worldwidescience.org Internet Source	<1%
3	Leiping Duan, Ashraf Uddin. "Defects and Stability of Perovskite Solar Cell: A Critical Analysis", Materials Chemistry Frontiers, 2022	<1%
3	Marc J. Madou, S. Roy Morrison. "Solid-State Background", Elsevier BV, 1989 Publication	<1%
3	Oleksandr Masalskyi. "Investigation and application of hot carrier phenomenon in photovoltaics", Vilnius Gediminas Technical University, 2023 Publication	<1%
3	Submitted to Pusan National University Library Student Paper	<1%
	Seckin Akin. "Hysteresis-Free Planar Perovskite Solar Cells with a Breakthrough Efficiency of 22% and Superior Operational Stability over 2000 h", ACS Applied Materials & Interfaces, 2019 Publication	<1%

39

40

Ya-Nan Zhang, Qun Li, Bo Li, Cheng-Xiang Wang. "Insight into structure defects in highperformance perovskite solar cells", Journal of Power Sources, 2023

<1%

Publication

- - Haimang Yi, Dian Wang, Md Arafat Mahmud, Faiazul Haque, Mushfika Baishakhi Upama, Cheng Xu, Leiping Duan, Ashraf Uddin. " Bilayer SnO as Electron Transport Layer for Highly Efficient Perovskite Solar Cells ", ACS Applied Energy Materials, 2018

<1%

Publication

41

Organic-Inorganic Halide Perovskite Photovoltaics, 2016.

<1%

Publication